One-Dimensional Strain Initiated by Rapid Compaction of a Heterogenous Granular Mixture Consisting of Cu, Fe, SiO2, C, MoS2, and Sn

Cullen Braun
Marquette University

ONE-DIMENSIONAL STRAIN INITIATED BY RAPID COMPACTION OF A HETEROGENOUS GRANULAR MIXTURE CONSISTING OF Cu, Fe, SiO_2, C, MoS_2, AND Sn

by

Cullen A. Braun, B.S.

A Thesis Submitted to the Faculty of the Graduate School,
Marquette University,
in Partial Fulfillment of the Requirements for
the Degree of Master of Science

Milwaukee, Wisconsin

May 2011

ABSTRACT

ONE-DIMENSIONAL STRAIN INITIATED BY RAPID COMPACTION OF A HETEROGENOUS GRANULAR MIXTURE CONSISTING OF Cu, Fe, SiO_2, C, MoS_2, AND Sn

Cullen A. Braun, B.S.

Marquette University, 2011

The dynamic compaction of metal powders is of great interest to the metallurgical and military communities. The compaction of a heterogeneous granular mixture consisting of copper, iron, silica, graphite, molybdenum-disulfide, and tin predominately used in aviation break-pad creation is presented. The initial density of the material was on average $2.756\frac{g}{cm^3}$. The research also required developing a working projectile velocity measurement system and a proper target assembly for pressure measurements. Manganin gages were used to record the shock wave transit time and the pressure of the transmitted waveform into the powder mixture. An impedance matching technique was utilized to determine the particle velocity at the powder-impact plate interface and the shock velocity was determined from the measured data. The shock velocity and particle velocity were plotted to develop a linear equation of state, $U_s = SU_p + C_0$. The linear equation of state was determined to have a Hugoniot slope of $S = 0.3949 \pm 1.2869$ and a bulk sound speed of $C_0 = 0.552 \pm .188(m/s)$. The equation of state was then employed in bulk one-dimensional computer simulations to compare to the waveform obtained from the pressure measurement system. The post-impact samples were investigated using a scanning electron microscope and electron dispersive spectroscopy to compare the microstructure of the dynamically compacted samples to the commercially manufactured pressed and sintered sample. The bulk scale simulations proved to recreate the pressure waveform from the pressure measurement system. It was also found that the dynamically compressed samples had minimal evidence of sintered grains, but had significant lateral fractures resulting from release.

ACKNOWLEDGEMENTS

Cullen A. Braun, B.S.

I would like to give thanks to God the Father and Our Lord and Savior Jesus Christ for giving me the strength and ability to persevere and accomplish all endeavors.

My family for the love and support they have given me as I continued my education and worked toward my goals.

Marquette University (Department of Mechanical Engineering) for the opportunity and financial support to pursue higher education and the resources to accomplish the research objectives.

Dr. John Borg, my advisor, for the opportunity to research an awesome topic. I never thought I would be able to apply one of favorite recreational hobbies (hunting/shooting) to research in various areas. Also, thanks for the direction and always having an open door to discuss the problems and successes of the research. Thanks for the opportunity to attend conferences and open my eyes to the numerous applications and problems others in the shock physics community aim to solve.

Dr. Jon Koch and Dr. Rice for being on my committee and their advice in completing the thesis. Also, Dr. Rice for taking the time to discuss the techniques for characterizing the powder and the equipment required to complete the tasks.

Ray Hamilton, Dave Gibas, and Tom Silman for their assistance and advice over the countless hours I spent in the DLC. Without their guidance and input the project would not have been as successful. I was also taught skills in the machine shop that I will be able to utilize for many years to come.

Dr. Fournelle and Tao Yan for their assistance in performing the static compaction and microscopy procedures.

To Drew Fraser and Ken Jordan for their help in conducting the experiments and their input in addressing problems that existed in the research.

Annette Wolak for organization in helping to complete the steps necessary for graduation and the help in purchasing components necessary for the research.

To my friends for their support and ability to turn my mind 180 degrees from the research when I needed a break.

To the many others who helped both directly and indirectly to the completion of this work, without the assistance of many this work would not have been possible.

TABLE OF CONTENTS

TABLE OF CONTENTS — *Continued*

LIST OF FIGURES

LIST OF FIGURES — *Continued*

LIST OF FIGURES — *Continued*

LIST OF FIGURES — *Continued*

LIST OF TABLES

CHAPTER 1

Introduction

1.1 Motivation

The work contained in this thesis consists of the measurement systems of a single-stage gas gun and the compaction of heterogeneous granular materials both of interest to the shock physics and manufacturing groups in Marquette University's Department of Mechanical Engineering. The research aims to improve the velocity measurement system presented by Thomas J. Downs (M.S. 2006) upon building the gas gun and the work completed by Jeffrey Midday (Summer 2009). A system for acquiring stress traces through a target consisting of granular materials will be developed. The target must include circuitry for a time-of arrival detector and two manganin stress gages, in addition to holding vacuum on the barrel end. The gas-gun configuration with the updated measurement systems will allow the acquisition of several parameters essential for shock physics experiments, including projectile velocity, time-of-arrival at projectile-target interface, peak stress, transit time through the target, and stress through the powder.

The heterogeneous granular mixture of interest in this study is a formulation present in aviation break-pads for use as a friction material. This formulation is composed of 42% copper, 19% iron, 18% graphite, 17% silicon-dioxide, 3% molybdenum-disulfide, and 1% tin. The resulting microstructure from dynamic loading is of great interest, especially in regards to possible sintering of the granular constituents. The dynamic compaction of the proposed granular mixture in conjunction with the developed measurement systems will provide the basis of the research. Flyer-plate experiments will be conducted on the granular mixture to develop the shock velocity-particle velocity, $(U_s - U_p)$, empirical equation of state, which describes the shock response of materials in the absence of phase transitions [6]. In addition, from the $(U_s - U_p)$ equation of state, the Pressure-Density, $(P - \rho)$, shock relationship will be developed and compared to the

solid Hugoniot relationship utilizing a mixture theory, and the experimental data. Another objective will be to perform scanning-electron-microscopy (SEM) and optical microscopy on the compacted samples for comparison to statically pressed and sintered mixtures as is commonly conducted in industry. Special consideration will be given to the welding of individual grains and the effect that initial projectile velocity and pressure have on the post-impact microstructure.

1.2 Background

In the 1970's research pertaining to the rapid-solidification of metal powders and the shock waves produced became a topic of great interest to the metallurgical and shock physics communities [7]. The interest stems from the ability to create localized temperatures and pressures of microsecond duration required for metallurgical bonding of individual particles while allowing the initial microstructure of the bulk powder to remain intact [8] [7]. The introduction of favorable physical, chemical and physiochemical changes to the initial powder may eliminate the lengthy sintering and static loading processes of industrial powder metallurgy applications [8]. Many parameters have been considered in the research of developing a reproducible procedure for compacting powders, including: initial flyer plate/explosive velocity, the initial specific volume of the powder to be compacted, the particle grain size, the initial temperature, the duration of the shock pressure, and the adiabatic compressive energy and thermal energy [of the compacted powder at pressure] [2]. In addition, the previously mentioned parameters have been extensively evaluated in the creation of experimental and numerical models along with the development of more precise equations of state. The development of models and equations of state are of the utmost importance to the shock physics community, as they reduce the need to perform countless gas-gun experiments. The following review will outline the pillars of new and old regarding the experimental procedure with a focus on the use of manganin gauges for acquiring stress signals, numerical models and equations of state, the use of hydrocodes and computer simulation to model the behavior of compacted powders, and experimental and numerical results. The primary focus of the research to be conducted is on the shock compaction of a copper, iron, graphite, sand, tin, and

molybdenum-disulfide powder mixture; the journal articles discussed in this review focus on compaction of the components above in particular copper, which constitutes 42% of the heterogeneous mixture. In additional, it is important to note that a majority of the articles in this area of shock physics research is devoted to the study of porous foams, which for the most part are created by statically loading and sintering the metal powders prior to the dynamic impact. However, an argument will be made that the equations of state and governing equations of the porous foam can be applied to the rapid compaction of granular-powder mixtures.

1.3 Observed Experimental Apparatuses

The experimental apparatus for performing dynamic loading experiments must display repeatable behavior, be easily controllable, and safe. Light-gas gun experiments have been the standard in performing rapid-compaction experiments due to the gun's ability to adhere to the standards mentioned above. Another experimental method applied consists of a high-explosive assembly, but with increased safety concerns in operation and explosive material storage, the light gas model becomes a more suitable and comparable alternative. The light-gas guns are typically built in a one-stage or two-stage configurations which allow for maximum projectile velocities of 1-2 km/s and up to 8 km/s respectively [7]. All projectile velocities presented in the reviewed research ranged from 69 m/s to 1000 m/s. The light gas gun assembly will also contain fixtures for a velocity measurement system and a target-gauge system to measure the projectile velocity impact and propagated stresses, respectively. A generic system schematic of the assembly can be seen in Figure 1.1 below less the velocity measurement system [7].

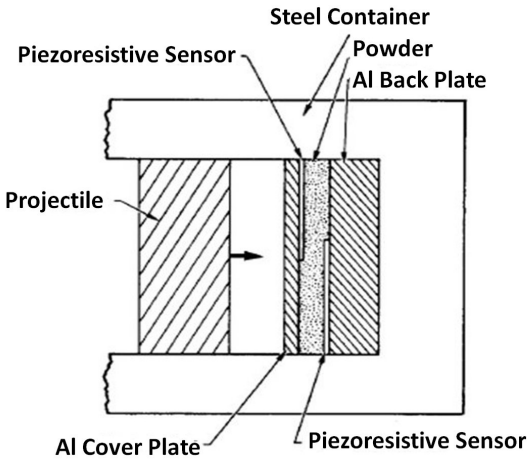

Figure 1.1: Schematic of Gas Gun Impact-Target Assembly.
Note the back plate, cover plate, and container materials do not need to be those specified in the figure.

Meyers describes that every shock propagation event must measure the following specific variables: [6].

1. Wave or particle arrival time: In these detectors, the arrival of a signal (wave or moving object) triggers an external measurement source
2. Discrete particle displacement versus time
3. Continuous particle displacement over time
4. Stress versus time: Piezoelectric and Piezoresistive Gage Assemblies

The techniques listed above are able to capture all the data pertinent to an impact test, and aid in the construction of equation of states and the baseline to determine accuracy of numerical models. It is important to note that the gun barrel should be evacuated when implementing these techniques [9] [10] [11]. The evacuated barrel will accomplish three pivotal tasks: the vacuum seal will pull all the components together, prevent ionizing and conducting of the air which could lead to circuit shorting , and the compressed gas in the barrel, as the projectile travels, could destroy any non-rigid components (i.e. velocity system) [6]. The following paragraphs will discuss the implementation of these techniques, except for the continuous particle displacement over time. The laser interferometer and VISAR devices used to capture the continuous particle displacement over time data

will not be utilized in the author's research and therefore not discussed. The particle velocity (displacement over time) will be numerically calculated using an impedance matching technique, which will be discussed shortly. The other three mechanisms mentioned by Meyer's are sufficient for acquiring the data necessary to conduct the author's research.

The wave or particle arrival time is essential for the successful triggering of the stress measurement systems. The most common triggering mechanism in the analyzed research is a pin mechanism (circuit) placed at the projectile-target interface [9] [10] [11]. Depending on the conductivity of the flyer plate either a break introducing an open circuit or a short circuit trigger could be created. In the case of Boade and Lynse using a short circuit, the scope was triggered 0.4 microseconds and 0.5 microseconds prior to impact [9] [10]. This short time duration will also maximize the amount of available memory in the measurement source or oscilloscope. As will be discussed in the stress measurement section, this will also prevent premature heating of the gauges due to the time duration of applied current and voltage.

The discrete particle displacement versus time is used to determine the projectile velocity. The general technique is to locate a series of pins a known distance apart on the gas-gun barrel and measure the time required to pass each pin. A circuit is developed so the passing projectile induces a voltage when contact is made with the pin and displays the voltage on an oscilloscope. Similar to the wave/particle arrival time a short circuit, break circuit, make circuit, or inverting circuit could be incorporated to determine the particle displacement. A sample oscilloscope trace for any inverting circuit can be seen in Figure 1.2 below. Boade utilized three charged shorting pins located 19 mm from the target assembly and a known distance part [9]. Vandersall also used three shorting pins placed 12.7 mm apart and 6.35 mm from the target surface [8].

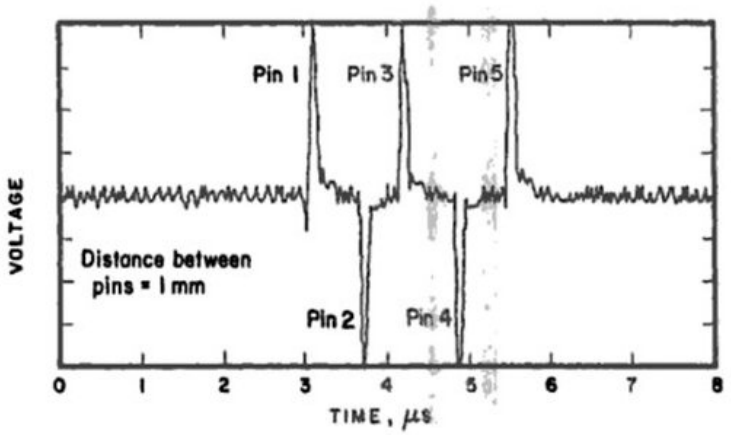

Figure 1.2: Oscilloscope Trace of Inverting Circuit for Determining Particle Displacement vs. Time.
The Distance between pins is known and from the max or half-voltage of the Pin Peaks the time between Pins can be determined [6]

Much of the early stress measurement devices for porous materials utilized the X-quart gauges. The quartz gauges provided accurate stress measurements for stresses less than 2.5GPa [7]. However, a more versatile stress gauge referred to as a manganin gauge consisting of a 84 wt% Cu, 12 wt% Mn, and 4 wt% Ni alloy was available, although not the standard for early impact testing [6]. The manganin gauges can successfully measure stresses up to 30 GPa [6]. Both gauge assembly's are constructed using the same principles and mechanisms with the goal of obtaining a record of stress as a function of time, but with contrasting working materials . The construction of the target utilizes a "sandwich" technique with the gauge placed between two insulating materials with an epoxy adhesive (see Figure 1.3).

The type of insulating material varied greatly in the discussed research with no real explanation for their given choice in comparison to another non-conducting material. Also, many of the early experiments did not utilize an insulating material and simply potted the gauge with C-7 epoxy of thickness less than 0.001cm [12] [3] . Vandersall choose a 25 micrometer FEP Teflon Insulator potted with 2-4 micrometer epoxy [8]. Lynse, Borg, and Rosenberg used PMMA plates of varying thickness ; Rosenberg also attached a 19 micrometer Mylar sheet when using copper back plates [13] [5] [1]. Linde argued that a buffer shim must be placed over the gauge to prevent erroneous measurements, but with little explanation given. Aluminum, C-7

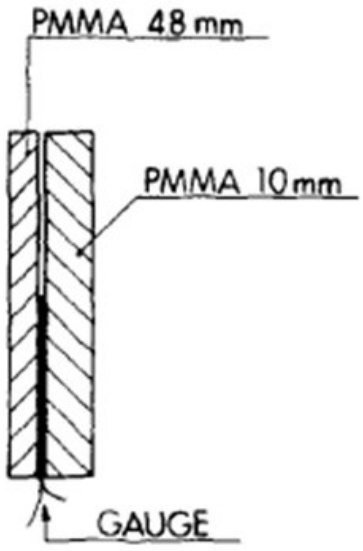

Figure 1.3: "Sandwich" Target using PMMA Insulators [1]

epoxy, and Mylar sheets were analyzed by Linde [11]. Linde concluded that a 0.025 mm Mylar shim was of sufficient thickness to be used as an insulator. Linde also noted that the use of mylar shim will reduce the recorded pressure by more than 10% when compared to gauges with no shim present. In addition, 0.3 mm C-7 epoxy coating was the minimum thickness to eliminate the contact between the porous surface and the gauge [11]. The following 0.08, 0.25, 0.48, 0.75, and 3.2mm thick aluminum shims were also tried on the gauge assemblies and Linde concluded that the 0.25 mm shim was sufficient to provide reliable stress readings [12]. In addition, to prevent localized stretching of the manganin gauge, a buffering shim must be present otherwise the change in resistance associated with a particular strain would alter the gauge response to pressure [12]. Rosenberg emphasizes the need of an insulating sheet of Mylar when using metallic surfaces for the front and back plate of the gauge [1]. A 70/30 mixture of resin to hardener for the epoxy mixture was also proposed by Rosenberg [1] . The requirement of an embedded gauge and a protective insulating material was also suggested by Meyers, who included that the manganin gauges must also be properly calibrated using a balancing technique [6].

The material behavior of the quartz gauges is described as piezoelectric while in contrast the manganin gauges are piezeoresistive. This implies that when stressed the quartz gauges generate an electrical charge (i.e change in current). Manganin

gauges on the other hand will exhibit a change in electrical resistivity with pressure. The advantage of the piezoelectric gauges over the piezeoresistive gauges is the piezoelectric gauges do not require an external power supply; however both will require an oscilloscope. The piezoresistive gages will require a pulsed power supply to provide the current required during the test. The voltage change due to the change in gauge resistance is then captured by the oscilloscope. Most manganin gauges have a resistance of approximately 50 ohms. Meyers suggests the importance of triggering the pulse-power supply milliseconds prior to the shock wave arrival to prevent the gauge from prematurely burning due to" resistive heating." [6] The piezoelectric gauges will not be discussed in more detail due their absence in the authors conducted research.

An additional component that did not receive discussion from Meyers was the projectile construction. The research reviewed all assumed a planar impact so by nature it was assumed that all the projectiles had a flat face. Linde mentions that the projectile flyer plates were machined flat and square to the impact axis to within 0.002 mm [11]. An additional assumption confirmed by Linde was all projectiles were full density (non-porous) [11]. Linde also mentions that the flyer plate should have the same composition as the driver or target plate to make numerical calculations simpler (The importance of this aspect will be discussed in the equation of state section) [11] . All of the projectiles discussed contained a metal flyer plate of aluminum, brass, or copper. However, the sabot or flyer plate housing consisted of Styrofoam, polyethylene foam, or aluminum. Also Lynse, Boade, and Vandersall had schematic drawings that incorporated an o-ring into the projectile assembly to seal downstream gas from escaping into the evacuated barrel. Also, when quartz gauges were used the projectiles contained an epoxy potting on their interior to affix the gauge to the projectile. Vandersall notes that the impact experiment should be "designed such that the planar-parallel shock wave propagates through the powder thickness without attenuation from loading or peripheral surfaces." So, the flyer plate should be of adequate length to prevent numerous wave transmissions and reflections in the target material.

The final pivotal aspect of the experimental apparatus is the preparation of the porous or granular samples. Vandersall created the Mo + 2 Si sample powders

using a slow moving V-blender for duration of 8-12 hours [8]. Linde and Boade both sintered their copper powders into a porous foam. The foam described by Linde consisted of 5 or 10 micron powders sintered at 1700 F for copper and 1600F for iron followed by being surface grounded, cleaned in an ultrasonic cleaner, and baked in a vacuum oven for 16 hours [11]. In the majority of the experiments the researcher used spectroscopy to analyze the initial microstructure of the porous foam. The graphite used by Linde required no specific fabrication upon receipt from commercial supplier [11]. Boade also created samples by placing 10-100 micron copper powders into a rubber sack before being submerged in a hydrostatic press to 1.4 kbar. All the porous foams discussed were made in quantities large enough that a lathe equipped with a vacuum chuck was used to partition the samples. As Lynse discusses, the turning process removes individual powder grains rather than cutting through the grains so the surface contains the same regularities as the sample as a whole [13]. It is also important to note that all the porous foams were put on a fine abrasive cloth to get planarity less than 0.005 mm. There was also no direct mention of the reason for the particular sample thicknesses. The range seemed to include 0.5-2.00mm and there was no correlation between projectile velocity and sample size, as initially suspected [9].

From the above discussion on rapid compaction of powder and porous foams the following conclusions can be drawn. A light-gas gun allows a compaction mechanism with the most control and highest safety factor. The projectiles should contain an o-ring to prevent gas from escaping downstream from the gas source. In addition the projectile should contain a light weight sabot/housing and a full density flyer plate of common material with the impact/driver plate. The flyer plate should also be of ample thickness to prevent any stress attenuation from arriving at the gauges in a comparable time frame to the initial stress wave. A series of flyer plate finishing steps should be used to insure that the flyer plate is flat and square for a planar impact. Also, a projectile or wave arrival circuit should be employed at the impact interface to trigger the oscilloscope 0.5 microseconds before impact. Also, a velocity pin measurement system containing three or more pins should be located several inches upstream from the impact interface. The velocity pin system should be displayed on the oscilloscope with an appropriate circuitry of low voltage

(2V or less). A "sandwich" gauge system should be utilized to guarantee accurate stress readings. The "sandwich" should contain an aluminum (appropriate metal) shim (0.25mm), a Mylar or Teflon sheet (<0.25 micrometers), or 0.3 mm of epoxy as an encapsulating material. Since powder samples are being considered, one would advise not to use only an epoxy shim due to possible distortion of the stress results from powder-gauge interaction. The "sandwich" should be potted with C-7 epoxy to protect the gauge and keep the gauge fixed between the two insulating sheets. Caution should be taken that a conductive material is not placed in contact with the gauge.

1.4 Equations of State

Developing an accurate and simplistic model for equation of states of porous materials is essential to effectively applying the discovered phenomena. As discussed in the introduction, numerous parameters must be considered when constructing an equation of state including both physical and thermal properties. However, an equation of state should not be so robust and inclusive that the underlying physics of the problem is lost and any analytical calculation becomes too tedious. In addition, a too simplistic model will not capture the essential physical behavior experimentally observed [14]. The best method for determining an appropriate equation of state still remains trial and error [14].

This section will discuss several methods for determining an equation of state for shock waves through a porous material and computational methods used to represent the compaction process. The Rankine-Hugoniot equations, in mass, momentum, and energy, will be presented in addition to the equation of state required to solve the system of equations. Methods will also be presented, such as those by Hermann, Carroll and Holt, and Boade that describe the compaction process of a porous material as two distinct processes: collapse of pores, and compression of compacted material [15] [16] [3]. Dijiken, also considered a two part equation of state based on the possiblity that the post-compacted sample could have a specific volume greater than the initial pre-compacted sample and the intutive behavior that the post-compacted sample has a lower specific volume than the pre-compacted sample [2]. Meyers relayed an equation of state for the Hugoniots of

powders based on the Mie-Grüneisen equation with parameters of both the solid and porous materials considered [6].

1.4.1 Rankine-Hugoniot Equations

Ferreira and Meyers included a schematic illustrating the multiple stage process of shock consolidation [17]. The process begins with an initial porous material impacted with a shock wave leading to void collapse and densification of the material, followed by the melting of the particle boundaries, the deformation and phase transformation of the particles, and lastly the kinetic energy imparting a residual velocity of the compact. The research articles reviewed were mixed between those focusing on a single aspect of the shock consolidation process and those striving to develop a working model for the process as a whole. Regardless, the ultimate goal of an equation of state in porous materials is to develop and accurate model that specifically describes the Hugoniot relationships of the compact. The Hugoniot is a locus of the potential end states a material can possess undergoing shock loading. The Hugoniot of a material must ultimately be determined experimentally, most commonly by finding the shock speed and particle velocity relationship, but the equation of state will reduce the need for experimentally determining the material behavior for each potential porosity. The Rankine-Hugoniot relationships describe the conditions necessary to "jump" or eliminate the discontinuity that exists from the compression induced shock wave in the material. Below are the mass, momentum, and energy conservation equations for the Rankine-Hugoniot which apply to any steady shock-wave, comparing specific volume V, the pressure P, the particle speed U_p, the shock speed U_s, and the internal energy E. Also below is the linear-empirical relationship between the shock speed and the particle speed, where S is the Hugoniot Slope and C_0 is the bulk sound speed in the material at zero pressure [6].

$$\rho_0 U_s = \rho(U_s - U_p) \quad \text{Mass} \quad (1.1)$$

$$P - P_0 = \rho_0 U_s U_p \quad \text{Momentum} \quad (1.2)$$

$$PU_p = \frac{1}{2}\rho_0 U_s {U_p}^2 + \rho_0 U_s (E - E_0) \quad \text{Energy} \quad (1.3)$$

$$U_s = U_p S + C_0 \quad \text{Equation of State} \quad (1.4)$$

From the equations above it becomes clear that with the equation of state only two of the variables must be known to completely describe the state of the system. The equation of state is experimentally determined using flyer-plate experiments for conditions that will not produce phase transitions. Also, the linear relationship suggests that as the fyler plate velocity increases, the velocity of the resultant shock wave also increases. The articles reviewed work to develop the relationships for the above variables describing an impact experiment with a porous sample. The critical concern that must be addressed lies with the pressure required to compact the initial porous material to a completely compacted solid. For many researchers a "snowplow" method was formulated that suggested the compaction occurred at zero stress [15]. The problem with this method is the powder Hugoniot curves in $P - V$ space indicate that more energy is absorbed in the compaction of a porous material then a solid material due to the reduction in initial volume from the voids in the material collapsing under loading. This is why porous and granular materials are great shock absorbers. However, it is visibly apparent in Figure 1.4 that as the porous material is compacted the Hugoniot of the porous material approaches that of the solid material.

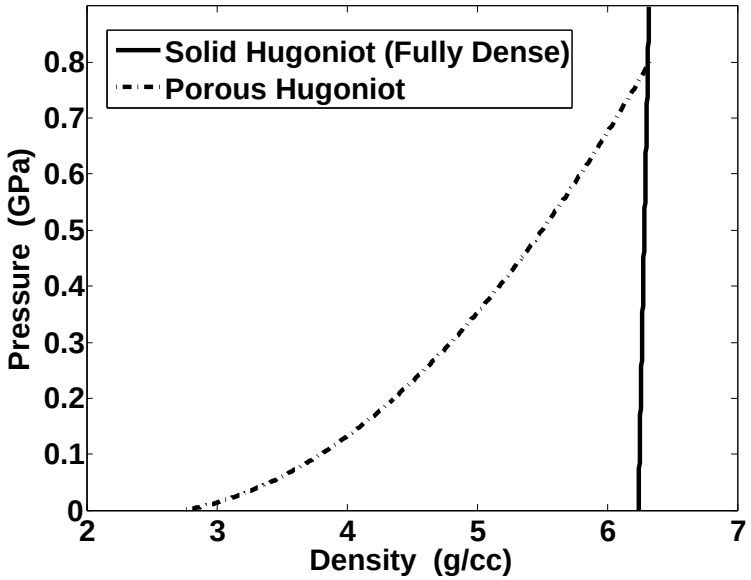

Figure 1.4: Pressure-Density Plot of Hugoniots for a Solid and Porous Material

In addition, the Rankine-Hugoniot equations above provide the basis for implementing the impedance matching technique. The impedance matching technique allows one to calculate the pressure between two interfaces. In order to calculate the pressure, the Hugoniot relationships must be rearranged into the Pressure-Particle Velocity relationship depicted below.

$$P = \rho_0(C_0 U_p + S U_p^2) \tag{1.5}$$

The equation above only depicts the stationary aspect or target of the experiment. The other component, the flyer or projectile, can be described in $P - U_p$ space below, where V is the velocity of the projectile.

$$P = \rho_0(-C_0(U_p - V) + S(U_p - V)^2) \tag{1.6}$$

From the two equations below, it is clear that with the knowledge of the $U_s - U_p$ equation of state, the density of the material, and the projectile velocity, the pressure between any two interfaces can be determined. An example of an interaction between a Copper and an Aluminum projectile is depicted in Figure 1.5 below.

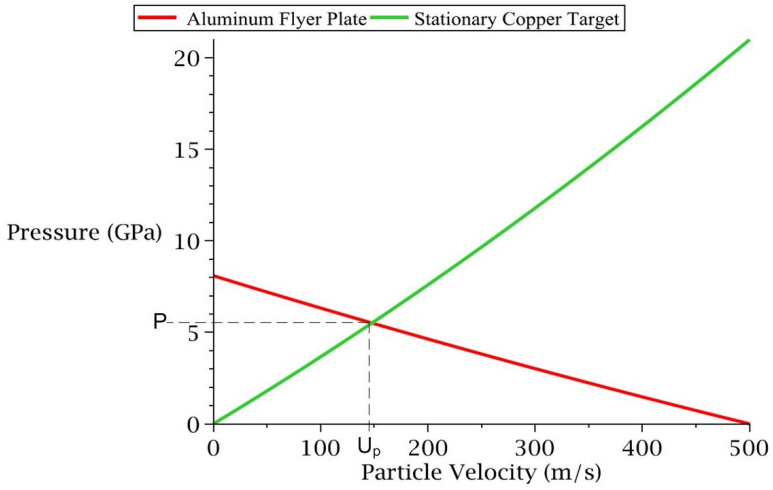

Figure 1.5: Impedance Match for 500 m/s Aluminum Flyer Plate Impacting Copper

Further, by reflecting the curves one can determine the pressure at interfaces of a target consisting of numerous materials with only the parameters discussed in the previous paragraph. This technique provides a simple calculation to determine the pressure of an impact experiment.

1.4.2 Equation of State Presented by Meyers

Meyers discusses an equation of state based on the Hugoniot relationships and the Mie-Grüneisen equation that relates both the solid and powder states. The conservation of mass, momentum, and energy are applied to both the powder and the solid including the standard pressure-volume relationship for solid materials. The resulting equations are substituted into the Hugoniot based on the Mie-Grüneisen equation (Equation 2.6) yielding the Pressure and Volume relationship for the powder in Equation 1.8 below [6]:

$$P = P_H + \frac{\gamma}{V}(E - E_H) \tag{1.7}$$

$$P = \frac{[2V - \gamma(V_0 - V)]C^2(V_0 - V)}{[2V - \gamma(V_{00} - V)][V_0 - S(V_0 - V)]^2} \tag{1.8}$$

From the above equation, the Rankine-Hugoniot relationships can be employed to determine the values of the other parameters U_p, E, and U_s. Gourdin argues that this equation is simply a relationship between the pressure of an individual powder particle, the specific volume compression of that particle, and the

specific volume of the porous volume as a whole, when the required relationship is between the average pressure in the porous body as a function of the specific volume of the distended body [7].

1.4.3 Dijken Equation of State

Dijken develops an equation of state similar to that Meyers discussed above with two initial porosity conditions based on the anomalous behavior that the final specific volume may be greater than the initial specific volume. One would assume that when a powder is compacted it would reach a state of greater density but experimentally that has not always been the case [18]. Dijken makes the following assumptions in his model [2]:

1. The compaction of a powder at zero pressure quasi-statically from V_{00} to the solid specific volume does not require any energy

2. The material is completely compacted behind the shock wave (no voids present)

3. The increase in internal energy is equally distributed inside the compacted material (Pressure and temperature fields are uniform)

4. There are no volume or energy changes due to deformation of phase transformations.

The first case Dijken considered was when the final specific volume was less than the initial specific volume. The final states of this scenario are calculated from compacting the solid material from a volume V_0 to V_2 along the Rayleigh Line and then heating the material at constant volume to pressure P_1. Equation 1.8 above results for this scenario and the Rankine-Hugoniot relationships can be used to determine the additional parameters. For the case when the final specific volume is greater than the initial specific volume, Dijken considered a system of thermodynamic processes. The final states of the powder will be calculated by heating at zero pressure from 0 to 4 followed by heating at constant volume from P_4 to P_3, as seen in Figure 1.6 The resulting pressure of the compacted powder will be given by

$$P_3 = \frac{2\Gamma(V_3)}{[\Gamma(V_3)(V_{00} - V_3) - 2V_3]} \int_{T_3}^{T_4} C_p(T), dT \tag{1.9}$$

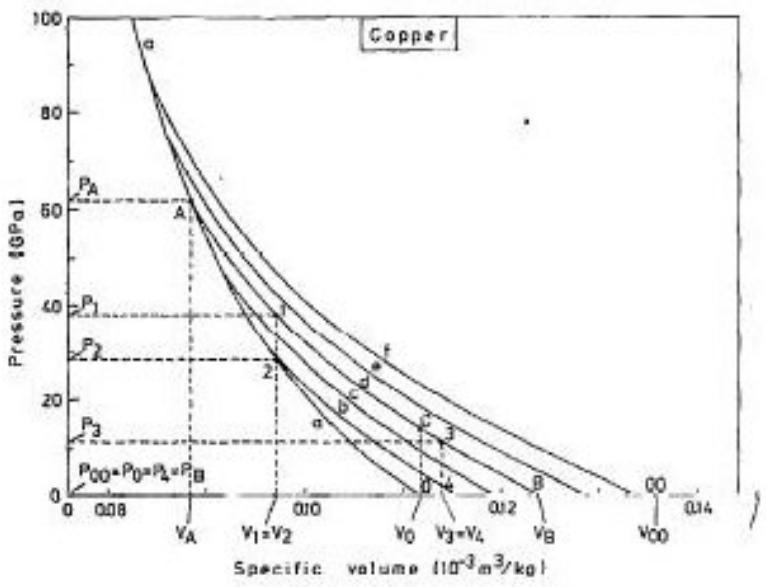

Figure 1.6: Copper Hugoniot and Equienergy Curves with P-V Points Labeled (From Dijken [2]

The parameters in Equation 1.9 can be chosen based in the case of V_{00} and V_3, with T_4 and $C_p(t)$ calculated utilizing several equations and estimations. The values of U_s and U_p can then be calculated based on P_3 for powders at varying intital temperatures.

1.4.4 Herrmann $P - \alpha$ Model and Proposed Modifications

The Herrmann $P - \alpha$ model considers the compaction of the powder in both the elastic and plastic region. Herrmann's goal was to separate the volume change from void collapse from that due to the compression of the material [15]. Herrmann assumes that the voids do not reopen during the time of interest and the shear strength is negligible. Herrmann's model considers only pressure as a function of specific volume and specific internal energy. The specific volume is then related to a dimensionless porosity term which is the ratio of the specific volume of the porous material and the specific volume of the corresponding solid material at the same pressure and temperature. Thus the equation of state of the solid material can be represented as

$$P = f(\upsilon_s, E) \tag{1.10}$$

and the porous material can be given by

$$P = f(\frac{\upsilon_p}{\alpha}, E) \tag{1.11}$$

where $\alpha = \frac{\upsilon}{\upsilon_s}$ is the dimensionless porosity term.

Herrmann then assumes the elastic and plastic ranges will have several expected properties to "ensure that the equation of state will be smooth and continuous at the point where the material becomes a solid." [15] The expected properties determine the coefficients of the polynomial of the plastic region (Equation 1.12), which can be greatly simplified if the polynomial is assumed to be quadratic.

$$\alpha = \alpha_0 + \alpha_1 P + \alpha_2 P^2 \tag{1.12}$$

Gourdin suggests that the Herrmann model has two pivotal advantages over other models. First, the Herrmann Model ensures that the porous equation of state will be consistent with the fully densified powder, and second, the factors attributed to the powder's large change in volume with the pressure are isolated [7].

Carroll and Holt proposed a modification to the Herrmann model in order to create a more accurate model at low pressures where the density differs from unity (or complete compaction) [16]. They assumed that a porous material was statistically homogeneous and isotropic so the material can be modeled as a homogeneous, isotropic solid material. In addition it was assumed that the volumetric response of the material is determined by the thermo-mechanical response of the matrix (solid) material, including the initial porosity. The volume average of the pressure in the matrix, P_m is given by

$$P_m = \alpha P \tag{1.13}$$

Herrmann suggested the two pressures were the same but Carroll and Holt argue that considering the transmitted force across a plane section of the porous

material will prove the pressures are not equal [16]. In other words, the Herrmann model would be valid only if the pressure in the matrix was uniform. The final requirement for the Carroll/Holt modification is the specific energies of the porous material and solid material are assumed to be the same. Combining the assumptions above with the definition of porosity from Herrmann the modified $P - \alpha$ model becomes

$$P = \alpha^{-1} f(\frac{\upsilon_p}{\alpha}, E) \tag{1.14}$$

Boade described a combination of the Mie-Gr*ü*neisen equation of state and the $P - \alpha$ model [9]. Porous Hugoniot data along with the equations below were used to define a curve at a pressure P_2 and the solid specific volume.

$$P_2 = \frac{P_H(V_{S0} - V_S - \frac{2}{G}) - P_1(V_0 - V_2)}{V_1 - V_2 - \frac{2}{G}} \tag{1.15}$$

where P_H is the $P - V$ Hugoniot for the solid material and G is the ratio of the Gr*ü*neisen parameter and specific volume at zero stress.

Boade discovered that the $P - \alpha$ coefficients of the polynomial did not agree with the experimental data. An exponential form of the α_2 coefficient was proposed below, where $\hat{a} = 0.254 kbar^{-1}$ described the experimental data.

$$\alpha_2 = 1 + (\alpha_1 - 1) \exp[-\hat{a}(P_1 - P_2)] \tag{1.16}$$

An additional Boade experiment was referenced that suggested the previous equation also described porous iron and graphite [3].

1.4.5 Numerical Methods

Numerous other models have been developed analyzing a portion of the densification process represented by Ferreira and Meyers. Meyers and Ferreira considered a model based on the energy used in void collapse, melting, and deformation to determine the pressure for shock compaction [17]. The Mie Gr*ü*neisen equation of state was then used to obtain the relationship between shock pressure and energy as a function of distention. Gourdin developed a model that determined the disposition of energy at the powder particle surfaces during

compaction. This model was based on the net energy deposited at the powder particle surfaces, the rise time of the shock wave, and the diameter of the powder particles [19]. From these parameters the temperature or thermal modification can be determined assuming melting is neglected. Vijoen developed a model based on the definition of enthalpy and the aid of Wu and Jing who considered an isobaric compression from the porous Hugoniot to a Zero Kelvin Isotherm [18]. This model also used the Mie-Gr*ü*neisen equation of state to determine the pressure of the solid Hugoniot. Viojen method was noted to be valid whether the porous system compacted "normally" or anomalously. Linde used a system of equations to represent the porous Hugoniot over several segments of the curve [11]. However, little discussion was given in the development of these equations other than a (Q method) based on an artificial viscosity and the use of a finite difference equation. The $P - \lambda$ model developed by Grady is based on the $P - \alpha$ model, but assumes that the pore collapse is initiated at sites with in the mixture and then engulfs the entire sample until compaction is complete rather than the uniform crush of pores throughout the sample [20]. In addition, the model assumes that the material exists in either an unequilibrated state or a pressure equilibrated state. The lambda term specifics the mass fraction of the mixture that has been compacted and exists in the pressure equilibrated state.

Numerical and computation methods emerged in shock physics research in the 1990's. The ability to accurately acquire pivotal physical, thermal, and Hugoniot properties both numerically and visually from a computer simulation eliminates the repetition of performing gas-gun experiments for countless conditions. In addition, the equations of states discussed above are readily available to be used in numerical computations and simulations. Finite element and difference methods along with direct numeric simulation have been the means to studying individual particles during shock compression. The two formulations of the equations of state for the finite difference and element methods are the Lagrangian and Eulerian (CTH) [21]. Both consist of a problem domain usually consisting of collection of polygons (quadrilaterals) in two dimensions known as a mesh, where each polygon edge is connected at a node. A Lagrangian formulation attaches the material directly to the mesh and allows the mesh to flow with the material as it deforms.

On the other hand, an Eulerian formulation applies a mesh that is fixed in space and the time step is unaffected by the material deformation. According to Benson, from the previously stated comparison; the Eulerian formulation is preferred over the Lagrangian [22]. A troublesome area exists when trying to obtain real-life particle distribution and porosity in two-dimensional space. Benson developed a pseudo-gravity method to numerically locate individual particles in the domain [22]. The particle is dropped into the box in the direction of gravity until the particle contacts another particle. The particle then slides along the surface of the contact particle until it contacts an additional particle, all acting as if under the influence of gravity. Benson used this procedure for rectangular and circular particles however irregular shaped particles could be used with increased difficulty due to the number of contact points.

The Mie Grüneisen equation of state and the $P - \alpha$ model appeared to be the least cumbersome and sufficiently address the concerns of modeling porous materials. The two methods are able to be coupled as was discussed by Boade to develop the appropriate Hugoniot relationships. As was quickly found in conducting the literature review, countless articles have cited Herrmann's P-alpha model and used the Mie- Grneisen equation of state which suggest their applicability and regard in the shock physics community. The P-alpha model perhaps offers the most favorable approach to modeling the compaction process by isolating the elastic and plastic regions. Both of these methods will also play a pivotal role in the use of numerical or computational methods of determining equations of state.
Experimental results are still essential and the shock speed and particle velocity at minimum must be determined before an equation of state can be applied. Also of great importance for this research, Dijken noted the following in order to obtain a "crack-free well-sintered material": high flyer-plate velocity, highly porous material, grain size should not be too small so the surface grains become hotter which favors sintering, initial temperature should be higher than room temperature which results in a higher temperature behind the shock leading to better sintering behavior, the batches should be large and thick so the material may remain for a longer time at high pressure and temperature, and a strong and heavy container material should applied to absorb the adiabatic compressive energy [23].

1.5 Experimental Results

The results and discussion below represent a brief overview of the major conclusions drawn from the articles pertaining to physical phenomena and equation of state use. Methods used to develop results need to be consistent and accurate. Numerous articles agreed that the transit time of the shock wave propagating through the powder must be calculated from the half max-value of the oscilloscope trace. No reasons were given for this method, but one can assume it is an average value based on the rise time record. If a "sandwich" target is used the transit time through insulator thickness must be deducted, using the impedance matching technique in order to determine the transit time through the powder only. The shock speed can then be determined from the definition of velocity [5]:

$$U_s = \frac{displacement}{\Delta time} \tag{1.17}$$

Vandersall in his compaction of a Mo+2Si powder noted several interesting observations [8]. The rise time at lower-stress magnitudes will be higher due to the "dissipative process responsible for powder densification" which leads to increased wave dispersion. At pressures greater than 6 GPa the data strays from the Hugoniot due to melting of the silica powder which occurs at 5GPa. Vandersall used the $P - \alpha$ model and determined the crush up strength to be 3.1 GPa, which continues up the Hugoniot until 6 GPa. The conclusion was drawn that the $P - \alpha$ model was the best fit from 0-4 GPa, the solid Hugoniot from 4-6 GPa, and at pressures above 6 GPa the powder melting will lead to large deviations from results. Vandersall also states in his $U_s - U_p$ curve that several data points at low particle velocities have higher shock velocities than the Hugoniot due to the assumption that the crush up strength is zero and as the particle velocity increases the shock wave speed decreases from the Hugoniot due to the melting of the silicon during compaction. The crush-up strength experience will also impact the ability of the powder mixture to react. A crush strength greater than the melt strength of the powders will inhibit shock induced chemical reactions while crush strengths lower than the melt strength favor the initiation of shock induced chemical reactions due to "plastic deformation and dispersion" during the crush-up process [8].

The verification of the experimentally obtained stress profile can be verified by comparing the peak pressure with the predicted Hugoniot pressure and by applying the fourth-power law developed by Grady [24]. The fourth-power law is a relationship between the peak stress and the strain rate within the shock wave. The particular peak stress and strain rated components can be visually seen in the Figure 1.7 below.

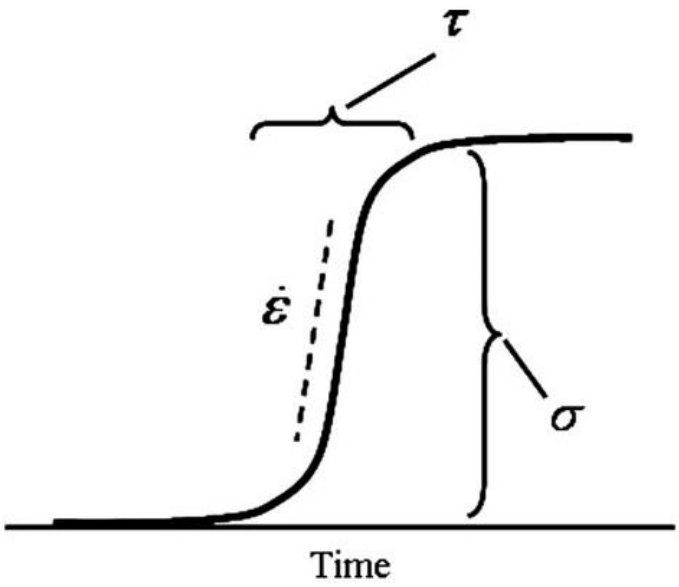

Figure 1.7: A steady structured shock wave with finite rise time

Grady states the fourth-power law is a common relation for a wide range of materials and shock amplitudes. The fourth-power law alters based on the materials used for compaction. The power law relationship for several materials is listed below:

1. $\dot{\epsilon} \propto \sigma$ Granular and Powder Materials
2. $\dot{\epsilon} \propto \sigma^2$ Laminated Composites
3. $\dot{\epsilon} \propto \sigma^4$ Metals

Grady notes that the fourth-power law is limited in the upper and lower limits of a pressure range. Also, component impedance differences will contribute to systematic behaviors that will not align with the fourth-power law.

In the compression of porous copper, Boade discovered a distinct three wave behavior in the stress record [9]. Boade suggested the three wave structure behaved

by the first wave compressing the powder at a low level with little to no deformation followed by a wave that overcomes the bonds between grains to push the grains into new positions with a new specific volume, and lastly a large amplitude wave causes large plastic deformation and flow regardless of grain shape or bonding. A linear relationship between transit time and sample thickness was noted along with pressure independence to sample thickness. Boade also noticed that the porous copper will not regain its initial specific volume, but will however follow the release wave similar to the solid material, thus remaining at a specific volume close to a fully densified material after compaction. The Hugoniot of the porous copper agreed with the Mie-Grüneisen equation of state and the solid Hugoniot with complete compaction occurring at 21 kbar. Boade also conducted an additional experiment on copper two years later using 10, 30, 50, and 100 micrometer powders [3]. Boade concluded that at 15 kbar the density of the compact was 98% of that of a copper solid and that the particle size had no distinct effect on the shock loading.

Linde performed experiments on porous copper and porous iron three years after the experiments of Boade [12]. None of the copper sample compacted by Linde experienced the three wave structure described by Boade. Precursor waves followed by a large amplitude wave were witnessed. Linde also observed that the specific volumes of the compacted porous materials were greater than the specific volumes of the solid material by 10% for iron and 6% for copper. There also existed considerable scatter in the copper Hugoniot data and post shot volumes which were attributed to oil existing in the specimens. Experiments performed with clean specimens resulted in data that agreed with the theoretical predictions. Also for oil-present iron specimens the final specific volumes were 2-5% greater than the initially solid material due to the wave release paths. Linde also discovered that the release paths for copper and iron were similar regardless if full compaction occurred. Both Linde and Boade created their copper powders from a sintering process; Linde using 5 to 10 micrometer powders while Boade purchased his from a manufacturer. The Mie Grüneisen equation of state predicted the specimen behavior above 20 kbar for clean copper and iron sample. Several years prior, Linde also performed gas gun experiments on graphite [11]. The final specific volume of the compacted graphite was closer to that of the initial density rather than the solid density. The

compaction of the graphite also did not depend on the orientation of the specimen. However it should be noted that a minimal number of trials were conducted on the graphite specimens.

Borg produced several experimental and numerical compactions of porous silica powder [25]. In the experimental results it was noted that at higher densities more complete compaction of the powder was observed. Also, the slope of the $U_s - U_p$ curve decreased as the densities of the powder decreased. Borg compared the compaction of the porous silica using the Mie-Gr*ü*neisen equation of state, the $P - \alpha$ model, the $P - \lambda$ model, and the snow plow method. The Mie-Gr*ü*neisen equation of state reproduced the experimental data the most accurate but required knowledge of the porous Hugoniot. All compaction models under predicted the release paths but reproduced the features of the experimental data better at higher projectile velocities. The $P - \lambda$ and snow plow method yielded similar results from which one can conclude that the presence of air does not affect the outcome since the $P - \lambda$ model considers air and the "snowplow" method does not. A conclusion was drawn that the $P - \alpha$ model had the most success since it includes the internal strength of the porous material as it is compacted. It was noted in an earlier simulation of the silica powder that the $P - \alpha$ and Mie-Gr*ü*neisen equation of state did not produce adequate results as the porosity increases.

1.6 Conclusions

The present direction and status of shock physics research has leapt forward greatly but has not abandoned the pillars of the past. Improvements in computational power have substantially advanced the ability to simulate rapid compaction of porous granular materials. Complex particle geometries and numerous variations of physical parameters such as porosity, particle size, temperature, and projectile velocity have broadened the landscape of analysis to what factors influence shock compaction. The Hugoniot relationships, Mie-Gr*ü*neisen equation of state, and the $P - \alpha$ model continue to embody the most intuitive and accurate means to convey shock wave interactions. Cold-welding of powder particles has been proven to be successful and acquire favorable characteristics of the compacted material. The awesome speed of compaction and

the frictional and deformational forces at the particle interfaces are able to bond particles to produce high hardness materials that eliminate the sintering process. With the continual development of new materials and powder mixtures, shock loading provides an additional means to analyze the usefulness of the powders and potential physical phenomena not realized in static applications.

CHAPTER 2

Experimental Apparatus

2.1 Apparatus Overview

The experimental apparatus for this research consists of a gas-gun, quasi-static compaction, and scanning-electron and optical microscopy systems. Each system will yield valuable insights into the response of the powder to various loading conditions. The gas-gun system allows for dynamic-loading through impact between a stationary target and a projectile traveling between 190-275 m/s. The dynamic loading using the gas-gun and flyer plate experiments will produce the samples to analyze using microscopy in addition to obtaining the shock speed and particle velocity required to develop the linear equation of state. The quasi-static compaction system will provide a method of compaction differing significantly from the dynamic by inducing a slow moving piston to crush the powder to a given load. Lastly, the scanning-electron and optical microscopy will reveal the microstructure of the powder as a result of the varying compaction methods. This will provide the basis for determining if the dynamic loading conditions can create samples with an improved microstructure to the statically pressed and sintered samples. The three research methods discussed above will be discussed in more detail below.

2.2 Gas Gun Overview

The gas gun system at Marquette University consists of three parts: Single Stage Gas Gun (SSGG), velocity measurement system, and stress measurement system. The SSGG's air delivery system, breech, and impact chamber were built by Thomas J. Downs (M.S. 2006) and later improved by Jeff Midday and through the present research [26]. The SSGG's air delivery system produces pressurized air for the breech to accelerate the projectile. The breech stores and releases the pressurized air sending the projectile down the barrel. The impact chamber houses the projectile-stationary target impact and provides a safety barrier for the gas gun

operators.

2.2.1 Air Delivery System

The air delivery system consists of an air compressor, refrigerated air dryer, filtration bank, and a gas booster, as shown in Figure 2.1. The air compressor produces compressed air regulated to 100psi for the gas booster inlet and gas booster driver through a tee at the air compressor outlet. The compressed air for the gas booster inlet travels through the refrigerated air dryer where the dew point is lowered to 37 degrees Fahrenheit. From the refrigerated air dryer the air enters the filtration system which consists of three coalescing carbon bed filters in series. The compressed air is in turn sent to a 2.25 liter cylinder which is emptied into the gas booster inlet at each compression. The compressed air for the gas booster driver is sent to a filter-regulator, where the pressure is regulated to 40 psi. At a 40 psi driver pressure and 100 psi inlet pressure the gas booster is capable of producing 2600 psi at the outlet. A three-way valve was piped to the gas booster outlet to allow operation of an additional gas-gun in parallel. All the piping in the compressed air system from refrigerated air dryer to breech is rated for 5000 psi. The air further compressed by the gas booster is then sent through the three-way valve to the breach.

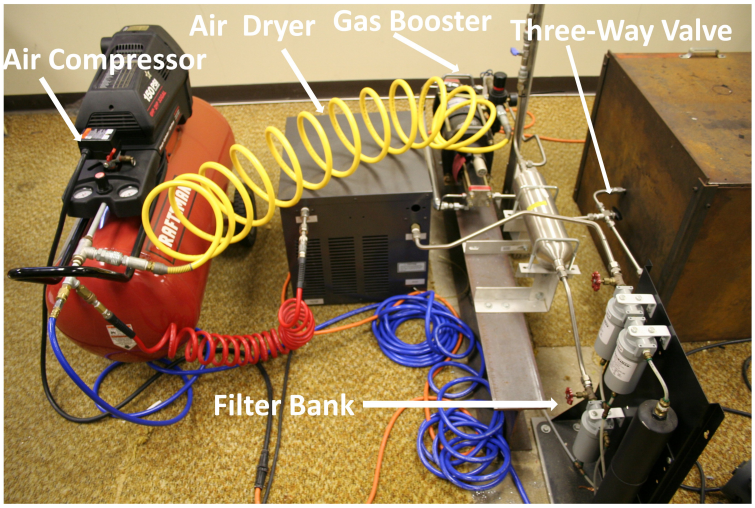

Figure 2.1: Marquette SSGG Air Delivery System

2.2.2 Breach, Barrel, Vacuum System and Projectile

The breech is the storage vessel for the compressed air leaving the gas booster. The breech is a three-piece aluminum cylinder with additional components, including o-rings, pressure gage, safety relief valve, copper foil shear disk, and vacuum port. O-rings are located at the middle aluminum piece interface, both copper shim-aluminum piece interfaces and at the barrel-breech interface. The projectile is located in the down stream section of the breech, with the rear of the projectile abutting to the copper shear disk. The compressed air leaving the gas booster builds up in the volume of the middle piece of the breach as the booster runs. When the pressure in the breech is equivalent to the burst pressure of the copper shear disk the projectile will be sent down the barrel. A pressure gauge is mounted to the middle piece of the breech, along with a pressure relief valve which will open if the pressure in the breech exceeds 1100 psi. The breech is also enclosed by a 1/4 inch steel secondary containment box as a safety precaution to gas gun operators in the unlikely event of a system rupture.

The barrel is a 36 inches long by 2 inch outside diameter and 1 inch inner diameter column of drawn over mandrel steel with fixtures for connecting to the breech, a vacuum port, and mounting the velocity measurement system and the targets.

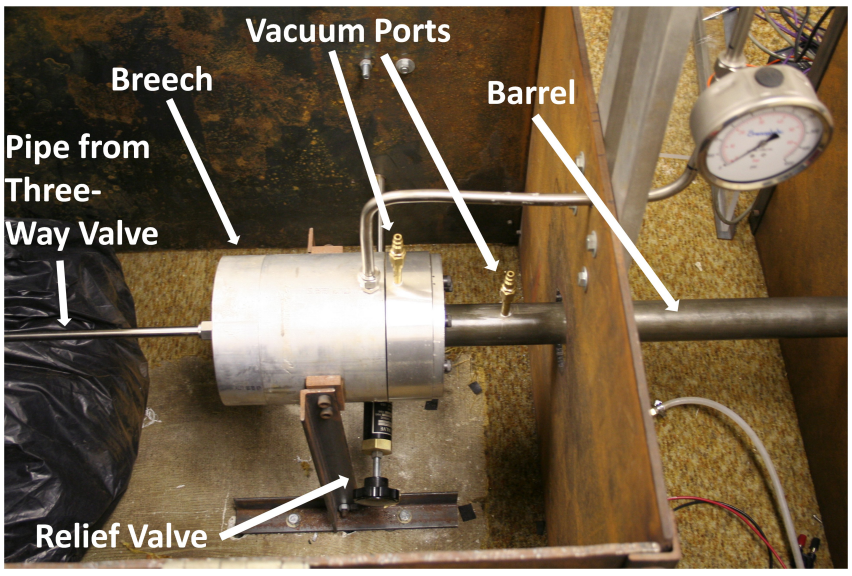

Figure 2.2: Marquette SSGG Breech and Barrel

The vacuum ports contained on the breech and barrel evacuate all air between the projectile o-rings and between the upstream projectile o-ring and the target at the barrel end. Figure 2.3 presents the vacuum system which is powered by a Hitachi 160VP CuteVac vacuum pump. The vacuum system is piped through two ball valves which evacuate the air from the breech and barrel. A pressure gage is placed between the two ball valves to insure there is no air entering the system. Upon launching the projectile the upstream ball valve connected to the barrel is closed to prevent pressurized air from entering the vacuum pump.

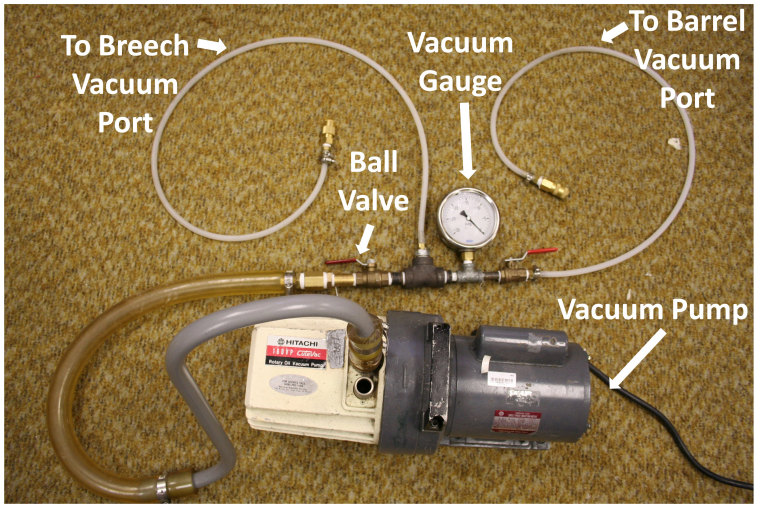

Figure 2.3: Marquette SSGG Vacuum Pump System

The projectiles are constructed of 1 inch nylon round with a 0.863 inch diameter aluminum flyer plate, see Figure 2.4. The nylon round was turned on a lathe to a diameter of 0.996 in. The aluminum flyer plates are 0.380 inches long to provide a large distance relative to the thickness of the target, so as to not affect the stress gages with reflected waves from the flyer plate. The flyer plate's were snug-fit mounted into the sabot via a 0.200 inch inset. Two o-rings were placed on the sabot to create a seal between the high pressure gas from the breech and the evacuated barrel. The o-rings also provide balance and rigidity to the projectiles with 0.025 inch compression so the flyer plate will be planar to the impact surface upon reaching the velocity measurement system and target. The flyer plate also undergoes a multiple step finishing process to ensure planarity through creation of a mirror finish. A Photron APX RS CMOS high speed camera was used at the target

barrel interface to insure the projectile was exiting the barrel properly with limited gas escaping prior to impact. Two consecutive images from the high speed camera at 10000 frames per second can be seen in Figures 2.5 through 2.7 The dimensions listed above for the projectile minimized the volume of gas leaving the barrel prior to impact to a negligible amount as viewed by the high-speed camera.

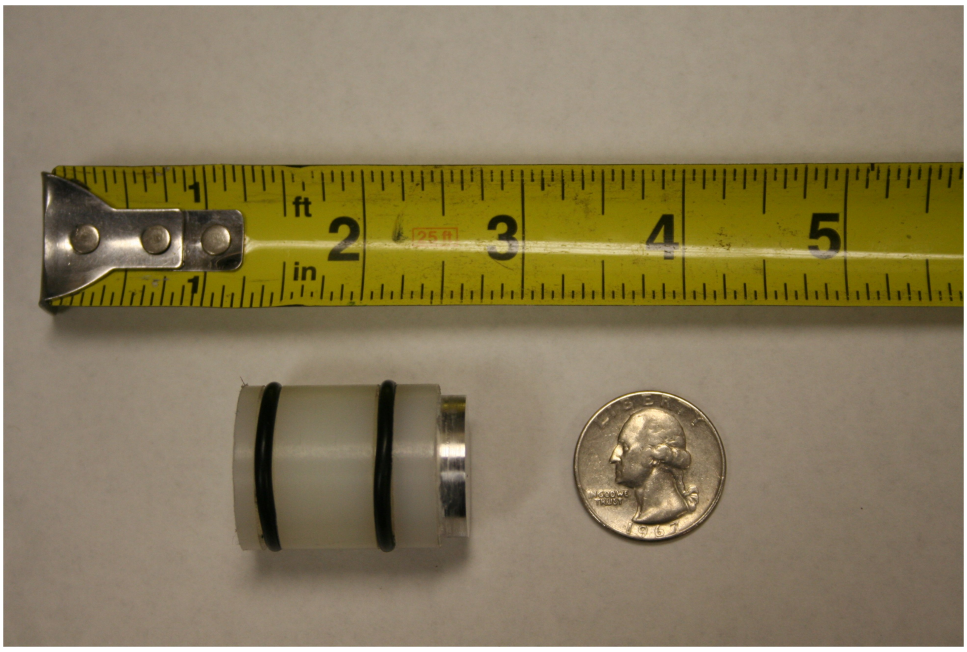

Figure 2.4: Projectile used in Marquette SSGG

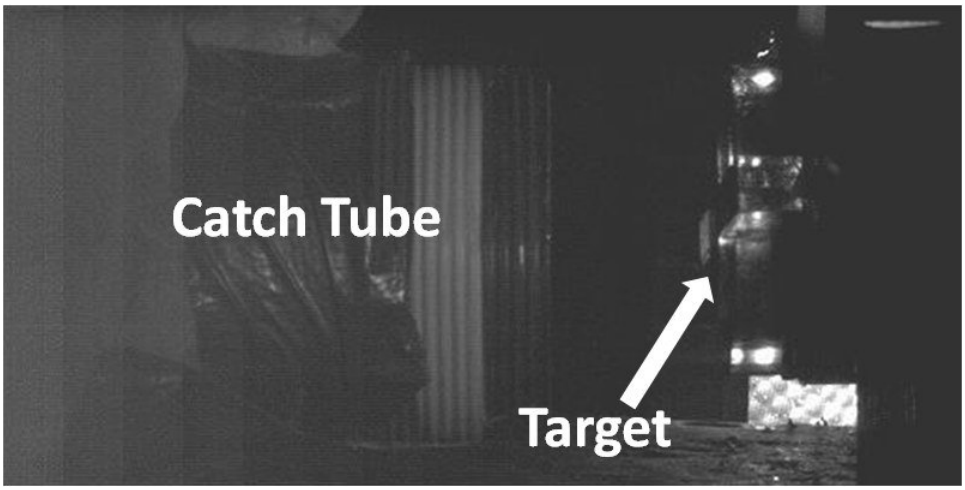

Figure 2.5: Image from High Speed Camera of Target Assembly

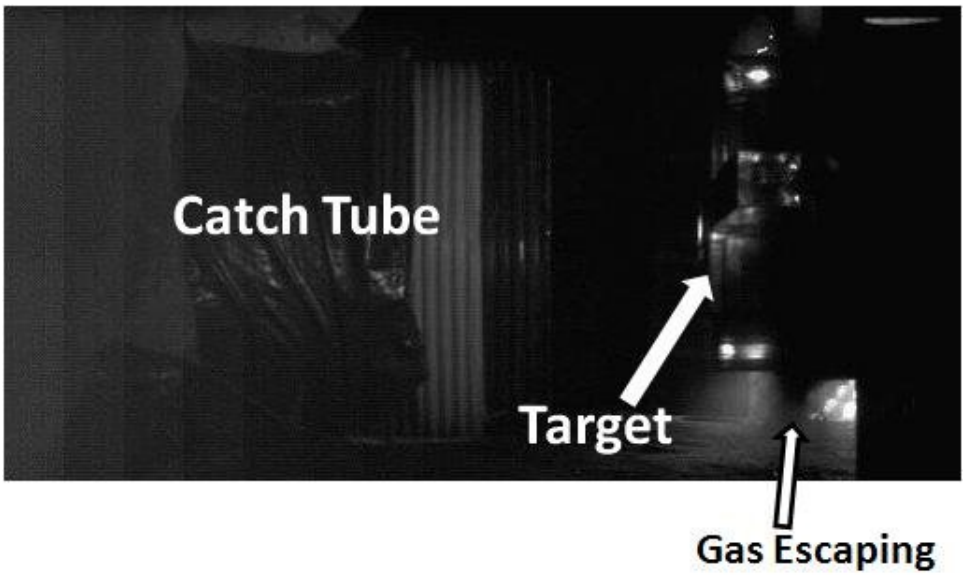

Figure 2.6: Image from High Speed Camera of Target Assembly 100 microseconds before Impact

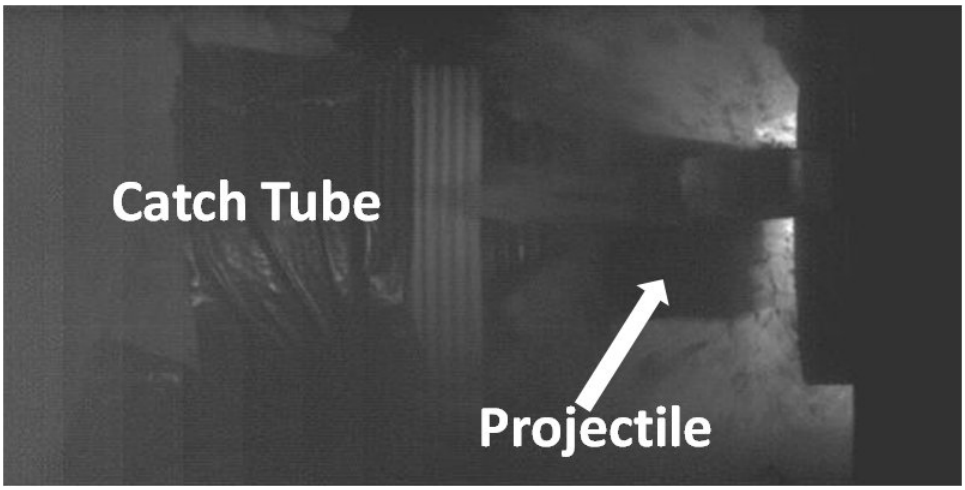

Figure 2.7: Image from High Speed Camera of Target Assembly and Projectile 1000 microseconds after Impact

2.2.3 Impact Chamber

The impact chamber houses the projectile-target collision along with the velocity measurement and stress measurement components and wiring. The construction of the impact chamber is 1/4 inch steel as used in the breech enclosure. A manual-jack is also located at the barrel end to rest the target and prevent stress on the breech system due to the weight of the barrel. There are also 1 foot square acrylic viewing ports for use of the high-speed camera and the appropriate lighting.

A catch-box is also placed at the barrel end to collect the target, projectile, and all debris exiting the barrel. The box is filled with cotton shirts to aid as a dampener for the weight of the target and associated metal components. The inside of the impact chamber moments before a flyer-plate experiment can be seen in Figure 2.8.

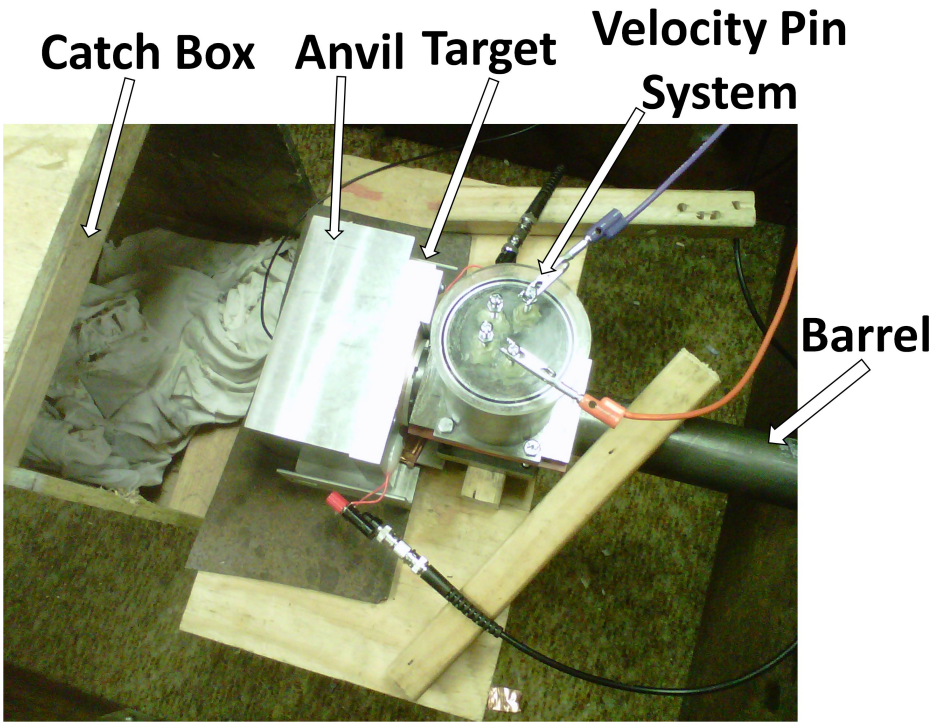

Figure 2.8: Experimental Set-Up for Target and Velocity Pin System and Impact Chamber

2.3 Velocity Measurement System

The velocity measurement system is to used obtain the velocity of the projectile prior to impact with a stationary target and provide camera and/or gage trigger. The system consists of a circuitry block, digital voltage supply, a vacuum sleeve with two o-rings, a vacuum lid with electrical connectors, and an oscilloscope. The circuitry block depicted in Figures 2.9, 2.10, and 2.11 is affixed to the barrel just upstream from the barrel end with a gasket and fasteners as seen in Figure 2.8. The circuit utilizes a parallel circuit with four branches. Each node consists of an isolated pair of parallel graphite rods (0.5mm pencil lead)or velocity pins, perpendicular to the flight of the projectile. These rods serve as four made-pins positioned in the barrel such that the flyer front face closes the circuit as it passes. Each graphite rod in the pair is connected to a common copper buss. Through the electrical connections on the vacuum lid, one copper buss will be grounded the other will receive 1.5V. The 1.5 V and corresponding current will prevent the graphite rods from distorting due to resistive heating. The electrical connections are then fed into an oscilloscope. Therefore, the velocity measurement system circuit is initially open. The velocity pins are spaced 19.89mm, 20.11 mm, and 19.92 mm apart. When the projectile makes contact with the initial pair of velocity pins, the circuit is complete and a rise of 1.5V will be seen on the oscilloscope for each velocity pin pair. From the oscilloscope, the user is able to determine the elapsed time between each circuit completion. The electrical connections are presented in Figure 2.12 and the entire velocity measurement system can be viewed in Figure 2.13. Utilizing the definition of velocity, Equation 2.1, the velocity of the projectile can be determined.

$$V = \frac{distance}{time} \tag{2.1}$$

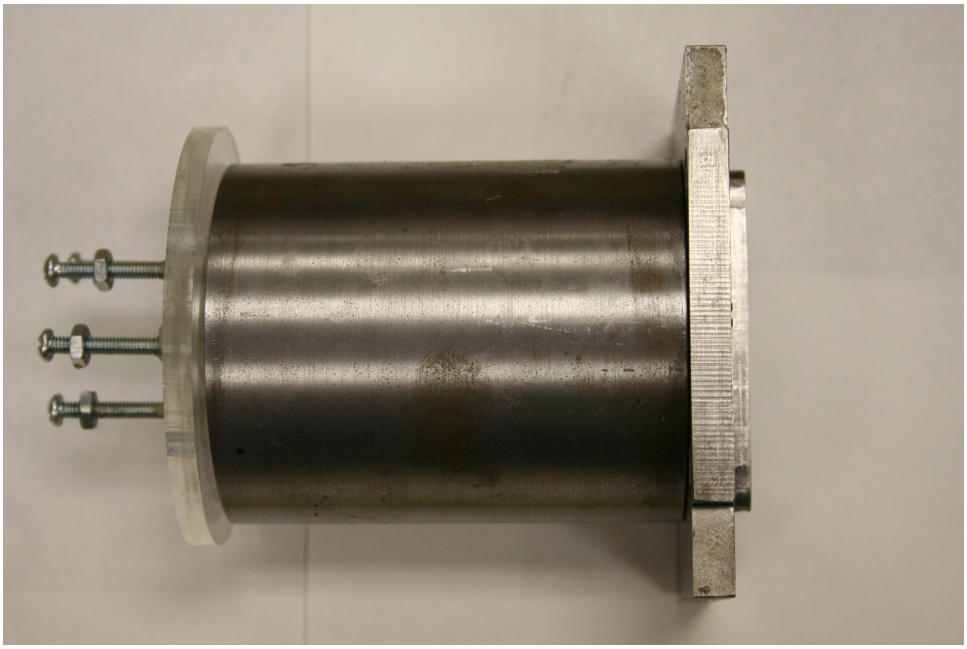

Figure 2.9: Velocity Pin System Assembled

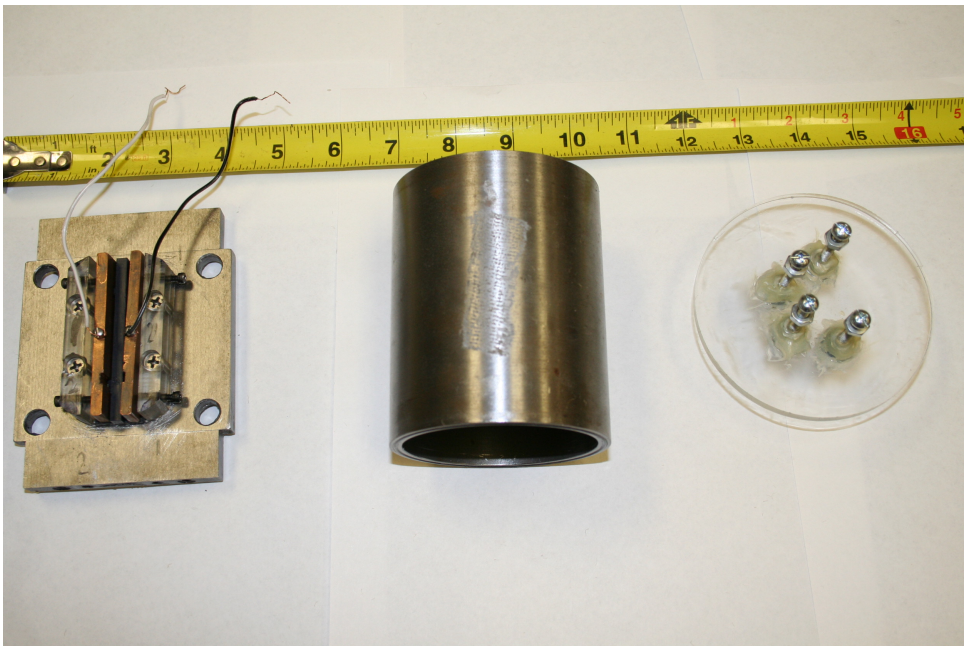

Figure 2.10: Velocity Pin Block, Vacuum Sleeve, and Acrylic Lid

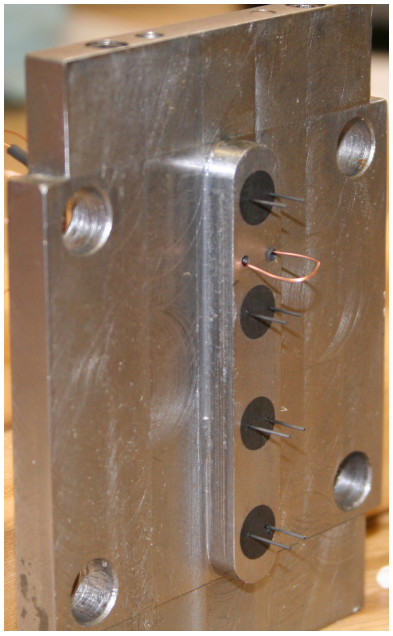

Figure 2.11: Bottom of Velocity Pin Block with Graphite Rods Visible and a Trigger Mechanism

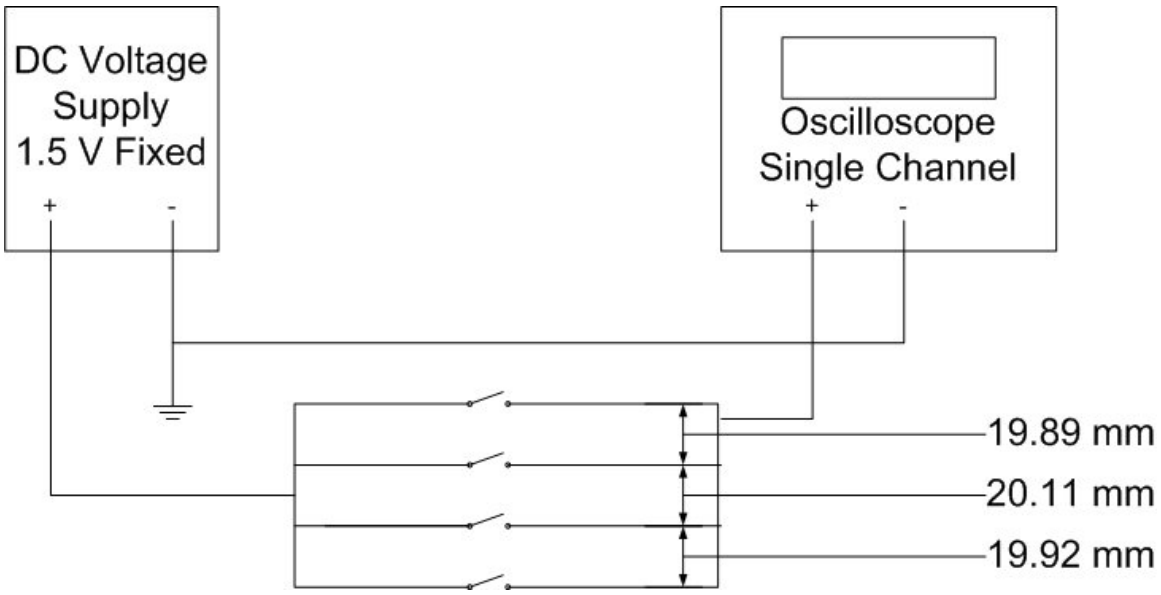

Figure 2.12: Electrical Diagram of Velocity Measurement Apparatus

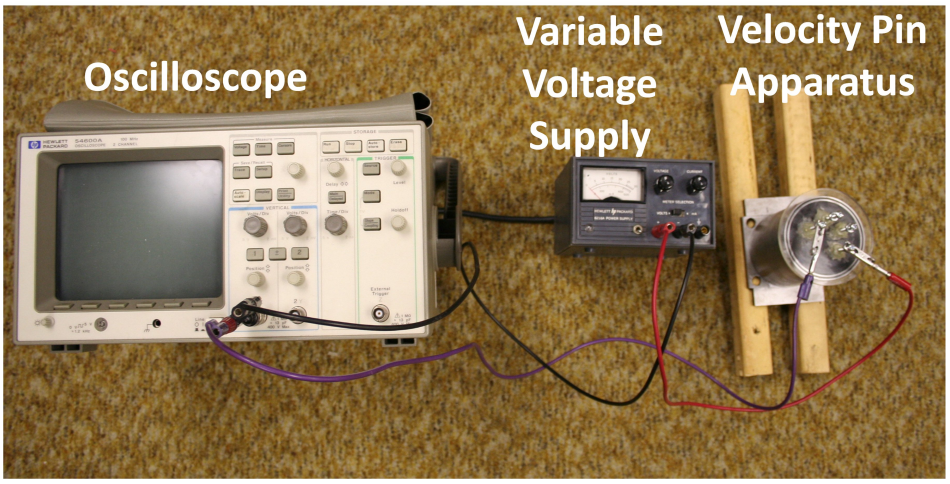

Figure 2.13: Velocity Measurement Apparatus including Oscilloscope, Variable Voltage Supply , and Vacuum Pin Block

As discussed in the previous section the barrel is under vacuum. Therefore the velocity measurement system is also under vacuum. The gasket between the circuitry block and the barrel, in addition to the o-rings on the vacuum sleeve which provides sealing between the vacuum lid and circuitry block, allow the barrel and its fixtures to remain under vacuum.

Circuitry isolators are also used in two locations of the circuitry block. The circuitry isolators are located between the steel block and the velocity pins and also between the copper busses and the steel block. The circuitry isolators prevent inadvertent grounding of the signal to the steel block and barrel. The material chosen for the isolators was nylon due to its machinability.

For all experiments performed on the gas gun, the oscilloscope was set with vertical divisions of 500mV/div and horizontal divisions of 50 microseconds/div. At an average projectile velocity of 250m/s, approximately 240 microseconds will elapse as the projectile passes from the first pair of velocity pins to the final pair. The oscilloscope was also set to trigger on 1/3Vmax or 0.5V of the first rising pulse. This was chosen since the time interval is of most importance rather than the specific place in time when circuit completion occurs. Figure 2.14 shows a typical velocity measurement trace corresponding to a projectile velocity of 243 m/s.

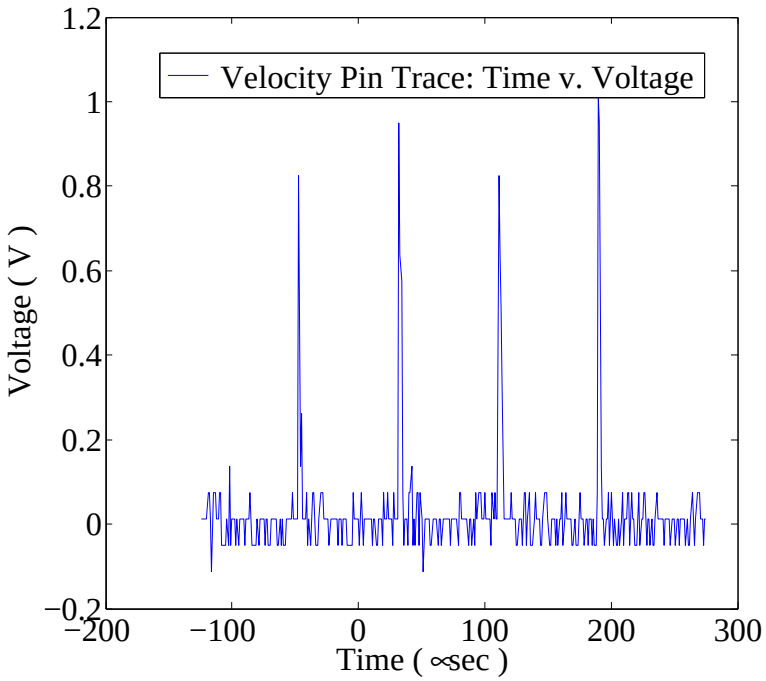

Figure 2.14: Velocity Measurement Trace for Projectile Traveling at 253 m/s. Note some time is negative based on the delay/pre-trigger set point of the oscilloscope

2.4 Stress Measurement System Overview

The Stress Measurement System is a multiple component system that is used to measure the stress of the planar impact between an incoming projectile and the stationary target. The Stress Measurement System yields valuable insight into the pressure waves transmitted and reflected through the various materials of the target, in addition to the time of arrival of the waves at a specific location in the target. From the pressure data the Hugoniot states of the material, specifically the heterogeneous mixture, can be determined, including the Shock Speed-Particle Velocity relationship ($U_s - U_p$), and the Pressure-Density (P-ρ) relationship.

2.4.1 Stress Gage Targets

The Stress Gage Targets contain the gages, triggering mechanism, and heterogeneous powder that will be used in the gas gun experiments. The target depicted in Figure 2.15 utilizes a "sandwich" technique. The "sandwich" consists of the following components in order from the barrel end: an aluminum driver plate, Mylar shim, manganin gage, aluminum piston, heterogeneous powder, copper shim,

Mylar shim,manganin gage, and aluminum back plate. The circular aluminum driving plate and piston were 2" diameter and the back plate was a rectangular 4" x 6" aluminum block. The aluminum housing visible in Figure F.10 was 2" inner diameter and 2.75" outer diameter with thicknesses varying from 0.165" to 0.200." The manganin gages are placed on a surface abutting to the material of interest to obtain the stress waveform propagating through the material [27]. The manganin gages were manufactured by Vishay Micro-Measurements with a grid resistance of 50 ohms. The manganin gages contain 84% copper, 12% manganese, and 4% nickel resulting in a high electrical conductive material with favorable mechanical properties and minimal change in resistance as a function of temperature [27]. Two gages are used in the stress gage target, one glued to the aluminum piston and the other glued to the aluminum back plate. The manganin gages from Micro-Measurements were not encapsulated and therefore a thin layer of epoxy under a Mylar sheet was applied over the gage and raked flat to protect the gage. In addition, each manganin gage has two legs from which two 2-3 inch pieces of 22AWG stranded copper wire was soldered and then encapsulated with epoxy to prevent damaged during construction and use. The copper shim was placed between the powder gage interface to prevent individual grains from penetrating the Mylar sheet and to amplify the signal to the back gage. The target will be fixed to the barrel end and therefore must also be able to hold and perform under vacuum. As result, the driver plate material with a polished mirror surface was blanked with a 2 inch die and hydraulic press to create the best available mate between the steel barrel and target since no gasket or o-ring could be installed.

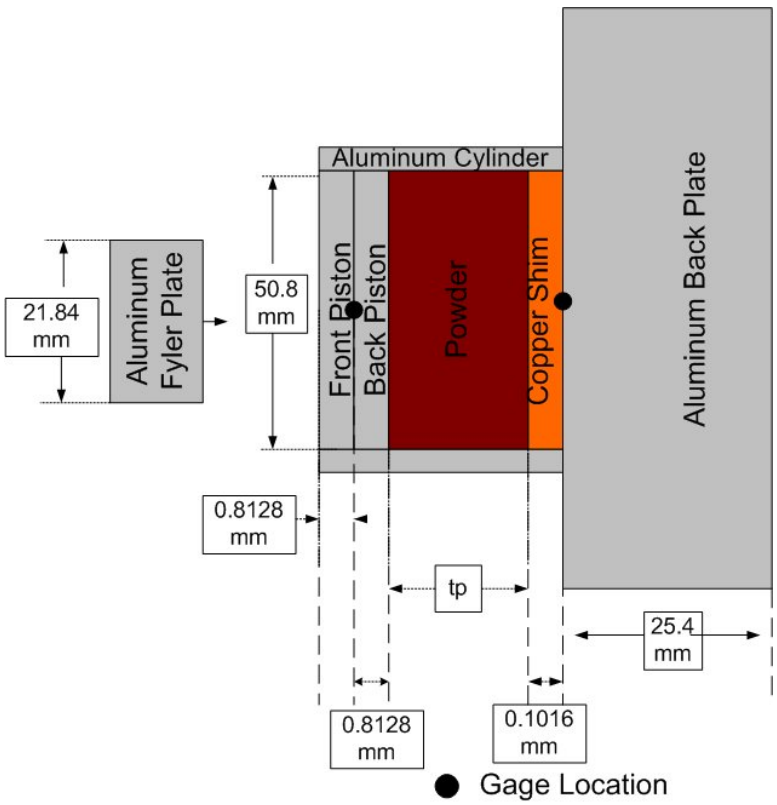

Figure 2.15: Diagram of Material Components and Location in Stress Target

The target will operate as follows based on an incident projectile with an aluminum flyer plate. The projectile will impact the 0.032" aluminum drive plate creating a stress wave from the aluminum-aluminum interface. The wave is transmitted through the driver plate to the gage and through the 0.032" aluminum piston. At the aluminum-powder interface an impedance mismatch exists transmitting and reflecting this initial stress wave. The transmitted wave will propagate through the powder and will also be reflected back through the aluminum piston to the front gage. The transmitted wave through the powder will reach the 0.004" copper shim interface and the impedance mismatch will again transmit and reflect the incident stress wave. The transmitted stress wave through the copper shim will reach the copper shim-aluminum back plate interface where the back manganin gage is located. An impedance mismatch also exists at the copper-aluminum interface sending the stress wave with adjusted amplitude through the aluminum back plate, which at 1.00" is considered infinitely long.

It was found that a copper shim was necessary to protect the back gage from

the powder. In experiment 21, where there was no shim, the back gage immediately went to an open circuit on the oscilloscope. Under loading the mylar shim will stretch and the granular particles can penetrate the mylar and disrupt the gage response, which will prevented by the epoxy. A metallic material, such as copper, above the mylar shim will also act as an amplifier of the stress wave based on the impedance match of Mylar and a metal.

A 0.086" through-hole is also drilled through the target for placement of a time-of-arrival detector. The time-of-arrival-detectors (TOADS) were purchased from Dynasen Inc and are constructed with brass inner and outer conductors. The TOADS are piezoelectric and therefore do not require any external power supply. When the projectile impacts the pin a crystal and silver epoxy are crushed shorting the inner and outer conductor [28]. The crushed pin produces a 70 volt, 0.4 microcoulomb pulse of 0.4- 0.5 microsecond duration for a 2kbar stress interaction. The TOADS extend roughly 0.080-0.100" above the surface of the aluminum drive plate [28]. The TOADS were also placed in heat shrink-fit to act as a circuit isolator and glued and epoxied at the driver plate and back plate to fill the voids left by the drill hole and therefore be able to hold vacuum.

2.4.2 Stress Data Acquisition System

The stress data acquisition system receives the signal from the target upon impact and outputs a digital signal to an oscilloscope. The components required are a piezoresistive pulse power supply, a variable resistance box, an oscilloscope, and seven BNC cables of varying lengths and ports. The general diagram for the data acquisition system can be seen in Figure 2.16 and in practice in Figure 2.17 . In general, the breaking of the piezoelectric pin triggers the oscilloscope, which in turn triggers the piezoresistive pulse power supply. The piezoresistive pulse power supply is a Dynasen Inc, model CK2-50/0.050-300. The piezoresistive pulse power supply then receives the signal from the stress targets and relays the information to the oscilloscope for viewing. The oscilloscope used on the stress data acquisition system is a Agilent Technologies DSO6054A. The oscilloscope is set to a time resolution of 5 microseconds/div and a voltage resolution of 50mV/div. The configuration of the electrical wiring allows the oscilloscope to sample at 4GSa/s which will allow

200,000 samples to be taken over the 50 microsecond experimental interval or an effective sample frequency of 4000 samples/microsecond. The oscilloscope is set to acquire a rising trigger from the breaking of the piezoelectric TOAD at 750mV with a delay of 8 microseconds from the beginning of the display window. The trigger sent from the oscilloscope to the piezoresistive pulse power supply is a 0-2.5V level output into a 50 ohm connector with a rising edge delayed 17 nanoseconds from the oscilloscopes trigger point [29]. The pulse power supply is designed to excite shock pressure gages and produce usable electrical signals in the presence of pressure waves [30]. The pulse power supply operates through essentially a Wheatstone bridge resistor network that is completed by the manganin gage. [30]. The trigger from the oscilloscope turns on a transistor from a timing circuit that allows a capacitor to discharge into the resistor network [30]. The capacitor discharges a quasi-rectangular pulse of 100 microseconds to allow for the experiment to complete [30]. The pulse power supply will then output the resistor bridge output voltage which is representative of the change in resistance of the gage. The Dynasen power supply was set to operate in 50 ohm mode with a 75 ohm output. The 75 ohm output was used so a direct measurement of the unattenuated bridge output voltage could be recorded while preserving the 20 nanosecond response time of the bridge network [30]. As a result, a 75 ohm terminator must be placed at the oscilloscope input to prevent wave reflection from the bridge output [30]. The capacitor voltage for each gage channel was set to 50V with a settling point of 46V. In earlier experiments, the gate was inputted into the oscilloscope to depict the moment in time and space where the pulse power supply triggered, but increased reliability of the system allowed for the removal of this information in favor of increased sample rates. The timing and circuitry discussed above between the piezoelectric pin and the oscilloscope and the oscilloscope and the pulse power supply is of utmost important to not only acquire the signal in the proper event window, but to also prevent the gages from burning due to the voltage and current applied by the pulse power supply. If a power supply was connected to the gage that ran continually the heat generated would have a detrimental effect on the gage due to resistive heating, therefore a timed pulse is required to preserve the gage for the duration of the experiments.

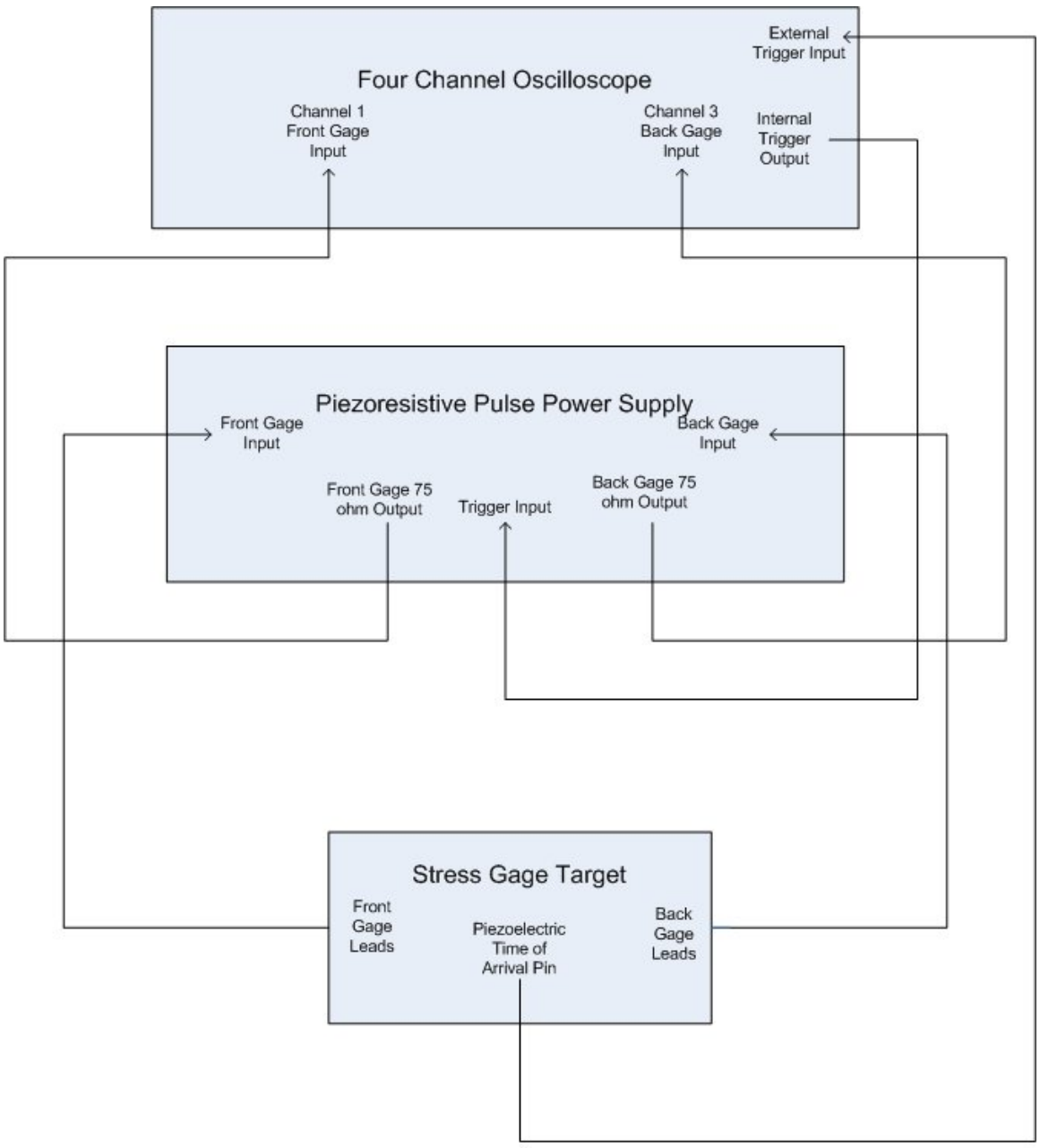

Figure 2.16: Connection Diagram for Stress Measurement Apparatus

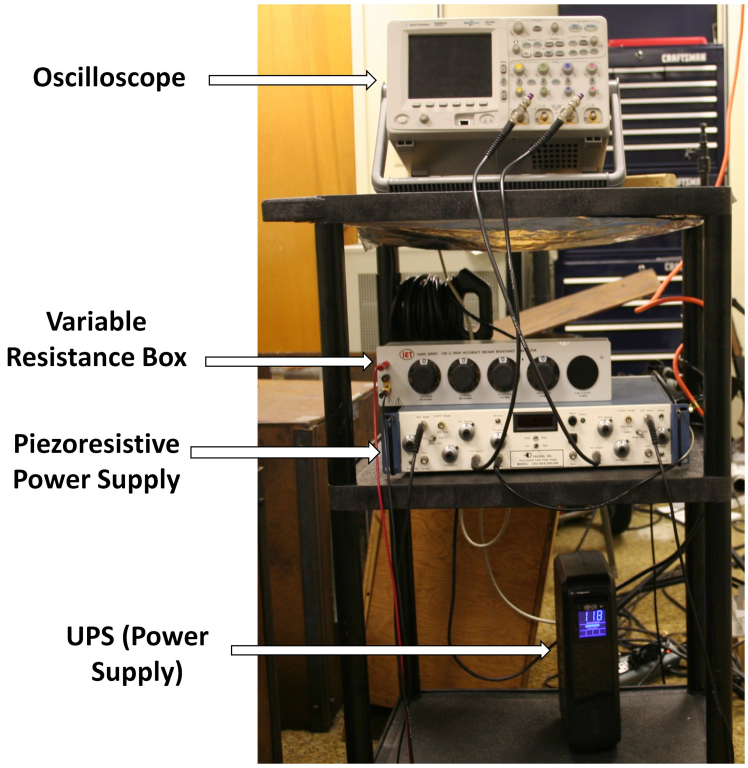

Figure 2.17: Instrument Cart Containing Stress Measurement Apparatus Hardware

In order to receive the proper response of the gage to the pulse power supply's bridge network, the bridge must be balanced and calibrated around the gage resistance. The bridge was balanced by placing the oscilloscope at high resolution (10mV/div) and connecting the gage to the pulse power supply. The balance procedure consists of adjusting the balance control and firing the pulse power supply observing the output on the oscilloscope. The bridge will balance around 000 to -001 on the digital display. When the output to the oscilloscope was a flat pulse of 0V amplitude the bridge is balanced. This process was repeated for both the left and right channels (ie. both gages). Once the bridge is balanced the gage is removed from the network and replaced with the variable resistive box. The variable voltage supply was then adjusted and fired in order to determine the resistance of the gage. Once the variable resistive box is balanced in accordance with the bridge, it is adjusted off balance to simulate the gage changing resistance as a result of loading.

Thirty-six data points were then taken about the actual resistance of the gage to create a profile of resistance and voltage. The change of resistance of the

gage was then calculated for each trial using

$$\%R = \frac{R - R_0}{R_0} \tag{2.2}$$

The change in resistance and corresponding voltage was then plotted, see Figure 2.18. A second order polynomial was fit to the plot due to the parabolic nature of the plot and for simplicity in solving for the roots of the fit. The calibration curve allows for the waveform on the oscilloscope to be related to pressure based on the change of resistance for a given voltage. The resulting change in resistance can be related to pressure using the experimental manganin gauge calibration polynomials developed by Sandia National Laboratory 2.3 and Rosenberg 2.4 below [31] [32].

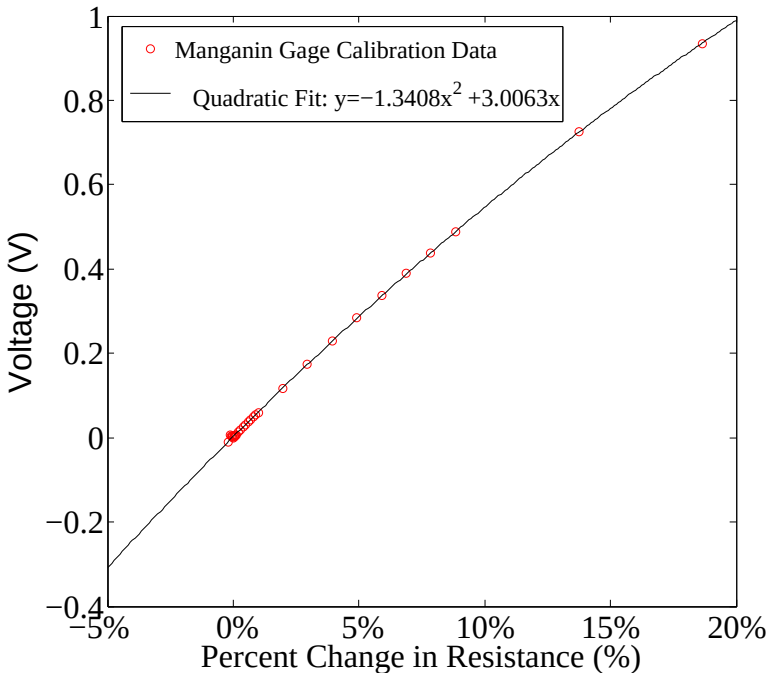

Figure 2.18: Sample Calibration Curve for Pulse Power Supply about 51.3 ohms

$$P(GPa) = 5.5027(\frac{\Delta R}{R_0}) - 0.2063(\frac{\Delta R}{R_0})^2 + 0.0061(\frac{\Delta R}{R_0})^3 \tag{2.3}$$

$$P(GPa) = 0.572 + 29.59(\frac{\Delta R}{R_0}) + 95.20(\frac{\Delta R}{R_0})^2 - 312.74(\frac{\Delta R}{R_0})^3 + 331.77(\frac{\Delta R}{R_0})^4 \tag{2.4}$$

The above equations are applied to each data point of pressure and time, in order to convert the waveform on the oscilloscope from Voltage-Time space to

Pressure-Time space.

2.5 Static Compaction Experiments

The Static Compaction Experiments were conducted using a 810 Material Test System manufactured by the MTS Systems Corporation with a MTS 442 Controller and 413 Master Control Panel. The experiments are used to analyze the powders response to quasi-static loading. The MTS can operate in both a stroke and load control mode. The load control mode was chosen due to unfamiliarity with the load associated with a given displacement. The apparatus depicted in Figure 2.19 was created to perform the static compaction tests, consisting of a mounting flange, compaction cylinder, compaction piston, platen, and associated fasteners. The diameter of the platen was 2.997" and the diameter of the piston was 1.440" yielding a ratio of 2.08:1. The compaction cylinder was filled with approximately 12 grams of powder for each trial. The load was manually varied from 0-20 kips based on the controller range. The available ranges were 0-2kips, 0-4kips, 0-10kips, and 0-20kips. The stroke measurement system was set to a range of 0-.25 inches. Each range is comprised of a 0-10Volt output, which can be translated to load or stroke using the manufactures calibration data of voltage and corresponding percent load or stroke. Therefore for each trial, the load and stroke voltages were recorded for ten points along the load range. From the voltages the pressures and densities observed by the powder were recorded and plotted in pressure-density space.

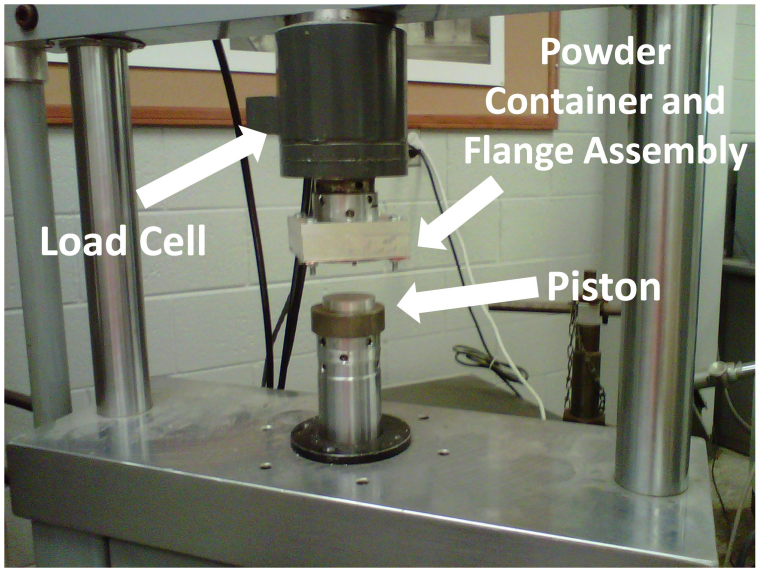

Figure 2.19: MTS Set-Up for Static Compaction Experiments

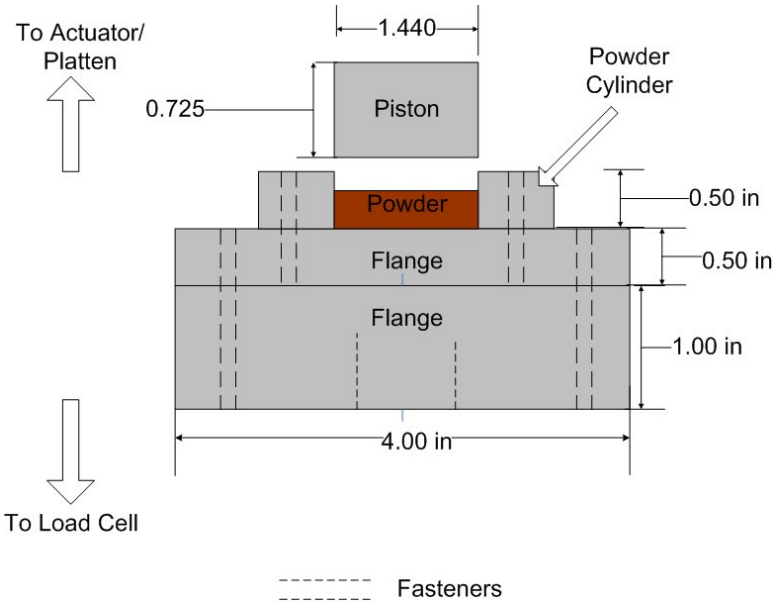

Figure 2.20: Schematic of Static Compaction Apparatus with Flanges for Mounting to MTS

2.6 Heterogeneous Powder Creation Process

The heterogeneous powder consisting of 42% copper, 19% iron, 18% graphite, 17% silicon-dioxide, 3% molybdenum-disulfide, and 1% tin was created using a simple mixing process. The key characteristics of each constituent including grain size and apparent density can be seen in Table 2.1 The mixtures were created

to obtain 200g of total sample. A Sargent Welch Scientific Weighted Scale Model S3223 was used to measure the mass of each constituent of the powder mixture. Each component was then added to a Thumbler Rock Polisher to be mixed. For each 46.3 grams of powder two drops of corn oil was added to the mixture or roughly nine drops per 200g. The density of corn oil is 0.92 g/cm3. The corn oil acted as a binder to prevent the individual powder grains of a common material to coalesce or diffuse after mixing and allow for a heterogeneous mixture. After five minutes of mixing the procedure was complete and the mixture was emptied into a common container. The resulting mixture had the following properties and distributions:

Table 2.1: Heterogenous Mixture Constituent Properties

Constituent	Percent Volume (%)	Apparent Density (g/cc)	Particle Size Distribution (μ m)	Solid Density (g/cc)
Copper	42.5	2.55	25<x<100	8.924
Iron	18.72	3.12	50<x<150	7.87
Graphite	18.3	0.51	200<x<400	2.16
Silica	17.4	1.30	300<x<500	2.197
MoS_2	2.8	1.20	x<100	4.79
Tin	0.3	3.94	x<125	7.31

The density of the mixture was determined using a graduated cylinder and a weighted scale to utilize the definition of density.

$$\rho = \frac{Mass}{Volume} \tag{2.5}$$

Both the poured density and tapped density was determined. The poured density and tapped density were experimentally determined to be 2.423 g/cc and 2.691 g/cc respectively. This is in comparison to the theoretical density of 2.030 g/cc. The theoretical density was determined, using Equation 2.6, by summing the product of the manufacturer's apparent density and volume fraction for all of the constituents in the mixture. In addition, using the solid density of each component, the solid mixture will have a theoretical density of 6.240 g/cc.

$$TheoreticalDensity, \rho = \sum_{i}^{n} \rho_i * \phi_i \tag{2.6}$$

where ρ_i and ϕ_i are the apparent density and volume fraction,respectively of

constituent i.

Microscopy was also performed on the pre-impact powder using a Lintron No. 0536 Upright Optical Light Microscope equipped with Scope Image Advanced to stream live video of the sample and acquire images at 50X-100X magnification. The sample was poured onto a glass wafer and smoothed to a level plane using an additional glass wafer. The microscopy allowed a method to capture each constituent in the sample in order to visualize the morphology/geometry of each grain. The grain geometry will provide a means of comparison to the post-impact specimen in addition to supplying geometry for entry into two-dimensional computer code. The bulk sample was also analyzed while varying the focal length to focus on different sample depths. Focusing on different depths depicted how the grains will orientate themselves in the powder and the porosity in a given plane. A sample image from this process is displayed in Figure 2.21.

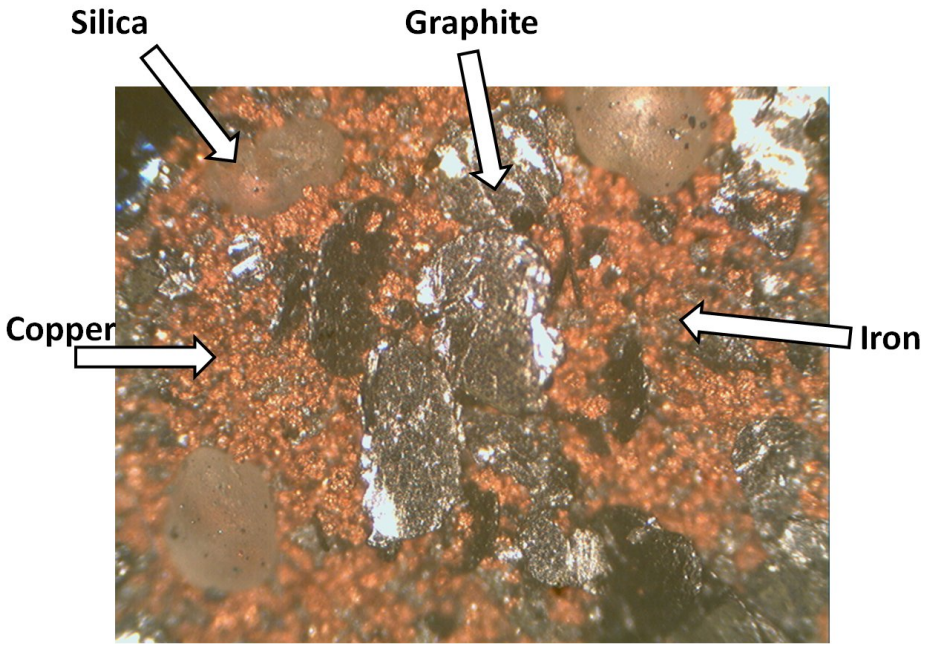

Figure 2.21: Heterogeneous Powder Viewed through Upright Microscope at 100X Note MoS_2 and Tin are not visible.

2.7 Optical Microscopy of Post-Impact Powder Specimens

The post-impact and statically pressed and sintered specimen's grain structure was imaged using an Olympus PME3 Inverted Light Metallurgical

Microscope with a Spot Insight Digital Camera to photograph the sample. Spot Basic software was used to stream live video and capture the image for analysis. The cross-section of the samples was analyzed from the center of the impact location due to the expected stronger bonds than at the sample peripheral. The samples were molded in Lecoset100 Resin Polymer and Resin Monomer. The mold was then polished beginning with rough sandpaper of 80, 240, and 320 grit. The mold was then further polished using 400 and 600 grit sandpaper on a rotating table before polishing on a 1.0 μm table with A_2O_3 powder to create a defect free surface. The microscope lenses allowed for magnification of 25X, 50X, 100X, 200X, and 500X. The samples were also swabbed with Ammonia Hydroxide for etching. The Olympus microscope was then used to view the sample's grain boundaries and acquire several images.

The porosity of the specimens was determined using the image manipulation software GIMP (GNU Image Manipulation Program) and the imaging software *SimplePCI*. The pores were defined in the optical images and turned black in GIMP. All the constituents not considered pores were colored white. The resulting black and white image was imported into *SimplePCI*. *SimplePCI* was used to identify the black (pores) as a region of interest and calculate the fraction of black to white in the image or the porosity of the image.

In addition, a JEOL JSM35 Scanning Electric Microscope (SEM) and a Trancor Northern Energy Dispersive Spectroscopy (EDS) were used to gain additional knowledge of the compaction of the powder specimen. A Technics Hummer 1 Sputter Coater was used to coat the specimens with gold-palladium prior to using the SEM and EDS system. Images were taken using the SEM at varying magnification from 500X to 1000X. EDS was then performed to identify each constituent and aspects of the sample that were unexpected or unidentifiable.

CHAPTER 3

Experimental Validation

3.1 Experimental Validation Overview

Before the results could be fully analyzed the velocity pin system and stress measurement system had to be functioning appropriately. The velocity pin data was reduced for each experiment and compared to the work conducted by Downs [26]. The projectile velocities were compared based on the shear disk used in the experiment. The stress measurement system data was also reduced and analyzed using an impedance matching technique, the fourth-power law, and wavelength comparison. The impedance matching technique will yield knowledge when comparing the peak stress of the front gage, while applying the fourth-power law will conclude if the pressure waveform is consistent with the materials used.

3.2 Velocity Pin System

The use of two different methods to measure the velocity of a projectile in the Marquette SSGG will improve the understanding of the gas-gun's behavior and the accuracy of the measurements. Downs utilized a laser and optical measurement system at two known locations in the gun barrel. The passing projectile disrupts the laser beam to the optical collector and relays a voltage decrease to the oscilloscope. The two disruptions at each sensor location results in the time difference required to calculated velocity. The velocity measurement system used in the present research as discussed in Section 2.3 consisted of four graphite "make pins" in series, a known distance apart, wired in a parallel circuit. The passing projectile would complete the circuit inducing a voltage spike on the oscilloscope from which the time difference could be obtained. The moment in time the voltage spike occurred was taken to be the first notable rise in voltage. A percentage of the voltage peak was not taken into consideration due to the limited functionality of the oscilloscope measurement cursors. Shear disk thicknesses ranging from 0.004" to 0.008" were

used in characterizing both velocity measurement systems by providing different pressures to propel the projectile. The tables below depicts the average of all variables collected in the trial experiments at each shear disk.

Table 3.1: Velocities Achieved in Downs Research (Average)

Note Burst Pressure Uncertainty is up to ± 100 psi

Shim Size (in)	Burst Pressure (psi)	Projectile Mass (g)	Diameter (in)	Velocity (m/s)
0.004	360	14.392	0.994	201.98± 3.34
0.005	450	14.421	0.994	213.30± 3.34
0.006	560	14.375	0.993	233.08± 3.34
0.007	680	14.438	0.994	256.08± 3.34
0.008	710	14.396	0.994	266.27± 3.34

Table 3.2: Velocities Achieved in Present Research (Average)

Note Burst Pressure Uncertainty is up to ± 100 psi

Shim Size (in)	Burst Pressure (psi)	Projectile Mass (g)	Diameter (in)	Velocity (m/s)
0.004	400	21.994	0.997	206.68± 2.15
0.005	500	21.494	0.996	216.39± 2.35
0.006	600	22.078	0.997	241.63± 2.93
0.007	750	21.917	0.996	257.32± 3.10
0.008	800	22.335	0.997	271.14± 3.68

Apparent from the tables above is the method in the current research resulted in more massive projectiles experiencing higher velocities across the entire shear disk range. The current velocity measurement system with the adapted projectile achieved velocities on average that were 1.95% higher with a projectile mass increase of 52.5%. It is important to note that the averages are not based on the same number of trials since the goal of the current research was to consider the stress measurement system and the heterogeneous mixture. However, the 0.007" shim contained a similar number of trials and therefore may be used to characterize the system as a whole. The 0.007" shim produced velocities that on average were 0.48% higher than an increased projectile mass of 51.8%. The current method also

improved on the repeatability of the velocity measurement with a standard deviation of 4.63 m/s compared to 5.50 m/s in the research of Downs. A possible reason for the increase in projectile speed is the current research utilized a larger diameter projectile, coupled with o-rings, a partially bored center and an evacuated barrel. This allows for an improved seal between the high pressure gas behind the o-rings and the evacuated air downstream in the barrel, in addition to the adjusted pressure differential from an atmospheric barrel and a barrel at 29.5 inHg. The poor sealing mechanism may have also contributed to errors in the time measurement in the Downs experiments as the air passing the projectile disrupted the laser reading before the projectile reached the laser location. The previously discussed phenomena was encountered in this research as poor sealing in early trials prevented the oscilloscope from triggering due to shifting of the projectile resulting in no contact with the graphite rods or the high pressure air breaking the graphite before the projectile arrived. Also, an important note is the uncertainties in the velocity measurements, though similar, are not the result of the same systematic errors. The greatest source of error attributed to the work of Downs was in measuring the distance between the two laser-sensor assemblies, while the greatest source of error in the current research was the time measurement of the oscilloscope. In the current research a microscope was used to precisely measure the graphite location to 0.005mm while the oscilloscope could only measure time accurately to 1 microsecond. Down's, on the other hand, was able to accurately measure time to 0.3 microseconds. The time measurement system could be vastly improved by utilizing a similar scope as used by Down's and acquiring the data in an ASCII file. The resulting uncertainty in the time measurement would be 10.5 nanoseconds or 1.5% of the current oscilloscope uncertainty.

3.3 Stress Measurement System

The ability to have a stress wave that agrees with current models will allow the data to be reduced further into development of an experimentally measured equation of state. The experimental equation of state to be developed will provide the missing link to solving the Rankine-Hugoniot Equations (Equations 1.1-1.4). However, to create this equation of state for the heterogeneous mixture, the stress

measurement system must be producing reliable data. In order to compare the stress waveforms to current models, the data was reduced according to the description in Section 2.4.2, resulting in pressure and time data for each experiment. The cumulative experiment summary can be seen in Table C.1. The goal of the stress measurement system was to correctly acquire the waveforms for the gages embedded before and after the heterogeneous mixture. This goal was accomplished in trials 22-26, and therefore the analysis of these trials will form the crux of the research. However, a brief analysis of the first two experiments (10 and 12) to successfully acquire a stress waveform on a single gage target will be discussed. A few of the variables to be discussed in the following sections and chapters can be observed in the Figure 3.1 below:

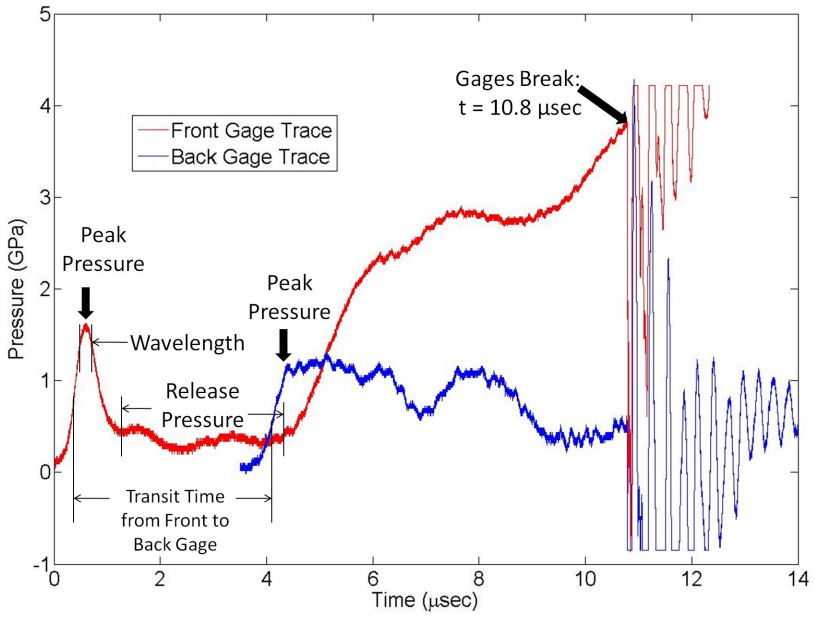

Figure 3.1: Sample Two-Gage Pressure Trace with Key Features of Trace Defined for Experiment 26 (Projectile Traveling at 263 m/s

3.3.1 Aluminum-Aluminum "Sandwich" Single Gage Target Experiment

Experiments 10 and 12 consisted of a target composed of a single gage epoxyed between two pieces of aluminum sheet metal with a mylar sheet encapsulating the gage leads. The system was triggered by a piezoelectric pin above the upstream aluminum surface. The resulting waveforms of these two experiments

can be seen in Figure 3.2 below.

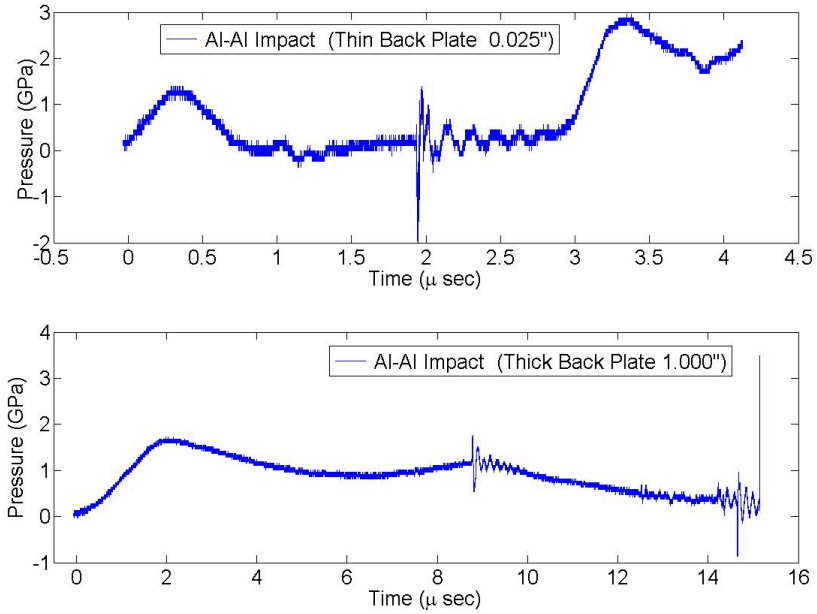

Figure 3.2: Aluminum Projectile Impacting Target consisting of Single Manganin Gage Embedded between Aluminum Sheet Metal

For projectile velocities of 259 m/s for the thin back plate and 253 m/s for the thick back plate the impedance matching technique was applied to calculate the peak pressure between each material of the target. Therefore, the impedance match will consist of the interaction between the aluminum projectile and aluminum front plate interface (1), the front plate and mylar sheet interface (2), and the mylar sheet and aluminum back plate interface (3) as depicted in Figure 3.3. Therefore the gage should read the Hugoniot pressure at state (3) of the impedance match.

The peak pressures acquired in these experiments utilizing both the Sandia and Rosenberg methods and the calculated Hugoniot pressure can be seen in Table 3.3. The Hugoniot Pressures were calculated by solving Equation 1.5 for the particle velocity at the intersection of the Hugoniot curves of interest. For the Aluminum components a Hugoniot slope of $S = 1.3507$ and bulk sound speed $C_0 = 5311.2$ and for the mylar sheet a Hugoniot slope of $S = 1.5954$ and bulk sound speed $C_0 = 2222.7$ were used in the calculations [33] [4].

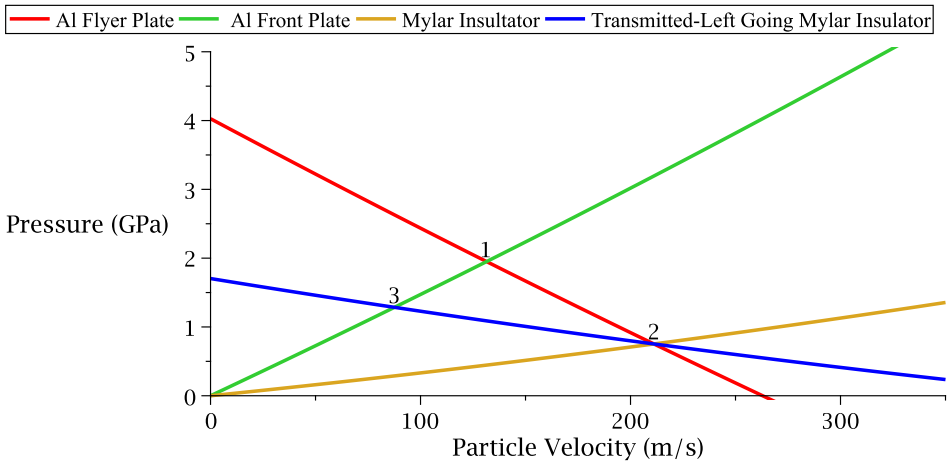

Figure 3.3: Impedance Match of Aluminum Projectile Impacting Target consisting of Aluminum and Mylar

Table 3.3: Velocities Achieved in Present Research

Experiment #	Experimental Pressure (GPa)	Theoretical Hugoniot Pressure State 1 Al-Al (GPa)	Theoretical Hugoniot Pressure State 3 Al-Mylar (GPa)
10	1.727±0.262	1.920	1.264
12	1.682±0.292	1.860	1.220

As seen in Table 3.3, the experimental data is roughly 10% below the Hugoniot pressure at the aluminum-aluminum interface, and 37% above the Hugoniot pressure at the mylar-aluminum interface. As mentioned in the introduction, Linde suggested the inclusion of mylar would reduce the peak stress by 10% or more when compared to experiments without the mylar shim [11]. Though experiments were not considered with the absence of the mylar shim, this phenomena is consistent with the current results if the Hugoniot pressure is equal to the experimental pressure without the mylar shim. However, these results indicate that the mylar has little effect on achieving the maximum pressure between the aluminum and aluminum interface. The impedance matching technique does not include parameters such as the strength of the metal and therefore represents a hydrodynamic treatment that will theoretically over predict the pressure in an interaction. In addition, these two experiments prove the "sandwich" target configuration can acquire pressures within 10% of the calculated values. No

additional experiments were performed with these specific targets as the goal was to simply acquire the stress signal and have the peak pressure be consistent with calculated values.

3.4 Impedance Matching Technique Applied to Two-Gage Target

The impedance matching technique was applied to experiments 22-26 using the same method as depicted in Figure 3.3. Only the front gage results were analyzed due to the inability to predict the back gage response without knowledge of the powder equation of state. The results from the impedance match are presented in Table 3.4 below:

Table 3.4: Comparison of Experimental Results and Impedance Matching Technique for Front Gage on the Two-Gage Target

Experiment #	Experimental Peak Pressure Sandia, State 1(GPa)	Experimental Peak Pressure Rosenberg, State 1 (GPa)	Hugoniot Pressure State 1 (GPa)	Hugoniot Pressure State 3-Mylar(GPa)
22	0.987±0.144	0.962	1.479	0.946
23	1.279±0.140	1.275	1.791	1.164
24	1.388±0.138	1.395	1.909	1.248
25	0.893±0.148	0.865	2.025	1.371
26	1.627±0.134	1.653	1.960	1.285

A similar result was encountered as experienced in the aluminum single-gage experiments. The experimental pressure was located between the calculated pressure at the aluminum-aluminum interface and the mylar-aluminum interface with the exception of experiment 25. The average deviation between the experimental pressure using the Sandia approximation and the aluminum Hugoniot pressure was 30.8% and 29% for the mylar Hugoniot pressure. However, the absolute value of the percent difference yielded values of 59.8% and 21.5%. However, the difference between the experimental pressure and aluminum Hugoniot pressure for experiment 26 was 17.8%. This value yields an agreement comparable to those in the single gage experiments. The encapsulating mylar sheet can contribute the decrease in peak pressure achieved by the stress measurement system. The decrease in pressure from the mylar shim is in agreement with the 10% or more proposed by Linde [11]. The inability to achieve uniform planarity of the target plate due to the

press fit and the necessity to hold vacuum on the target plate could have induced further flexure to the target plate causing a dampening effect to the incident wave as the target plate is forced to the planarity of the projectile.

The results in Table 3.4 indicate the Sandia and Rosenberg calculations differed by less than 3.3%. Based on the shims used in experiments 10 and 12 , the pressures recorded will resemble the upper tier of pressures capable for the Marquette SSGG in the recorded velocity range. For projectile velocities in the range 199 m/s to 270 m/s the calculated pressure will be in the range 1.48GPa to 2.05 GPa. Plotting the Sandia and Rosenberg curves together yields a maximum difference of roughly 4.6% over the expected pressure range. The largest percent difference arises at the discontinuity at 1.5GPa in the Rosenberg approximation. Therefore, for simplicity the Sandia approximation was used for the remainder of the calculations, as to avoid the piecewise function and work with a continuous function. More analysis needs to be conducted at pressures about 1.5GPa as there exists a discontinuity in the Rosenberg approximation at this pressure, the fourth-power law predicts limitations in the lower pressure regions, and Rosenberg's manganin gage hysteresis experiments for release waves (to be discussed further in Chapter 4) resulted in no observable hysteresis in pressures less than 1.45 GPa and small hysteresis appeared at 1.65GPa [31]. The conclusion that each method will produce comparable results when reduced further can be drawn from the fact that each approximation, Sandia or Rosenberg, results in an over-prediction for certain pressures.

3.5 Swegle-Grady Power Law Analysis on Two-Gage Powder Target

The successful acquisition of the two-gage waveforms allows for the structure of the waveform to be validated using the power law proposed by Swegle and Grady [24].

$$\sigma \propto \dot{\epsilon}^n \tag{3.1}$$

The waveform structure can be seen in the traces in Appendix B. Recall the gages are sandwiched between two pieces of aluminum sheet metal and therefore the

power law will determine the stress-strain rate relationship in the aluminum. Swegle and Grady concluded that fully consolidated materials, like aluminum bar stock, exhibit an n=4, fourth-order power law. As can be seen in Equation 3.1, solving the power law requires determining the peak pressure and strain rate of the waveform. The peak pressures are the maximum pressure (Hugoniot pressure) attained in the initial rise of the waveform. The strain rate was calculated using three different methods. For each method the rise time was calculated by determining that the waveform had a linear rise time between the 90% and 40% of the peak pressure. This linear relationship was then extrapolated to the maximum pressure and the zero pressure state. The rise time was then defined as the difference between the maximum pressure and the zero pressure, along the linear rise time line. The peak pressure and strain rate were then plotted in log-log space. A power-law fit was then applied to the data to obtain the power-law relationship described by Swegle and Grady.

In the first method, the theoretical density, $\rho_1 = \frac{1}{V_1}$, after compaction was calculated using the P-V relationship below.

$$P = \frac{C_0^2(V_0 - V_1)}{[V_0 - S(V_0 - V_1)]^2} \tag{3.2}$$

The strain rate in turn was calculated using the following equation for change in density.

$$\dot{\epsilon} = \frac{1 - \frac{\rho_0}{\rho_1}}{\Delta t} \tag{3.3}$$

The complete results from determining the values of the 90% and 40% of the peak pressure and their respective rise times can be seen in Table C.2 and Table C.3. The key results from applying the first method can be seen in Tables 3.5 and 3.6

Table 3.5: Experimental Data for Determining Fourth Power Law by Applying the Theoretical Method to Front Gage

Experiment #	Experimental Pressure (GPa)	Initial Density (g/cc)	Hugoniot Density (g/cc)	Strain Rate (s^{-1})
22	0.987±0.144	2.700	2.734	2.951E+04± 5.63E+02
23	1.279±0.140	2.700	2.746	3.650E+04±4.82E+02
24	1.388±0.138	2.700	2.747	4.234E+04±5.25E+02
25	0.893±0.148	2.700	2.731	1.878E+04±4.06E+02
26	1.627±0.134	2.700	2.755	6.571E+04±8.66E+02

Table 3.6: Experimental Data for Determining Fourth Power Law by Applying the Theoretical Method to Back Gage

Experiment #	Experimental Pressure (GPa)	Initial Density (m/s)	Hugoniot Density (m/s)	Strain Rate (s^{-1})
22	0.925±0.129	2.700	2.732	1.373E+04±2.69E+02
23	1.218±0.142	2.700	2.744	2.299E+04±3.06E+02
24	1.332±0.136	2.700	2.745	3.864E+04±5.02E+02
25	1.276±0.167	2.700	2.743	2.604E+04±3.36E+02
26	1.130±0.146	2.700	2.740	2.525E+04±4.15E+02

The second method assumed the experimentally observed pressure was most accurate. By utilizing the impedance matching technique the particle velocity was determined based on the experimentally determined pressure at each interface. The impedance matching technique can be seen in Figure 3.4 below, where state (2) represents the experimentally determined pressure for the front gage, and state (3) represents the pressure of the back gage.

The strain rate was then calculated using the following relationship between particle velocity, shock velocity, and rise time.

$$\dot{\epsilon} = \frac{\frac{U_p}{U_s}}{\Delta t} = \frac{\frac{U_p}{1.3507 * U_p + 5311.2}}{\Delta t} \tag{3.4}$$

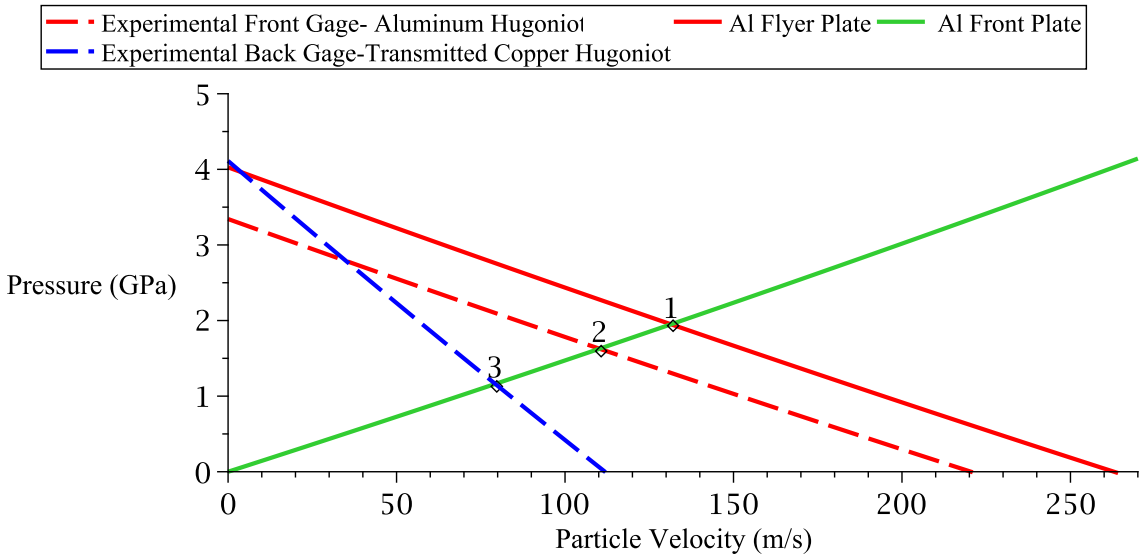

Figure 3.4: Impedance Match of Aluminum Projectile Impacting Target with Gage Pressure States Indicated

The shock velocity and particle velocity relationship for the aluminum sheet was determined based on data from the LASL Shock Hugoniot Data that represented particle velocities near those experienced in this research. The results for this pressure method can be seen in the two tables below.

Table 3.7: Experimental Data for Determining Fourth Power Law by Applying the Pressure Method to Front Gage

Experiment #	Experimental Pressure (GPa)	Particle Velocity (m/s)	Shock Velocity (m/s)	Strain Rate (s^{-1})
22	0.987±0.144	68	5402	2.984E+04± 3.31E+03
23	1.279±0.140	87	5429	3.537E+04±3.33E+03
24	1.388±0.138	94	5439	4.287E+04±3.68E+03
25	0.893±0.148	61	5394	1.878E+04±2.71E+03
26	1.627±0.134	40	5460	6.652E+04±4.70E+03

Table 3.8: Experimental Data for Determining Fourth Power Law by Applying the Pressure Method to Back Gage

Experiment #	Experimental Pressure (GPa)	Particle Velocity (m/s)	Shock Velocity (m/s)	Strain Rate (s^{-1})
22	0.925±0.129	63	5397	1.860E+04±1.71E+03
23	1.218±0.142	88	5430	3.096E+04±2.24E+03
24	1.332±0.136	90	5433	5.203E+04±3.54E+03
25	1.276±0.167	87	5394	3.531E+04±3.13E+03
26	1.130±0.146	79	5418	3.404E+04±2.84E+03

The third method assumed the projectile velocity was the most accurate method to acquire the particle velocity in the aluminum, rather than the experimentally observed pressure. By using the impedance matching technique discussed above, state (1) in Figure 3.4 represents the theoretical pressure state that the given projectile speed should reach. The particle velocity was then acquired from the x-axis and the strain rate was calculated using Equation 3.4 above. This method was not applied to the back gage, since the impedance matching technique cannot be utilized to determine the pressure and particle velocity at the back gage without knowledge of an equation of state for the powder.

Table 3.9: Experimental Data for Determining Fourth Power Law by Applying the Projectile Method to the Front Gage

Experiment #	Experimental Pressure (GPa)	Particle Velocity (m/s)	Shock Velocity (m/s)	Strain Rate (s^{-1})
22	0.987±0.144	100	5446	4.377E+04±9.36E+0
23	1.279±0.140	120	5474	4.841E+04±7.66E+0
24	1.388±0.138	128	5484	5.764E+04±1.04E+0
25	0.893±0.148	135	5494	4.078E+04±1.00E+0
26	1.627±0.134	131	5489	7.890E+04±2.15E+0

The results were calculated from each gage and method and plotted on a log-log plot. The pressures that were less than 1 GPa were not included as to prevent negative values incurring from taking the logarithm. A power law fit was then performed to each data group. The results can be seen graphically in the following three Figures:3.5, 3.6, 3.7

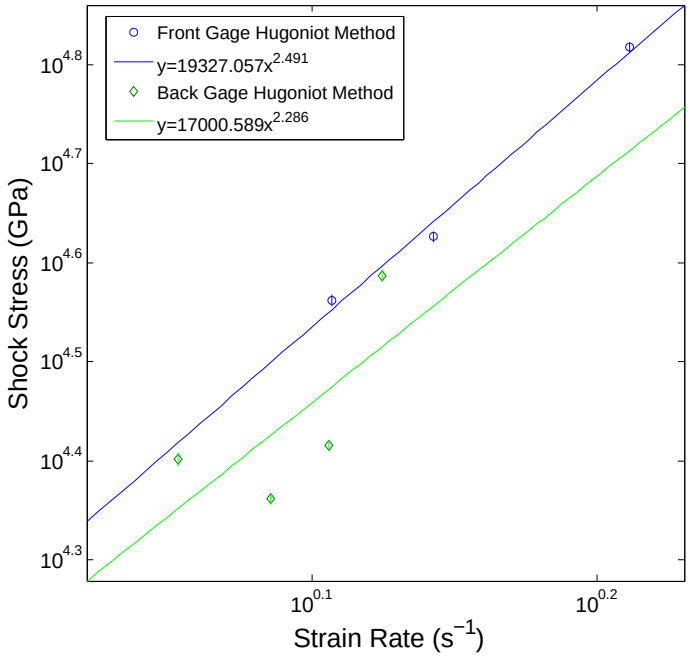

Figure 3.5: Power Law Plot: Pressure and Strain Rate for Theoretical Method

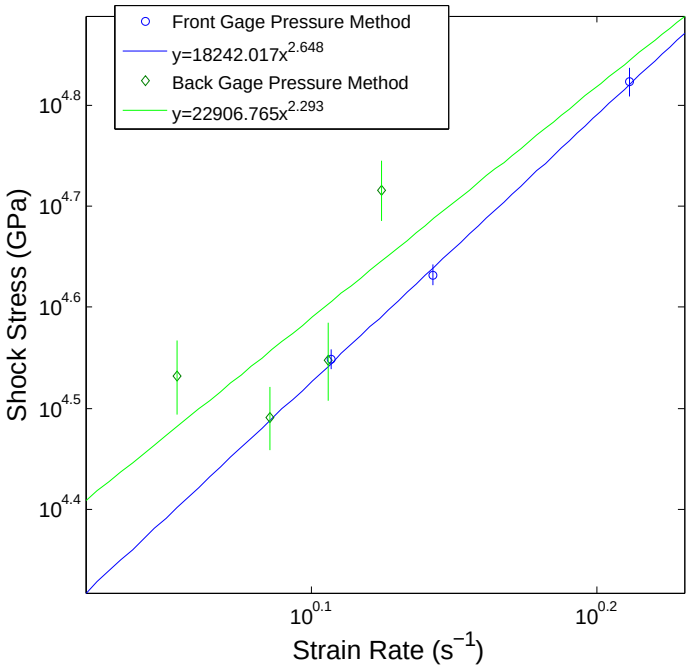

Figure 3.6: Power Law Plot: Pressure and Strain Rate for Pressure Method

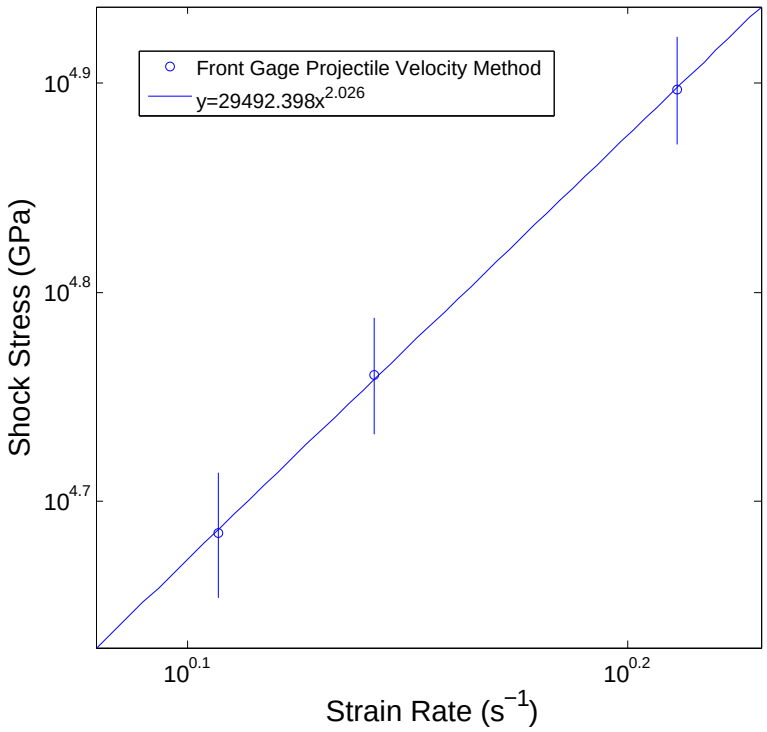

Figure 3.7: Power Law Plot: Pressure and Strain Rate for Projectile Velocity Method

The results for the front gage deviated minimally from the predicted power law fit, in comparison to the back gage. This result was expected due to the wave that encounters the back gage must interact with numerous materials, pass through a porous media, and be subject to numerous wave interactions. The previous description also describes the expected result of the front gage power-law being greater than the back gage power-law. The results for each trace was less than the fourth-power law fit expected and coincide more closely with the second-power law, n=2, of steady structured waves in laminated composites [24]. This result suggests that the mylar encapsulating sheet acts as a dampening or attenuating medium that lengthens the rise time. Grady-Swegle describe a polycarbonate and aluminum composite that experiences the second-power law, which describes the behavior observed in the present research. In addition, Grady also mentions that the rise time will increase as the thickness of the laminating layer (mylar) increases [34]. This increase in rise time will reduce the strain-rate and in turn lower the exponent of the power law. Therefore, if the flyer plate experiments were repeated with a laminating layer thicker than the 0.004" mylar shim used in the present research,

the exponent n, should approach n=2 from n=2.684 as the laminating layer thickness increases. The projectile velocity method for the front gage produced a power-law value less than the pressure method. This was expected since the shock velocity in the projectile measure exceeds that of the pressure measurement. The expectation also was that the Hugoniot method would produce an upper bound for the power-law based on the results of the impedance match of the two aluminum target experiments. This expectation failed due to the use of the experimentally observed pressure rather than the calculated pressure. The experimentally observed pressure provides more insight into the actual working of the system. One can conclude from the power-law analysis that the target system effectively represents the steady wave structure in accordance to the Grady-Swegle research and that the mylar sheet cannot be neglected due to its effect on the rise time and maximum state of the stress wave.

3.6 Wavelength Analysis

Lastly, the wavelength of the pressure wave must be analyzed to determine if the wave conforms to the thickness of the materials used. By knowing the expected wave speed in aluminum, the transit time in the aluminum cover plate can be determined and compared to the experimental results obtained here. In so doing, the experimental results can be validated against the accepted wave speed of aluminum. The target configuration used in the two gage experiments had an aluminum front-plate thickness of 0.032 inches, which should be equal to the wavelength of the pressure wave through the material. The wave period can be seen in Figure 3.1. The wavelength can be calculated by assuming the wave travels at a constant velocity, i.e. the shock velocity. Therefore, utilizing the equation below representing the period of the wavelength and the shock velocity through the front plate, the wavelength can be calculated using:

$$\lambda = U_s\tau = (1.3507 * U_p + 5311.2)\tau \tag{3.5}$$

where λ is the wavelength, U_s is the shock speed, U_p is the particle velocity, and τ is the period of waveform. The parameters for Hugoniot slope, S, and bulk

sound speed , C_0, were taken from the LASL Shock Hugoniot Data [4].

The shock velocity was calculated using the particle velocity at the flyer plate and front plate interface. The period of the shock wave was determined by analyzing the plot to determine a region where the maximum pressure occurs based on the first and last occurrences of the peak pressure. The results indicate that the average deviation from the expected wavelength is within 1.6% with a maximum deviation of 4.2%. The maximum deviation becomes 1.7% and average deviation of 0.96% when the uncertainty of the front plate thickness and experimental wavelength is taken into account. This is representative of two of the five experimental trials (24 and 26), since the uncertainty covers the deviation in the other experiments. This percent difference is acceptable when considering the digitization of the oscilloscope trace due to the sampling rate. Also, the accepted shock wave velocity is based on experimental data taken at different flyer-plate velocities then those experienced in the present research. This difference could also skew the data slightly. The results of the wavelength analysis are summarized in Table 3.10 below.

Table 3.10: Experimental Data for Determining Fourth Power Law by Applying the Projectile Method to the Front Gage

Experiment #	Front Plate Thickness (mm)	Period τ (μ sec)	Shock Velocity (m/s)	Experimental Wavelength (mm)
22	0.8128±0.0127	0.150	5446	0.8169±0.008
23	0.8128±0.0127	0.149	5474	0.8128±0.008
24	0.8128±0.0127	0.142	5484	0.7785±0.008
25	0.8128±0.0127	0.147	5494	0.8090±0.008
26	0.8128±0.0127	0.144	5489	0.7904±0.008

CHAPTER 4

Data Analysis

4.1 Development of Linear Equation of State $U_s - U_p$

The waveform traces from Figures D.1 to D.5 allow the equation of state for the heterogeneous powder to be determined. The equation of state will provide the means, as discussed previously, to relate the mass, momentum, and energy equations and determine relationships in other variable space such as $P - V$. The $U_s - U_p$ relationship will be represented by a linear fit to compare to tabulated values available in literature. A linear relationship will describe most materials not experiencing a phase transition [6]. In order to determine the $U_s - U_p$ relationship several methods will be employed to find the shock velocity, particle velocity, and release pressure. The Table C.4 depicts the target measurements and the key parameters acquired from the gage traces.

The release pressure is a result of the constant pressure wave through the aluminum front plates interacting with the lower impedance powder [5]. This interaction will result in lowering the incident pressure wave to some release pressure. The work of Rosenberg describes a hysteresis effect in the gage response during the transition from the shock state to a release state. The hysteresis of the gage is induced by strain-hardening resulting in an inability of the gage to behave elastically after being subject to a shock stress. Therefore, the measured change in resistance of the release state will represent an overestimate due to the hysteresis. Rosenberg states the hysteresis in the gage response upon full loading to be about 10% of the peak pressure state. Thus, the release pressure can be corrected using the formula below relating the peak pressure, experimental pressure, and release pressure:

$$P_r = \sum(P_E) - 0.1P_s \tag{4.1}$$

As stated previously, Rosenberg makes reference to no observable hysteresis

in peak pressure ranges from 0-1.45GPa, with minimal hysteresis at 1.65 GPa. The discussion in the previous chapter mentioned the discrepancy between the calculated peak pressure and the experimental peak pressure. The calculated peak pressure is greater than 1.45 GPa for all trials, while the experimental pressure is less than 1.65 GPa for all trials. Therefore, two series of peak pressures will be considered: one that takes into consideration the calculated value, where hysteresis would be valid, and the other where hysteresis would be invalid in the experimental data.

The particle velocity is calculated based on the impedance matching technique. The release pressure was defined as the pressure at the aluminum front plate and the powder interfaces. The experimental release pressure as defined in Figure 3.1 and as P_E in Equation 4.1 was determined by summing the steady state pressure region after the peak pressure. The initial estimates for the particle velocity were the bulk sound speed of the powder would be 400 m/s. This velocity was used to predict a place in time where the release pressure would occur by adding the time required to translate the aluminum back piston to the powder and the time required for the pressure wave at the impedance mismatch surface to reflect back to the gage. The time after the peak pressure where the release pressure began was determined to be 1.61 microseconds. The impedance match described can be seen in Figure 4.1 below.

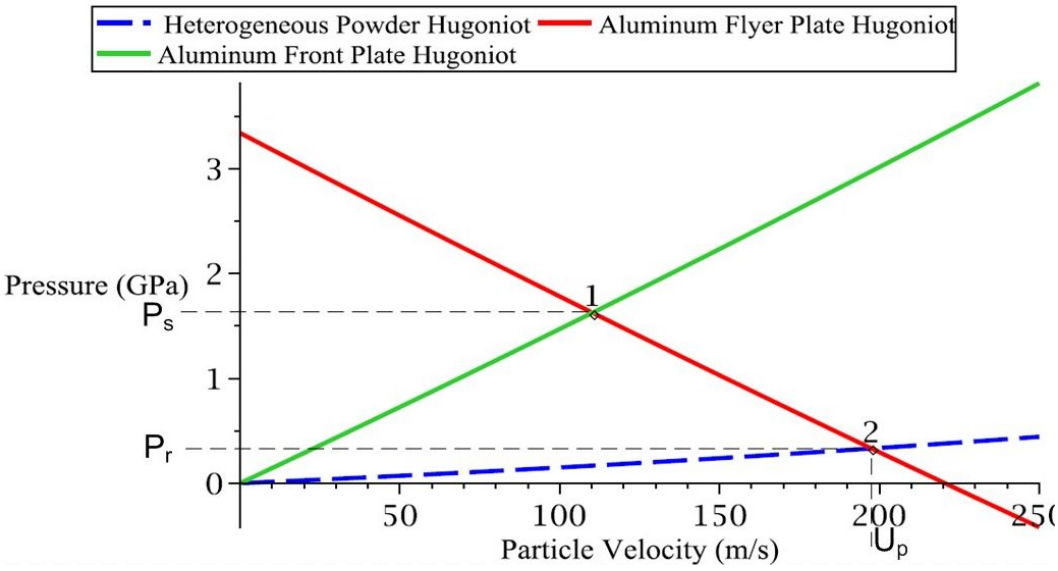

Figure 4.1: Impedance Match Depicting Powder and Aluminum Flyer Plate and Front Plate

State 2 represents the release pressure at the initial aluminum-powder interface induced by the flyer-plate experiment. The particle velocity is then determined by reading off the particle velocity on the x-axis for the given release pressure of state (2).

The shock velocity was calculated utilizing the definition of velocity coupled with the transit time between the two gage waveforms and the material of the target constituents used. The definition of velocity required taking the powder thickness divided by the transit time. The transit time was taken as the time difference between the front gage reaching 50% of the peak value and the back gage reaching 20% of the back gage peak value. This relationship can be seen with the formula below:

$$U_s = \frac{t_p}{\Delta t} \tag{4.2}$$

Many references utilized a 50% peak value indicator for the wave arrival time for both gages. However in some situations, the shallow, slow rise-time from the powder densification makes it difficult to justify the 50% peak value as an indicator of the time of arrival of the wave. Thus, a first detectable rise in the gage is used as an indicator for the time of arrival. As a compromise, the 20% rise time appeared to be the best back gage indicator based on the data plots. This 20% location was above the noise from the compacting material and therefore on the shallow rising pressure wave plateau. The transit time was then adjusted for the gage being embedded in between materials outside the powder location. The resulting equation for the shock speed is presented in equation 4.3

$$U_s = \frac{t_p}{\Delta t_{gage} - \Delta t_{aluminum} - \Delta t_{mylar} - \Delta t_{copper}} \tag{4.3}$$

The first method investigated was based on the Hugoniot pressure, Impedance match, while neglecting the effect of the mylar insulator. Therefore, the particle velocity was determined by applying the method depicted in Figure 4.1. The shock velocity on the other hand was determined by dividing the powder thickness by the transit time. The transit time based on the assumptions requires deducting the time required for the pressure wave at the incident aluminum-aluminum

interface to be transmitted to the powder, and the transit time of the transmitted pressure wave to pass through the copper shim before reaching the back gage. The transmitted pressure wave through the copper shim was determined using an impedance matching technique at the peak pressure of the back gage. The equation of state for the copper shim was determined based on the low particle velocity experiments tabulated in the LASL Shock Hugoniot Data [4]. The equation then utilized to determine the shock speed of this method is depicted below.

$$U_s = \frac{t_p}{\Delta t_{gage} - \Delta t_{aluminum} - \Delta t_{copper}} \tag{4.4}$$

$$U_s = \frac{t_p}{\Delta t_{gage} - \frac{t_1}{1.3507 * U_1 + 5311.2} - \frac{t_3}{1.5042 * U_3 + 3950.6}} \tag{4.5}$$

The particle velocities are those depicted in Figure 4.2 with State 1 representing the Al-Al interface and State 3 representing the powder-copper interface. The resulting values for U_s and U_p are presented in Table 4.1 below and the a graphical representation in Figure 4.3 with the linear equation of state superimposed.

Table 4.1: Shock and Particle Velocities Acquired Using Hugoniot Pressure Data and Neglecting Presence of Mylar

	Raw Data		Gage Hysteresis	
Experiment #	Particle Velocity (m/s)	Shock Velocity (m/s)	Particle Velocity (m/s)	Shock Velocity (m/s)
22	186±25	522±16	193±25	522±16
23	208±22	641±18	217±22	641±18
24	226±23	738±21	236±23	738±21
25	237±22	561±16	243±22	561±16
26	239±23	537±15	251±23	537±15

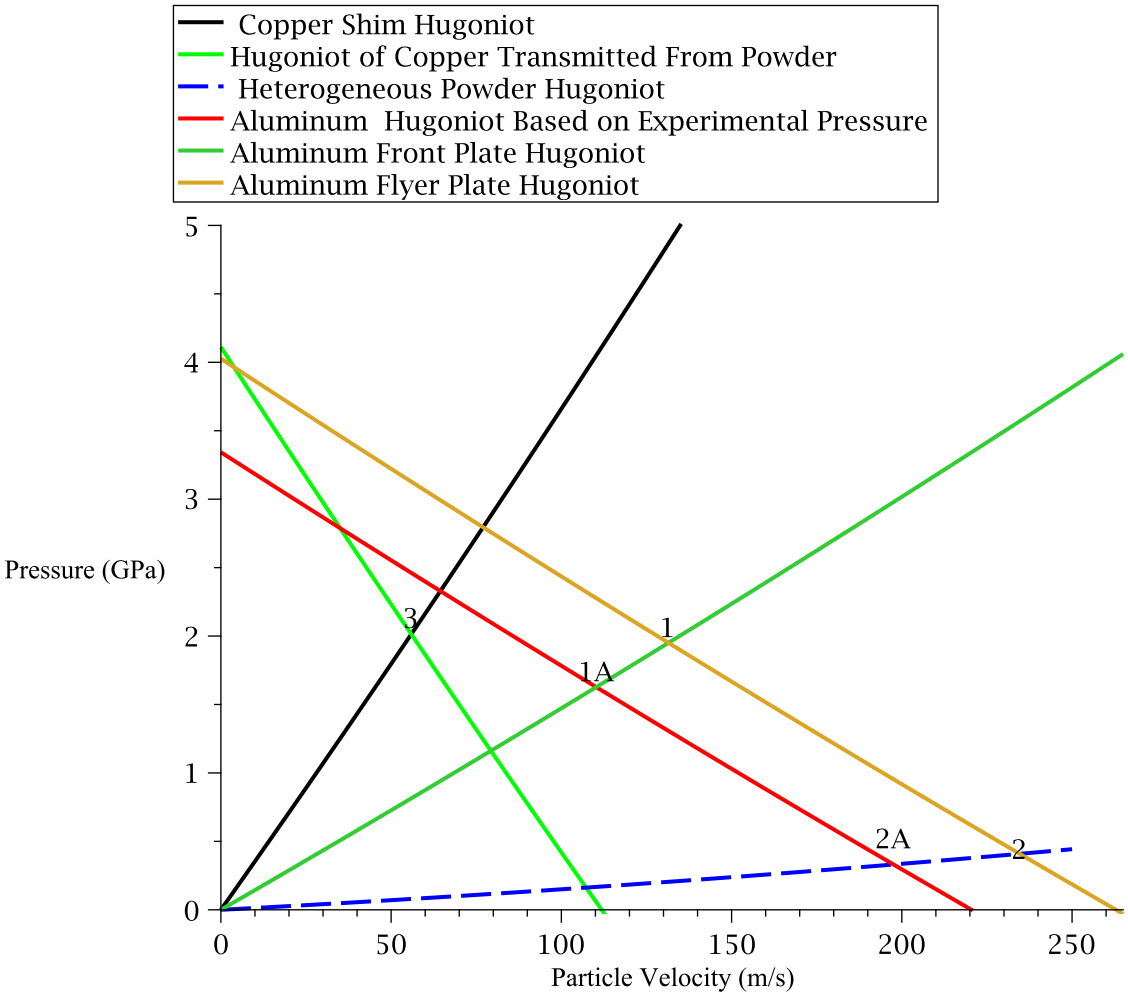

Figure 4.2: Impedance Match Depicting Powder and Aluminum Flyer Plate and Front Plate for Calculated and Experimental Pressures

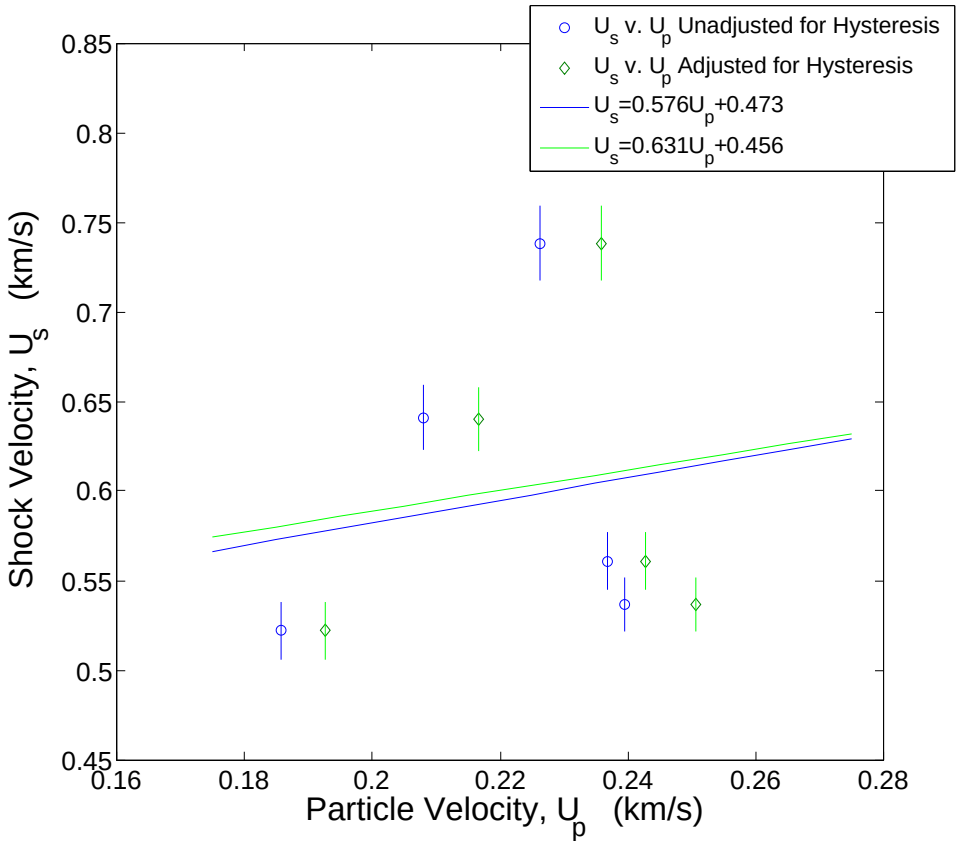

Figure 4.3: $U_s - U_p$ Plot for Data Based on Hugoniot Pressure and Neglecting Presence of Mylar

The second method assumed the experimental pressure was correct and the effect of the mylar sheet was negligible. This new interaction can be seen in the impedance match Figure 4.2 below . The particle velocity is then calculated based on the release pressure depicted by state (2A). The shock speed is calculated using Equation 4.5 with an adjustment made for the particle velocity through the aluminum sheet.

The results from the second method are displayed in the Table 4.2 and Figure 4.4 below:

Table 4.2: Shock and Particle Velocities Acquired Using Experimental Pressure Data and Neglecting Presence of Mylar

	Raw Data		Gage Hysteresis	
Experiment #	Particle Velocity (m/s)	Shock Velocity (m/s)	Particle Velocity (m/s)	Shock Velocity (m/s)
22	121	522	128	522
23	142	641	150	641
24	159	739	168	739
25	88	561	94	561
26	197	537	208	537

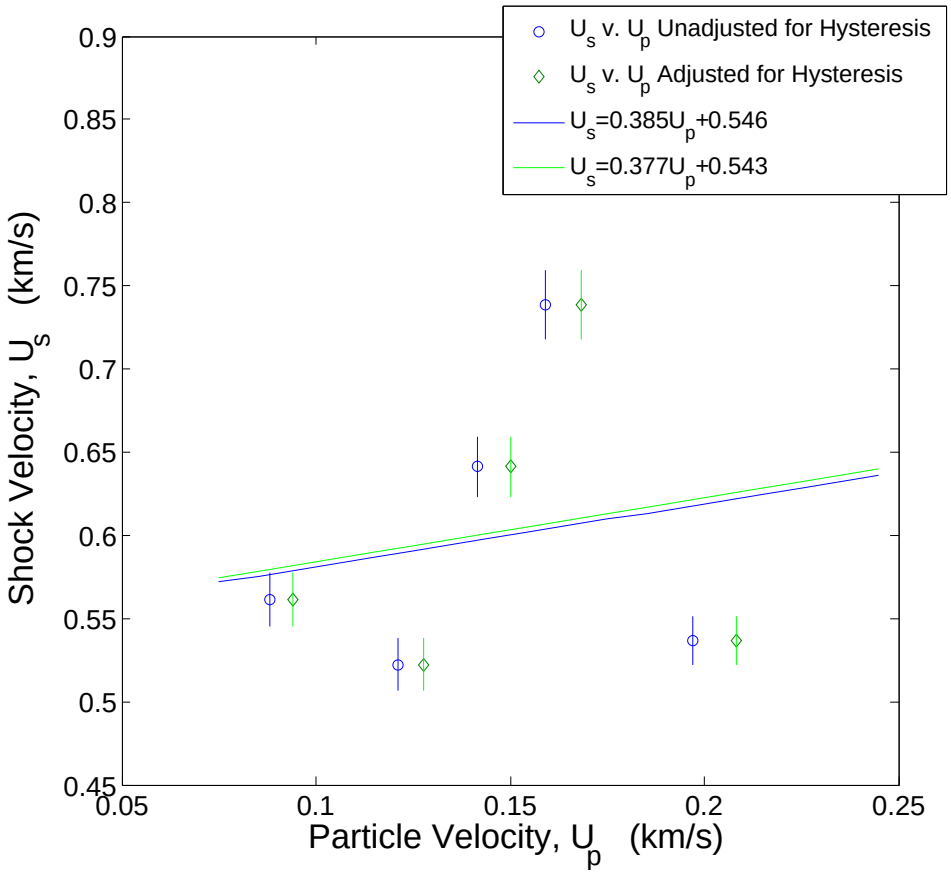

Figure 4.4: $U_s - U_p$ Plot for Data Based on Experimental Pressure and Neglecting Presence of Mylar

The third method will take into account the effects of the mylar sheet, with the particle velocity determined from the Hugoniot due to the projectile velocity. Therefore, the impedance match technique will be described by Figures 4.5 and 4.6 below. The particle velocity is then described as the interaction at state (4).

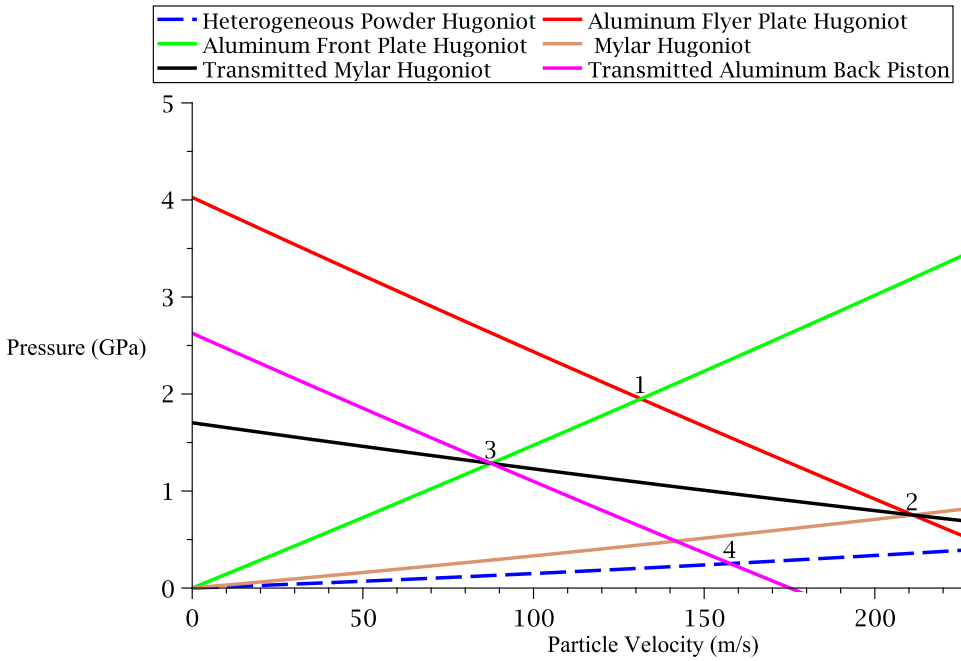

Figure 4.5: Impedance Matching Technique for Front Gage with Inclusion of Mylar

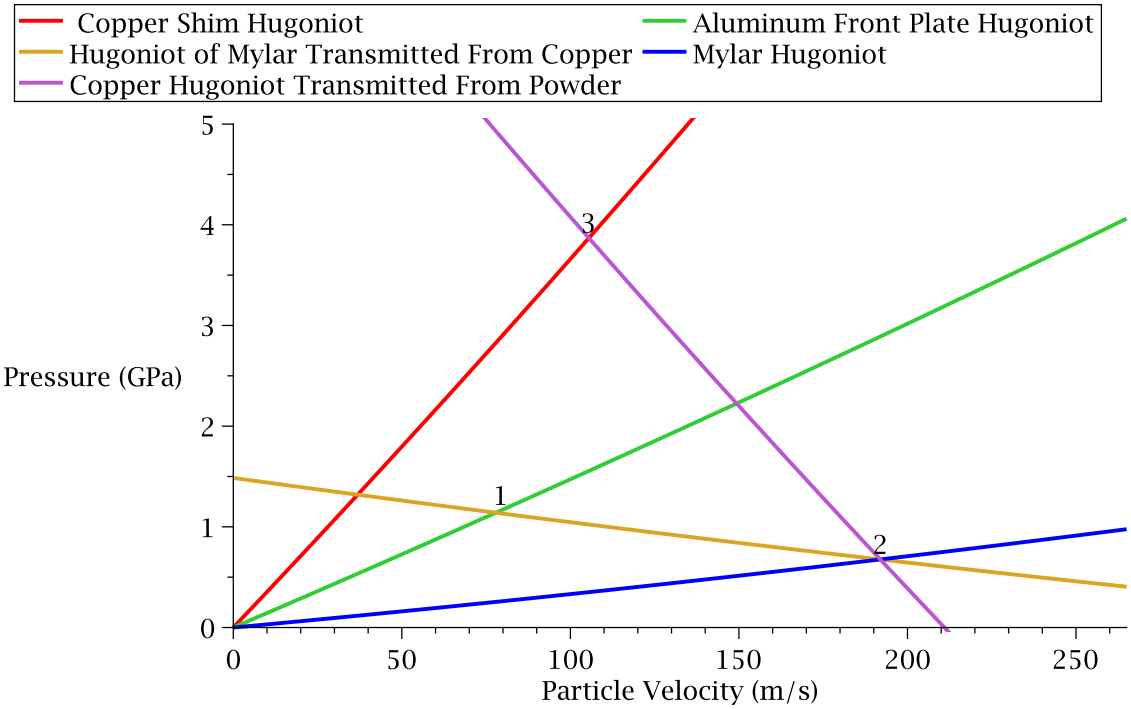

Figure 4.6: Impedance Matching Technique for Back Gage with Inclusion of Mylar

The inclusion of the mylar will also now effect the transit time through the back gage. The new equation for the shock speed through the powder will be represented by the equation below based on Equation 4.3:

$$U_s = \frac{t_p}{\Delta t_{gage} - \frac{t_1}{1.3507 * U_1 + 5311.2} - \frac{t_3}{1.5042 * U_3 + 3950.6} - \frac{t_4}{1.5954 * U_4 + 2222.7}} \tag{4.6}$$

The equation of state for the mylar sheet was determined based on the tabulated data from flyer plate experiments conducted by Boeing [33]. The particle velocity of the materials through the copper shim and mylar sheet were determined by reflecting the Hugoniot curves from the aluminum mylar interface to the copper powder interface. This interaction can be seen in Figure 4.5 above with the aluminum-mylar interface represented by (1) and the copper-powder interface represented by (3). The application of this method yielded the tabulated and graphical results displayed below:

Table 4.3: Shock and Particle Velocities Acquired Using Hugoniot Pressure Data and Including Presence of Mylar

	Raw Data		Gage Hysteresis	
Experiment #	Particle Velocity (m/s)	Shock Velocity (m/s)	Particle Velocity (m/s)	Shock Velocity (m/s)
22	105	529	112	529
23	114	650	123	650
24	127	750	137	750
25	133	567	139	568
26	138	543	150	543

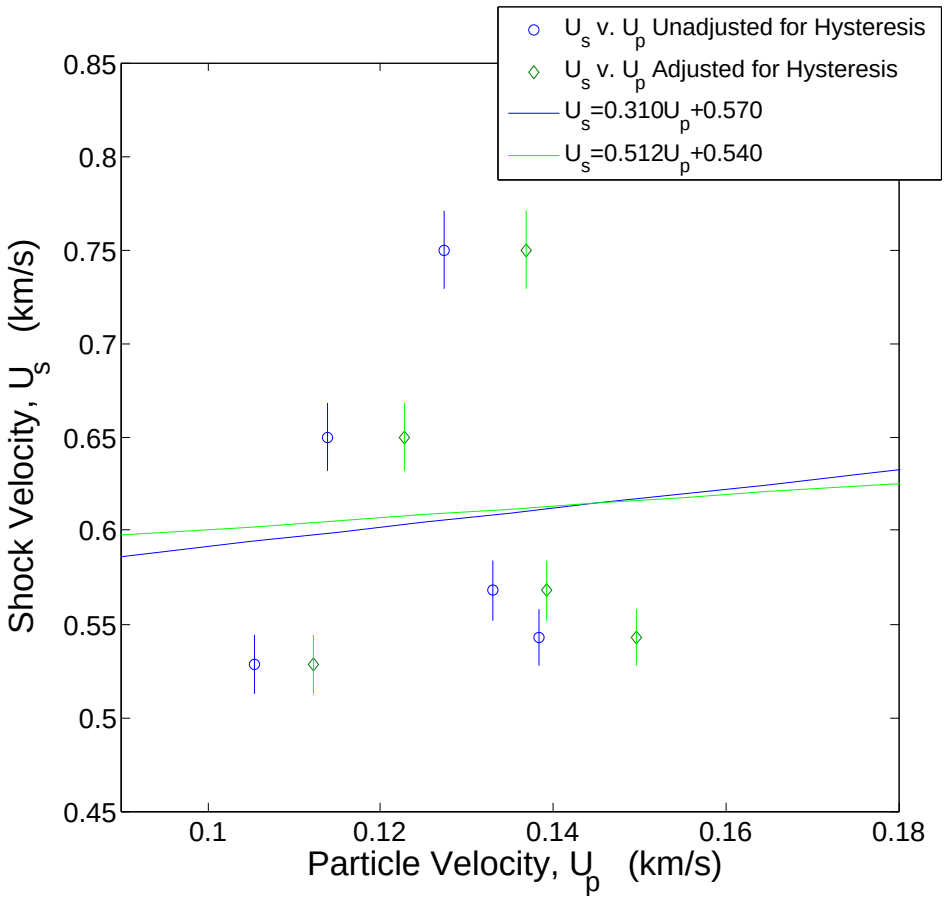

Figure 4.7: $U_s - U_p$ Plot for Data Based on Hugoniot Pressure and Inclusion of Mylar

The final method considered utilized a similar technique, but based on the particle velocity of the experimental peak pressure rather than the calculated Hugoniot pressure. This method will result in the same particle velocity of the powder calculated in Method 2 (see Figure 4.2 State (1)). However, the shock velocity in Equation 4.5 needs to be adjusted to account for this new particle velocity through the aluminum sheet do to the experimental pressure. The particle velocities determined for copper and Mylar from the Impedance Match in Method 3 are still accurate for this method. The results of this method are depicted in Table 4.4 and Figure 4.8 below:

Table 4.4: Shock and Particle Velocities Acquired Using Experimental Pressure Data and Including Presence of Mylar

	Raw Data		Gage Hysteresis	
Experiment #	Particle Velocity (m/s)	Shock Velocity (m/s)	Particle Velocity (m/s)	Shock Velocity (m/s)
22	121	529	128	529
23	142	650	150	650
24	159	750	168	750
25	88	568	94	568
26	197	543	208	543

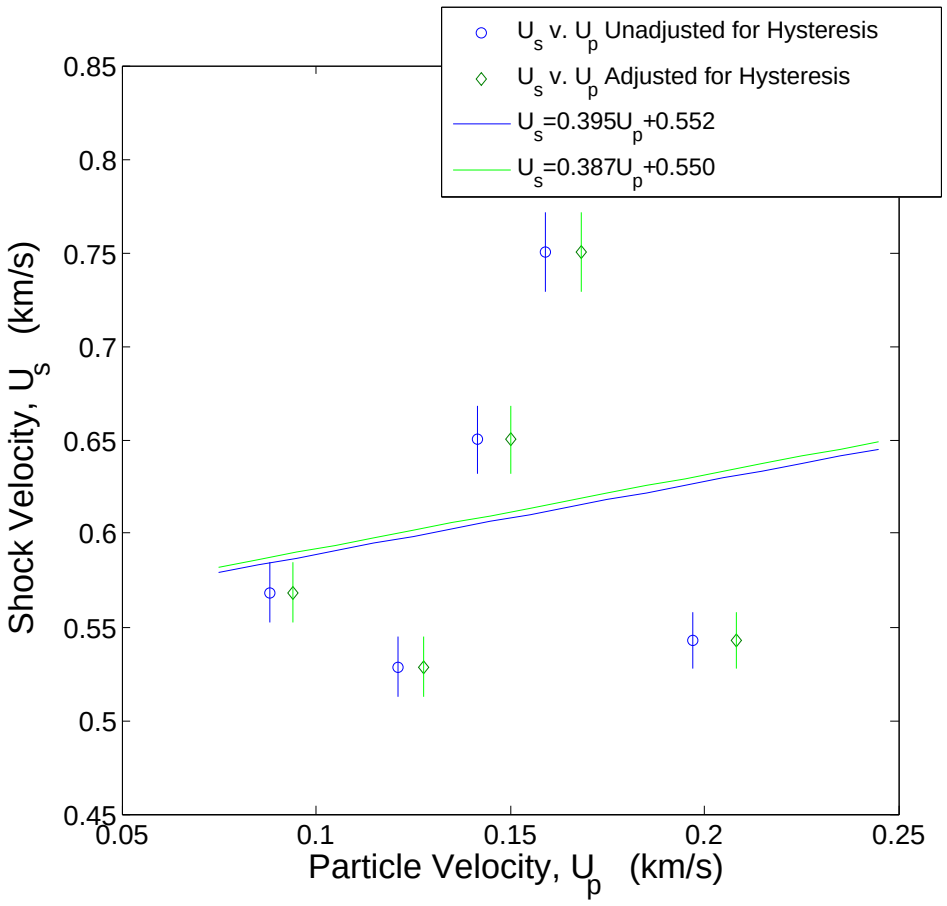

Figure 4.8: $U_s - U_p$ Plot for Data Based on Experimental Pressure and Inclusion of Mylar

From the plots and table above it is clear that regardless whether the hysteresis release pressure was considered or not, the $U_s - U_p$ equations of state based on the calculations and experiential pressure were very similar. Comparing the equations of state based on the experimental pressure for the mylar and no

mylar considerations for both release pressure regimes yielded a percent difference in Hugoniot slope of 2.1% and bulk sound speed of 0.4%. These results were expected as the particle velocities for the two methods were identical and the inclusion of mylar scaled the shock velocities slightly greater. The Hugoniot calculations of mylar yielded a difference of 65% for the Hugoniot slope and 5.1% for the bulk sound speed over the pressure regimes, and the calculations neglecting mylar yielded a Hugoniot slope and bulk sound speed percent difference or 9.6% and 3.9% respectively. In addition, from Table 4.5, the uncertainty boundaries in each Hugoniot slope calculation, include the slopes of the remaining calculation methods. Therefore, the calculation methods of the Hugoniot slopes do not have a significant statistical impact inside of the uncertainty of the slopes. The uncertainties in the bulk sound speed, C_0, however, are significant. The uncertainties in C_0 for the Experimental Methods (1 and 3) were much smaller than the uncertainties for C_0 in the Hugoniot Pressure Calculation Methods. Thus, Methods 1 and 3 can be considered more statistically accurate, which is encouraging since the results are based entirely on experimental data. The inclusion of points on the $U_s - U_p$ plot at higher particle velocities could improve the uncertainties in S and C_0 since the current research contained a wide range of shock velocities over a narrow range of particle velocities. The conclusion can be drawn, neglecting the mylar calculations, that there is little effect due to hysteresis on the equation of state. Also, the inclusion of mylar in determining the particle velocity from the Hugoniot calculations has proved troublesome as in the previous sections in correlation with the experimental results. The inclusion of Mylar in the equation of state determination will be considered in the computer simulations as providing an upper bound based on the resulting highest bulk sound speed.

Table 4.5: Hugoniot Slope and Bulk Sound Speed for Each U_s, U_p Calculation Method

Method	Hugoniot Slope (S)	Bulk Sound Speed, C_0 (km/s)	
1	Hysteresis	0.5757 ± 2.2902	0.473 ± 0.504
	No Hysteresis	0.6313 ± 2.1930	0.456 ± 0.501
2	Hysteresis	0.3851 ± 1.2545	0.546 ± 0.183
	No Hysteresis	0.3773 ± 1.1940	0.543 ± 0.185
3	Hysteresis	0.3098 ± 3.8937	0.570 ± 0.484
	No Hysteresis	0.5117 ± 3.6149	0.540 ± 0.480
4	Hysteresis	0.3949 ± 1.2869	0.552 ± 0.188
	No Hysteresis	0.3869 ± 1.2248	0.550 ± 0.189

The determined equations of state were also compared to the tabulated values for the constituents available in open literature. Table 4.6 below lists the Hugoniot slopes and bulk sound speeds for the various constituents in the heterogeneous mixture with similar densities to those used in the present mixture. Figure 4.9 depicts the tabulated data and equations of state for all the constituents on a single plot.

Table 4.6: Hugoniot Slope and Bulk Sound Speed for Heterogeneous Mixture and Tabulated Data for Constituents

Material	Hugoniot Slope (S)	Bulk Sound Speed, C_0 (km/s)
Heterogeneous Mixture 2.7564 g/cc	0.5757	0.47519
Unpressed Copper Powder 3.007 g/cc	1.4083	0.33077
Pressed Copper Powder 6.49 g/cc	2.1142	0.37905
Pressed Graphite 1.626 g/cc	1.9838	0.93459
Silica Powder 0.77 g/cc	0.40439	1.071
Sintered Iron Powder 3.368 g/cc	1.4814	0.36753

For simplicity, the Hugoniot calculation with no mylar will be used as the baseline for equation of state for the present research. Copper, which has the highest density of any constituent and represents the largest fraction of powder in the heterogeneous mixture, will therefore dominate the developed equation of state. The copper used in the flyer plate experiments and the mixture as a whole had a density less than the copper data in Figure 4.9. The less dense mixture would increase the amount of energy required in compaction to full density resulting in shock speeds less than those at higher densities. This intuition is represented in the comparison as the less dense heterogeneous mixture data is well below that of the denser copper and iron components. Based on the slopes of the equations of state the inclusion of silica could have contributed to the heterogeneous mixture having a Hugoniot slope less than those of iron, copper, and graphite.

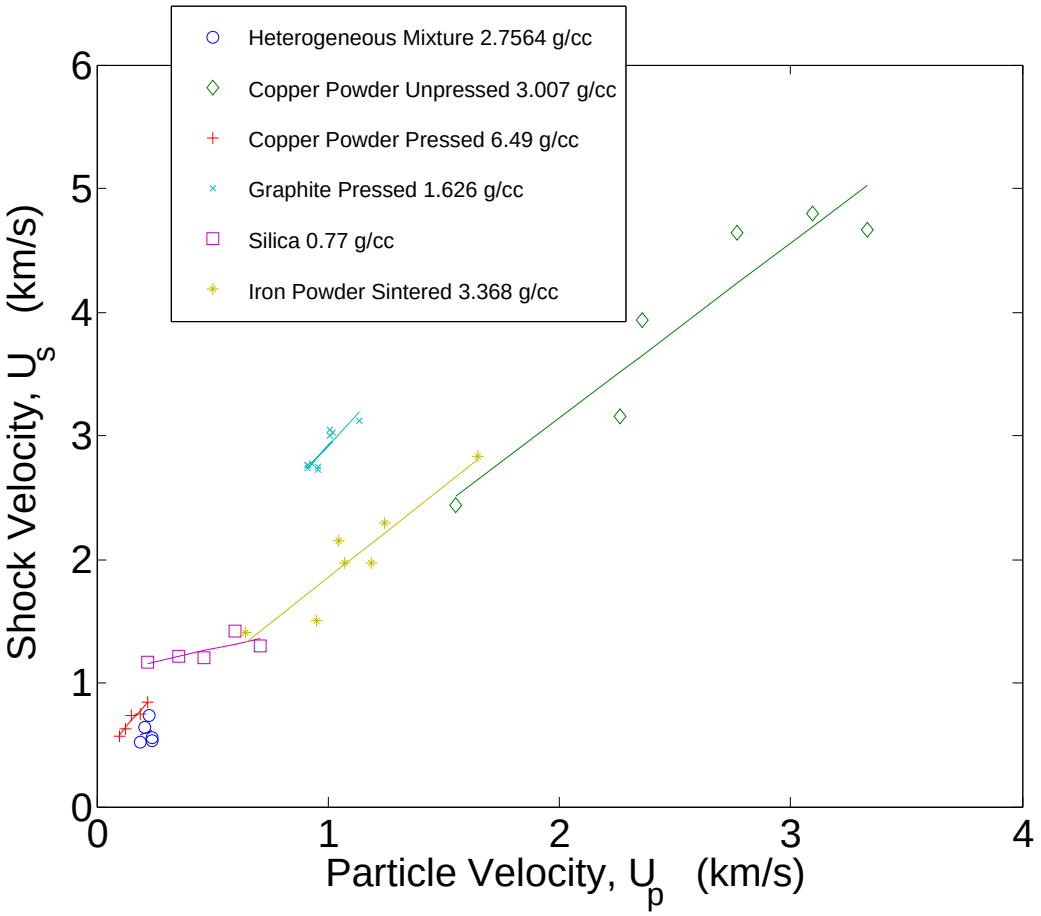

Figure 4.9: Experimental Data and Hugoniot Slope for Heterogeneous Mixture and Data of Various Constituents Available in Research of Boade, Borg, and LASL [3] [4] [5]

As stated earlier, this figure also contributes to uncertainties in the present research. The inability of the gas gun used in the flyer plate experiments to produce a vast range of projectile velocities only provides data with particle velocities in a small region of the tabulated $U_s - U_p$ space. Data available at a higher projectile velocity would provide a more accurate method in both determining the equation of state and in comparing the results to data readily available in literature on the compaction of porous copper, graphite, silica, and iron [3] [4] [5]. This would yield more insight into the behavior of the powder over greater pressure ranges.

4.2 One-Dimensional Bulk Simulations

The implementation of computer simulations provides an additional means to analyze the effectiveness or accuracy of the experimental apparatus and gain additional insight into the phenomena experienced. Ideally the computer simulation should closely follow the experimental pressure- time waveform; matching the key features of the waveform such as peak pressure, release pressure, and transit time. The KO computer program utilized to run the simulations employs partial differential equations and the corresponding finite difference equations [35]. In addition, the program is implemented in time-dependent and one-dimension space. The program requires several fundamental equations to describe the shock wave interactions including [35]:

1. Equation of Motion
2. Conservation of Mass
3. First Law of Thermodynamics
4. Velocity Strains
5. Stress Deviators
6. Pressure Equation of State
7. Total Stresses
8. Artificial Viscosity

9. Von Mises Yield Condition

In order to properly solve the fundamental equations numerous properties of the experiment must be identified in the computer programs input file. The properties of the Flyer Plate and Target included in the input file are listed below:

1. Material Thicknesses
2. Material Density
3. Projectile Velocity
4. Hugoniot Linear Equation of State (S and C_0)
5. λ Grüneisen Parameter
6. Dynamic Yield Strength
7. Shear Strength
8. C_V Constant Volume Specific Heat

The values for the constituents other than the heterogeneous powder were taken from tabulated literature data. However, values for the heterogeneous powder such as Dynamic Yield Strength and Shear Strength could not be readily determined. Therefore, a mixture theory was applied to the heterogenous powder taking into account the values obtained in literature for the individual constituents (i.e. copper, iron, graphite, etc.). The mixture theory was presented in *Transport Phenomena* for estimating thermal conductivities of a mixture but will be applied in various forms to develop strength values for the heterogeneous powder [36]. The equations for the mixture theory are displayed below:

$$\frac{k_{eff}}{k_0} = \frac{\sum_{i=0}^{N} \alpha_i (\frac{k_i}{k_0}) \phi_i}{\sum_{i=0}^{N} \alpha_i \phi_i} \tag{4.7}$$

$$\alpha_i = \frac{1}{3} \sum_{i=0}^{N} [1 + (\frac{k_i}{k_0} - 1) g_j]^{-1} \tag{4.8}$$

where $g_j = \frac{1}{3}$ when the granular materials are assumed to be spheres, ϕ is the volume fraction and k is the parameter of interest.

Once the input file has been formatted correctly the KO computer program was ran with Digital Visual Fortran 6.0. The computer program produces a data file complete with numerous variables including pressure, particle, velocity, and density with respect to time. The data file was uploaded into Matlab. A program was developed in Matlab to develop figures in varying variable space. For the purpose of the current research the Matlab program was manipulated to output a plot of pressure vs. time to compare with the experimental waveforms. The location tracer was set at the location of the gages embedded in the target. The simulation will allow the gage location to move with the target due to the induced impact velocity of the projectile. Therefore, the gage response does not require a time correction, as would be the case if the gage was fixed to one eulerian position. The resulting waveforms for Experiment 26 can be seen in Figures 4.10 and 4.11 with the remaining simulations for Experiments 22-25 included in the Appendix D.

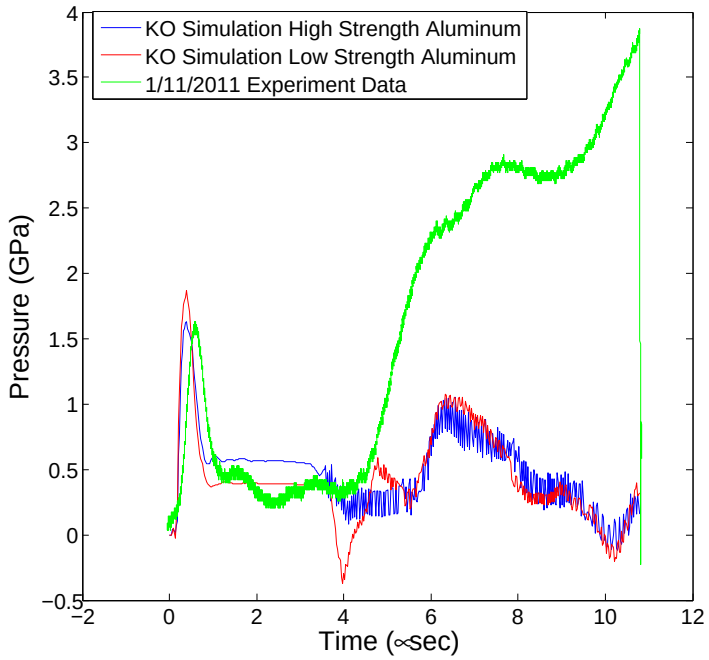

Figure 4.10: Front Gage Simulation and Experiment Pressure Trace for Experiment 25 over 14 Microseconds Shot Velocity 271 m/s and Powder Density 2.747 g/cc.

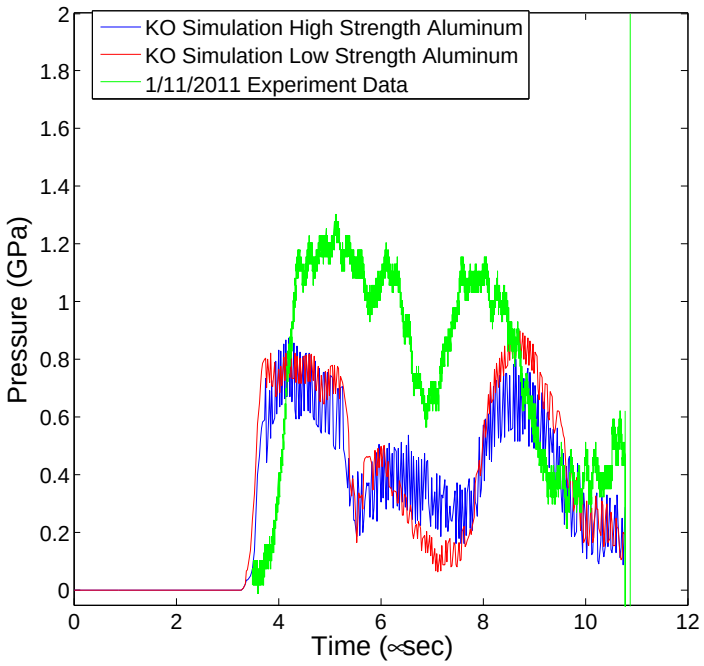

Figure 4.11: Back Gage Simulation and Experiment Pressure Trace for Experiment 26 over 14 Microseconds Shot Velocity 263 m/s and Powder Density 2.724 g/cc.

In the previous section, eight potential linear equations of state were developed from experimental data and various target assumptions. The computer simulations were run for the upper and lower bounds of the bulk sound speed (C_0) for the equation of states. This method will entail that the remaining equations of state would result in simulation that are located between the two bounded simulations. The two equations of state that form the upper and lower bound are listed below, where Equation 4.9 was developed using Method 1 with hysteresis considered and Equation 4.10 was derived from Method 3 with no hysteresis considered:

$$U_s = 0.631U_P + 0.456 \tag{4.9}$$

$$U_s = 0.310U_P + 0.570 \tag{4.10}$$

In addition, the simulations were run considering varying strengths of the materials used in the flyer plate experiments. The simulations were also performed with and without the inclusion of the Mylar encapsulating sheet. Experiment 26 was used as the baseline for the computer simulations. Therefore, once the

simulations were deemed appropriate for Experiment 26, the same parameters were applied to Experiments 22-25. The goal of the simulation analysis was to provide the parameters required to produce the simulation that most closely resembled that of the experimental data.

The simulations proved to qualitatively map the waveform of the experimental pressure-time traces. The input file that achieved the simulations depicted in Figures 4.10 and 4.11 and Appendix D can be seen in Table C.5 in Appendix C. The inclusion of the Mylar encapsulating shim, Higher Strength Aluminum Front Plates, and the equation of state in Equation 4.9 best represented the experimental data. The plot in Figures 4.10 and 4.11 depict the differences between the High and Low Strength Aluminum. The low strength aluminum more closely maps the release pressure while the high strength aluminum more closely maps the peak pressure. In addition, at 4 microseconds the low strength aluminum goes into tension, which is not observed in the experimental data or high strength aluminum simulation. The powder cannot support a tensile wave The high strength aluminum was chosen to represent the data as a whole due to the ability to capture the peak pressure and the overshoot in the release pressure. Based on the equation of state in Figure 4.3 the data point for Experiment 26 is below the linear fit. Therefore, the equation of state will over predict waveform behavior for the particular experimental conditions. All the simulations except Experiment 24 under predict the transit time between the two gages. This underestimation of transit time is consistent with the KO simulations on silica powder [25]. The overestimation observed in Experiment 24 was expected due to the location of the data point in Figure 4.3. The experimental shock velocity for Experiment 24 was over 150 m/s greater than the equation of state for the given particle velocity. Also, all the simulations underestimated the peak pressure of the back gage by roughly 33%. This underestimation is expected based on similarities between the KO simulation and the impedance matching technique, including the hydrostatic pressure. The impedance matching technique describing the entire experiment interaction severely under-predicts the back gage pressure by 87 %. The KO simulation and impedance matching technique do not take into account the granular material interactions or the shock waves that propagate in radial directions. Based

on the voids present in the granular mixture, the shock wave will form an irregular or (non-steady) front. The locations in the granular mixture where several particles are in contact will transmit the shock wave at higher shock velocities and pressures than the locations that contain a significant number of voids (Energy is absorbed in void collapse). In addition, there exists impedance mismatches as the shock wave transmits through the various constituents in the mixture. Therefore, for multiple experiments at a similar sample porosity, the pressure observed by the gage will differ based on the particular path the shock wave travels (though material or through void). On the contrary, the KO simulation is mainly hydrodynamic (considers material strength) but does not consider the porous behavior of the material and therefore would produce an over estimate of the actual pressure through the material. A more robust simulation (Two- Dimensional) would be required to resolve the back gage pressure. The KO simulation also does not predict the initial rise time of the front gage waveform. The simulation rise time occurs roughly 0.25 microseconds prior to the experimental data. The method used to create the experimental targets is most likely cause for the discrepancy. Due to the inability to press the front plate flush resulted in 0.015 inch deviation on the front plate surface. This deviation could result in 0.1 microsecond differential in rise time but may also act as a damper for the incoming shock wave as the front plate is pressed to zero deflection. This dampening effect will further increase the time required for the incident shock wave to reach the front gage.

The simulations were also able to correctly predict the shape of the experimental waveform. At approximately 6.5 microseconds all the simulations displayed a second compression state which is apparent on the experimental traces. However, the second compression state in the simulation data is roughly 2GPa below the experimental data. In addition the simulation of the back gage correctly predicts the peaks and valleys apparent in the experimental data. These peaks and valleys are seen at the 6, 7, and 8 microsecond locations on the experimental data. The simulation data however displays a delay in the location of these peaks and valleys by roughly 1 microsecond. The front gage simulations resulted in a release pressure that occurred roughly 0.6 microseconds before the experimental release pressure. This could be a result of the uncertainties discussed in the front plate

creation in the previous paragraph in addition to the gage in the experimental data. The simulation did not include the presence of the gage. The effect the presence of the gage has in determining the results will be discussed later in this paper.

4.3 Static Compaction Results

The static compaction of the heterogeneous powder was able to subject the material to pressures up to 0.038 GPa and final density of 4.6 g/cc. The elastic loading of the powder followed a similar path to that described by Herrmann [15] The static compaction plot in pressure-density space for the powder exposed to several load control ranges can be seen in Figure 4.12 below. The estimated average rate of compaction was 0.008 in/min at 4 Kip load control and 0.015 in/min at 20 Kip load control. The difference in compaction rates is due to the duration of the applied load remaining constant.

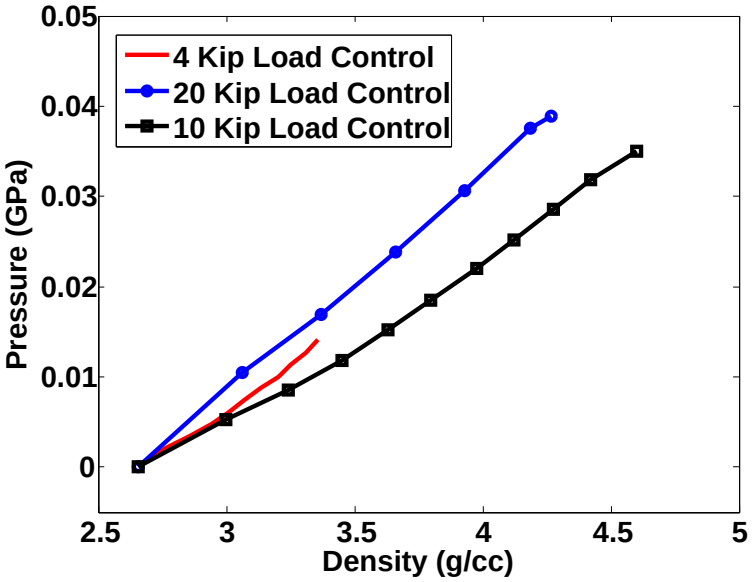

Figure 4.12: Static Compaction of Heterogeneous Powder over Varying Load Control Ranges

The deviation in the loading paths is likely a result of different constituent volume percentages. All off the samples statically compacted formed a "puck" shaped compact when removed from the container. However, it was noticed under the static loading that the graphite particles had diffused toward the outside of the container. When the "puck" was removed from the container the graphite area did

not remain in contact with the predominately copper interior and broke apart.

4.4 P-α Model Development and Discussion

The P-α model was applied to the experimental data in the present research and tabulated research to develop a relationship for the heterogeneous powder in pressure-density space under dynamic loading. The pressure in the elastic regime was assumed to be zero. This implies that under any stress the heterogeneous powder will plastically deform. The Third-order formulation for the P-α model was applied to the data. This eliminated the need to acquire the slope of the curve at the point where the elastic and plastic regions meet. The P-α model will thus adhere to the relationship in Equation 4.11 below with the coefficients defined in Table 4.7.

$$\alpha = \alpha_0 + \alpha_1 P + \alpha_2 P^2 \tag{4.11}$$

Table 4.7: Coefficients for Third Order P-α Model

Coefficient Variable	Coefficient Formula
α_0	α_p
α_1	$\frac{-2(\alpha_p-1)}{P_s}$
α_2	$\frac{(\alpha_p-1)}{P_s^2}$
α_3	0

The pressure P_s, when the powder becomes compacted to solid density, was determined utilizing the mixture theory based on data available in literature. The research of Linde analyzed the compaction of porous iron and graphite while the research of Boade included the compaction of porous copper [11] [12] [9]. The research of Borg presented the compaction of the porous silica [5]. There was no tabulated data in literature pertaining to the compaction of porous Tin and MoS_2 which was relatively unimportant due to their 3.1% by volume contribution to the mixture. P_s was determined from the literature mentioned above by acquiring the data point in $P - \rho$ space that was closest to the solid Hugoniot. It is important to

note that none of the research discussed above occurred at the same apparent density as each of the constituents in the present research. Therefore, the $P-\alpha$ model was determined twice for the unadjusted data from literature and also for the P_s adjusted based on the porosity difference between the literature and the present research. The value of α_p is the ratio of the density as a solid compact to that of the uncompacted powder. The results of the $P-\alpha$ Model can bee seen in Figure 4.13

The equation of state developed in Section 3.1 was also plotted in pressure-density space and compared to the theoretically determined solid curve. The lower bound equation of state obtained from using the Hugoniot Pressure with no mylar or hysteresis was used to represent the powder mixture. The solid curve was developed using the mixture theory discussed in the previous chapter. The resulting curves can be seen in Figure 4.13.

The $P-\alpha$ model was also developed for porous copper based on the density of the heterogeneous mixture. P_s was taken to be the dynamic yield strength (σ_{yd}) from the flat-end projectile tests conducted by Whiffen [37]. The dynamic yield stress of copper was determined to be 0.2 GPa. This model will provide a lower bound of the heterogeneous mixture based on the constituent with the greatest volume fraction.

The results depicted in the plot were determined based on the experimental pressure and the final state density was derived from the strain. The strain is a function of the experimentally determined shock speed and particle velocity, which can easily be related to density. The strain equation was developed based on the Conservation of Mass Equation.

$$\epsilon = \frac{U_p}{U_s} = 1 - \frac{\rho_0}{\rho} \tag{4.12}$$

The plots in Figure 4.13 indicate that the experimental data straddle the porous Hugoniot and the $P-\alpha$ Model adjusted for porosity. As expected with all the experiments subjecting the powder to pressures over 0.2 GPa, the copper had yielded and was above the $P-\alpha$ for copper only. Also, the $P-\alpha$ Model based on the unadjusted P_s was an over prediction due to the higher density constituents used. The experimental data also seems to be at the same relative pressure of those

indicated by the work of Linde for porous iron. The work of Whiffen indicated that the dynamic yield strength of iron was roughly 0.675 GPa. Therefore, one can assume that the iron powder in the experiments of the present research did not yield. Higher pressure experiments will be required to see if the experimental data continues to follow the porous Hugoniot and $P - \alpha$ Model adjusted for porosity. Also, further experiments will indicate if the experimental data behaves such that the iron particles begin yielding at pressures above 0.675 GPa. This would be represented by large increases in pressure as the heterogenous powder density approaches that of the solid Hugoniot.

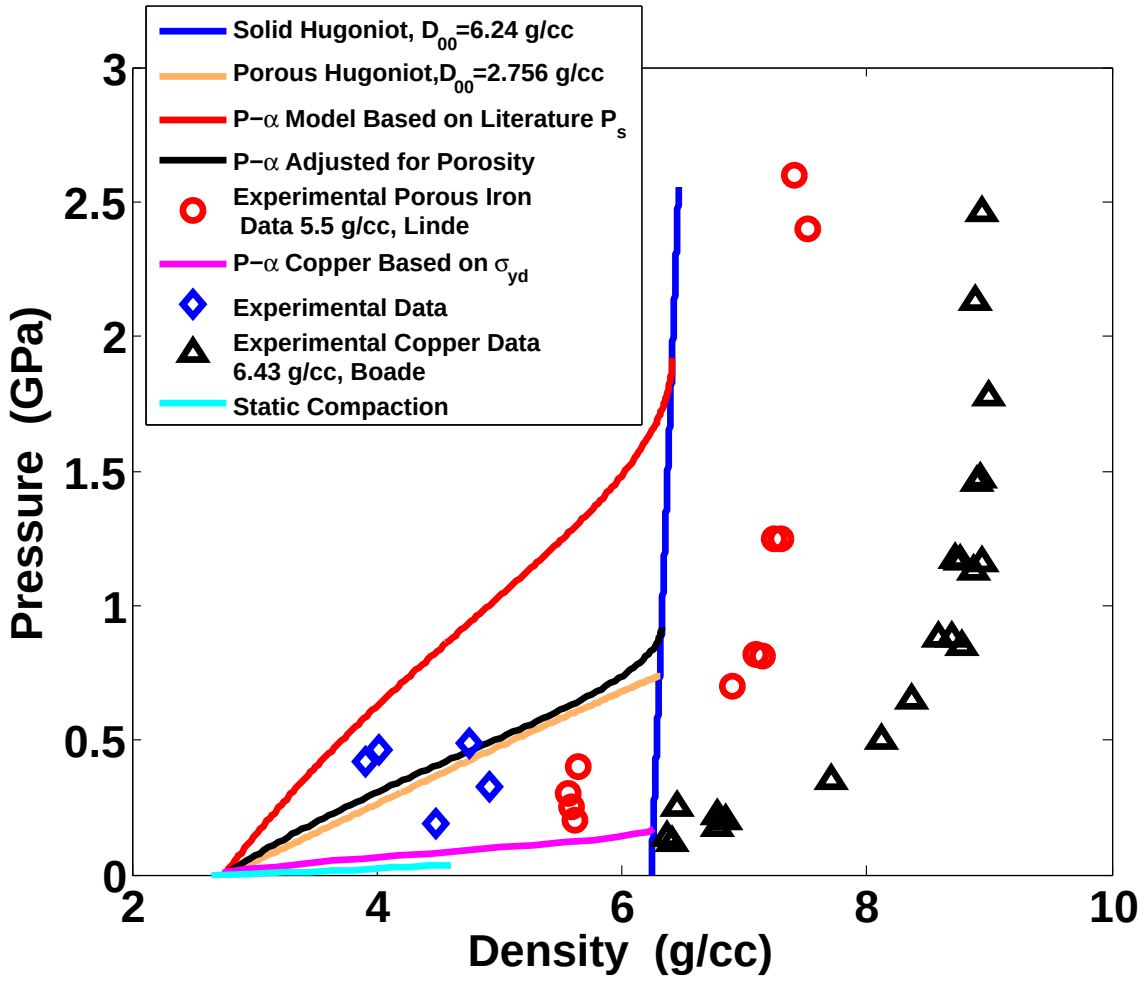

Figure 4.13: $P - \alpha$ Model in Comparison to the Theoretical Hugoniot for the Heterogeneous Powder, the Predicted Solid Hugoniot, and Experimental Data-Static and Dynamic

4.5 Morphological Comparison of Statically and Dynamically Compacted Samples

The morphology of the statically pressed and sintered powder compacts will be compared to the dynamically compacted samples produced in the present research. The samples will be compared using optical microscopy and scanning electron microscopy, in addition to determining the porosity of the compacts. As has been seen in the previous discussion, the dynamically compacted samples were subjected to pressures of 0.203 to 0.501 GPa for durations of 2.6 to 3.6 microseconds. The pressed and sintered compacts experienced pressures of 0.275GPa at temperatures of 900C (1652F) for 1.5 hours [38]. The images will yield valuable qualitative insight into how the individual constituents arrange themselves and bond when subjected to the varying load conditions. For simplicity, due to the number of images, the images can be seen in Appendix I. The visible constituents have been labeled in Figures 4.15,4.16, and 4.19.

The optical images in Figures 4.15-4.18 indicate the bulk orientation of the powder constituents upon loading. From the images it is clear that regardless of the loading mechanism, the graphite particles have coalesced and have aligned in a linear manner perpendicular to the direction of the shock wave or press. As seen in Figure 4.14, the graphite particles initially have no preferred alignment. In addition, the silica particles have an apparent lateral fracture in both the statically pressed and sintered and dynamically loaded samples. This lateral fracture is in the direction of the shockwave or press. Also, the copper constituents have yielded and have surrounded the nearby constituents. This is apparent in all the images especially with the copper's enclosing of the iron and silica particles. The yielding is expected since the pressures subjected to the powders was greater than the 0.213GPa dynamic yield strength of copper. However, based on the porosity of the dynamically compacted samples the yielding or flow of the copper particles was not great enough to fill the present voids and further pressure would be required to fill the remaining voids and yield the stronger constituents, especially iron.

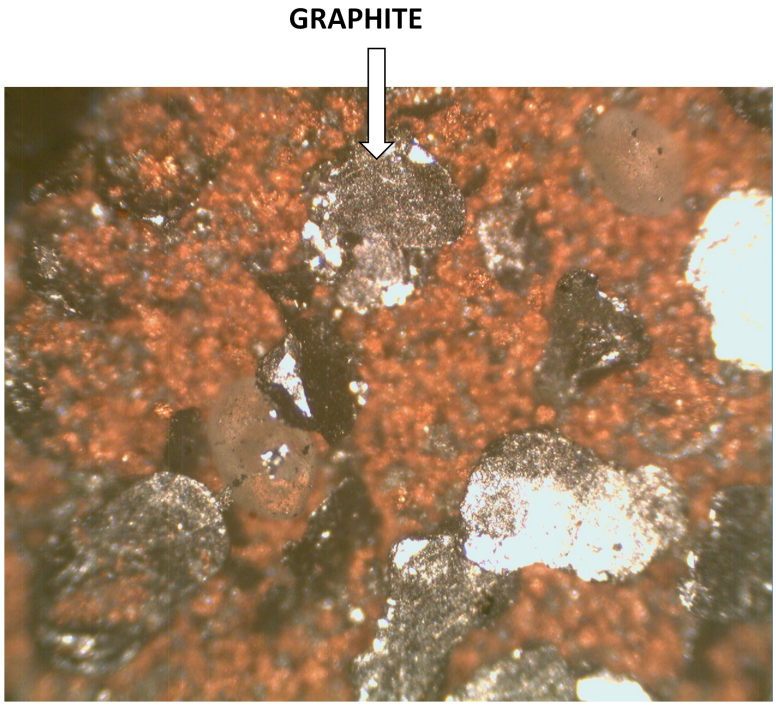

Figure 4.14: Optical Image of Powder Before Compaction.

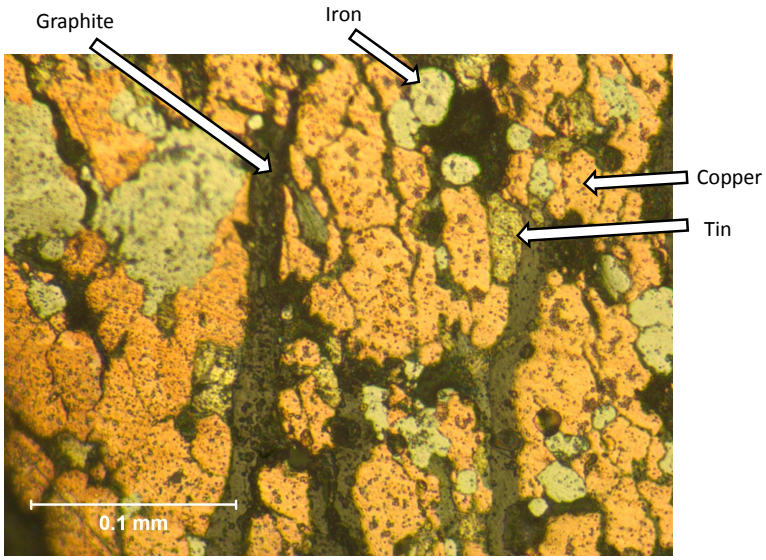

Figure 4.15: Dynamically Compacted Powder at 0.203GPa. Optical Image Corresponding to Working Area in SEM Image. Direction of Shock Wave is From the Left to Right

Figure 4.16: Optical Image of Dynamically Compacted Powder at 0.203GPa. Direction of Shock Wave is From the Left to Right

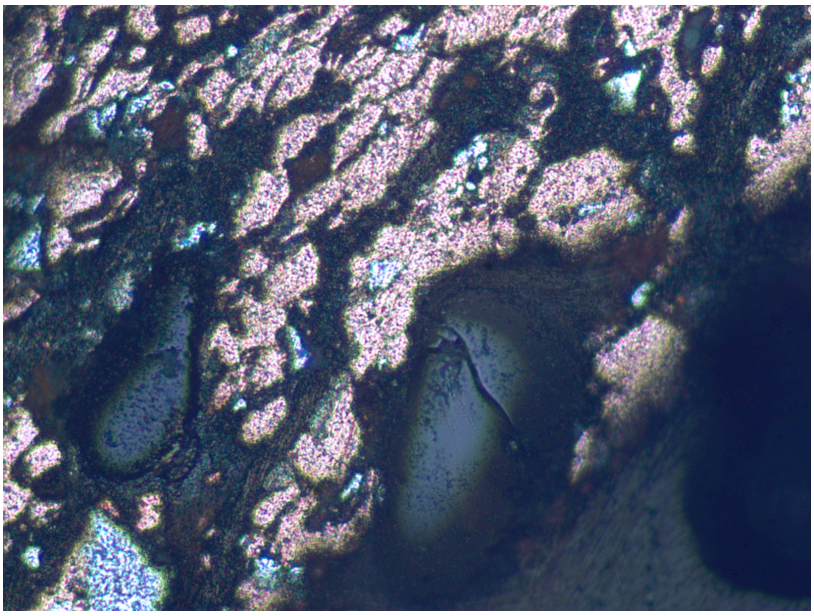

Figure 4.17: Optical Image of Dynamically Compacted Powder at 0.501GPa. Direction of Shock Wave is From the Left to Right

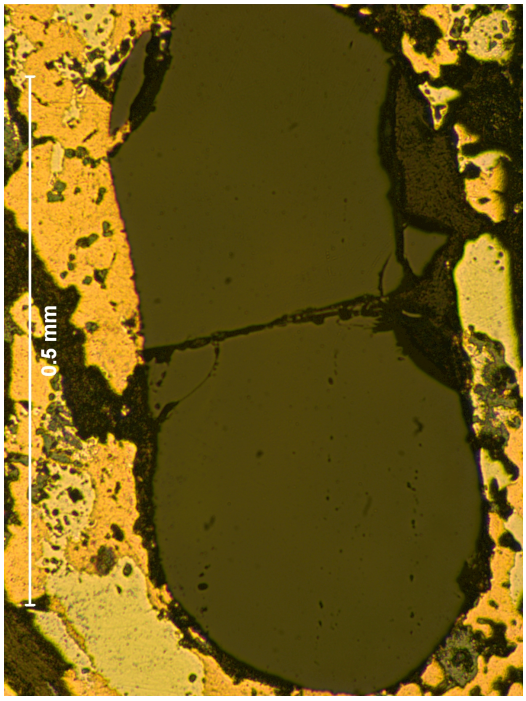

Figure 4.18: Optical Image of Statically Pressed and Sintered Powder Compact Magnification 100X. (Pressed from the Left to Right)

The SEM Images clearly indicate the dynamically compacted samples have not achieved high density states. In Figure 4.19, the copper particles appear to have at one time been compacted to the adjacent particles, as seen by the "puzzle" type morphology. The higher pressure dynamically compacted samples appear to have a similar "puzzle" behavior with much less of a void space present. This may indicate that the release waves in the low pressure dynamic loading cause the particles to be displaced significantly relative to the other pressure regimes. A higher-level computer simulation would need to be employed to determine if release wave was present in the powder. There is no evidence of the "puzzle" behavior in the pressed and sintered samples, as the copper appears to be uniformly bonded to the adjacent copper particles and enclosing the adjacent iron particles. It also appears in comparing the pressed and sintered SEM image to the image in Figure 4.20 that localized sintering has occurred. The experiment in Figure 4.20 was different to the others in that the recovered samples were much larger, as much as five times the thickness, due to the absence of stress gages. This may indicate that the powder experienced high temperatures for a longer duration.

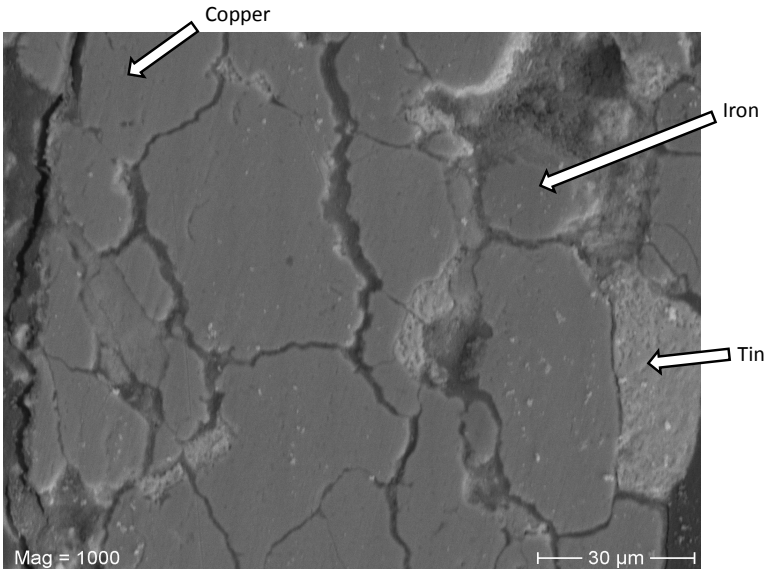

Figure 4.19: Scanning Electron Microscope Image of Dynamically Compacted Powder at 0.203GPa. Direction of Shock Wave is From the Left to Right

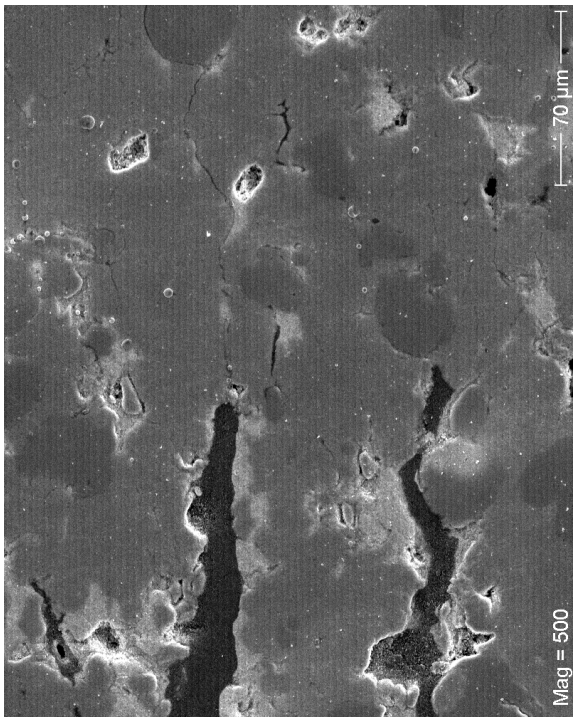

Figure 4.20: Scanning Electron Microscope Image of Dynamically Compacted Powder at 0.34-0.433GPa. Direction of Shock Wave is From the Left to Right

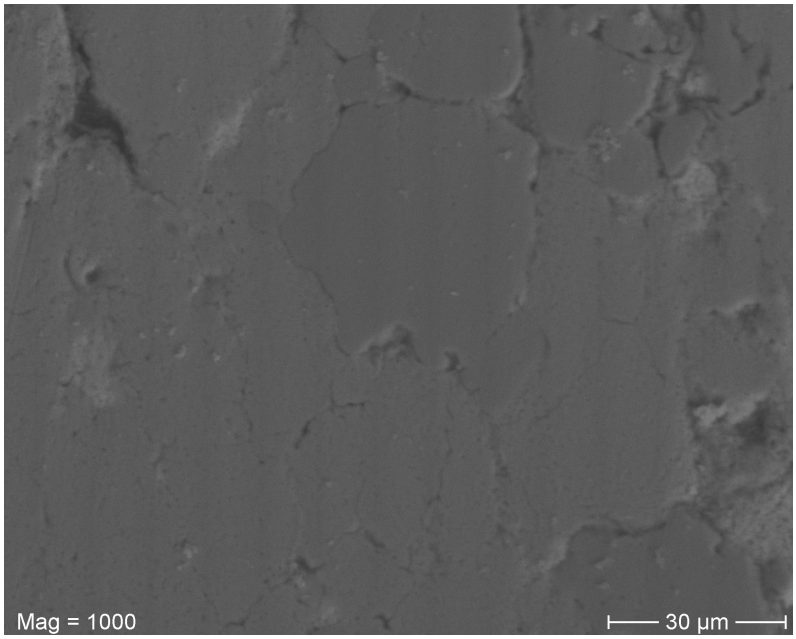

Figure 4.21: Scanning Electron Microscope Image of Dynamically Compacted Powder at 0.501GPa. Direction of Shock Wave is From the Left to Right

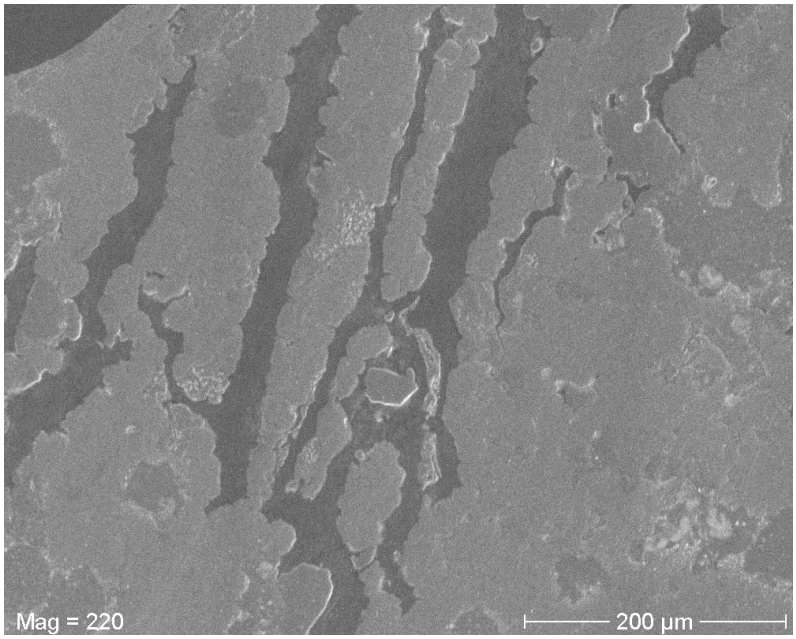

Figure 4.22: Scanning Electron Microscope Image of Statically Pressed and Sintered Powder Compact (Pressed from the Left to Right)

The porosity of the samples was determined using the *SimplePCI* imaging software. A total of six images at magnification of 100X were taken of the dynamically compacted samples over the radial direction of the cross section for the samples compacted at 0.203 GPa and 0.501 GPa. Ten images at 100X were taken of the pressed and sintered powder compacts due to the large size of the samples. The images were manipulated using the *GNU Image Manipulation Program (GIMP).* The color of the pores was selected and turned black, while the remaining constituents were set to white for detection in *SimplePCI.* The result of this procedure can be seen in Figure H.2. The images were then imported into *SimplePCI* and prepared to measure the area of the image, region of interest (ROI) or pores, and the resulting pore fraction. The "separate" feature was used to filter the image so the majority of the pores were clearly defined. The resulting porosity of each compaction method can be seen in Figures 4.23-4.25 below. The results can be seen in tabular form in Table 4.8.

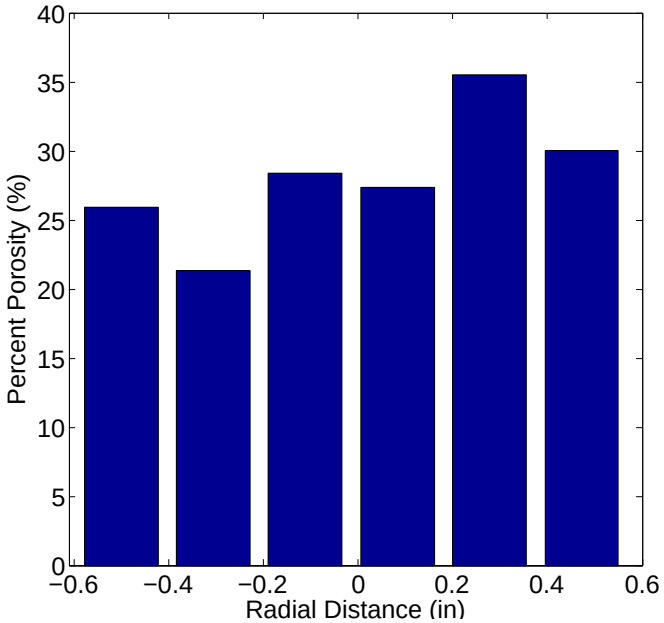

Figure 4.23: Porosity at Various Locations along Cross Section of Dynamically Compacted Powder at 0.203 GPa)

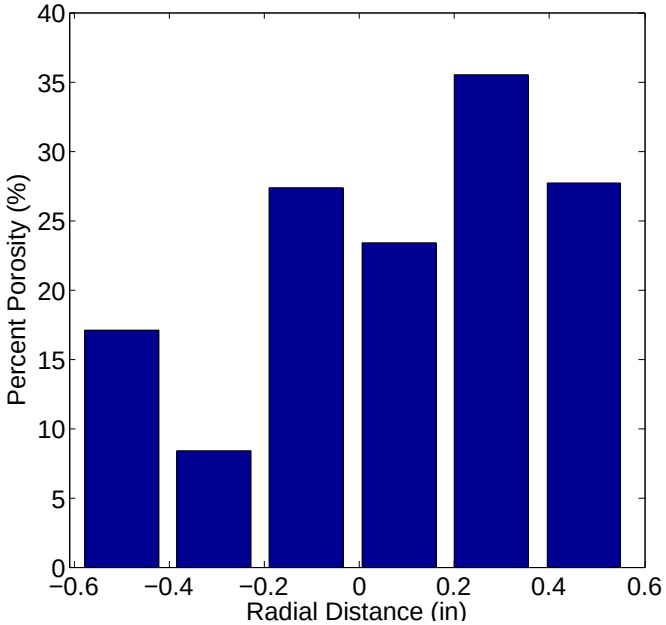

Figure 4.24: Porosity at Various Locations along Cross Section of Dynamically Compacted Powder at 0.501 GPa)

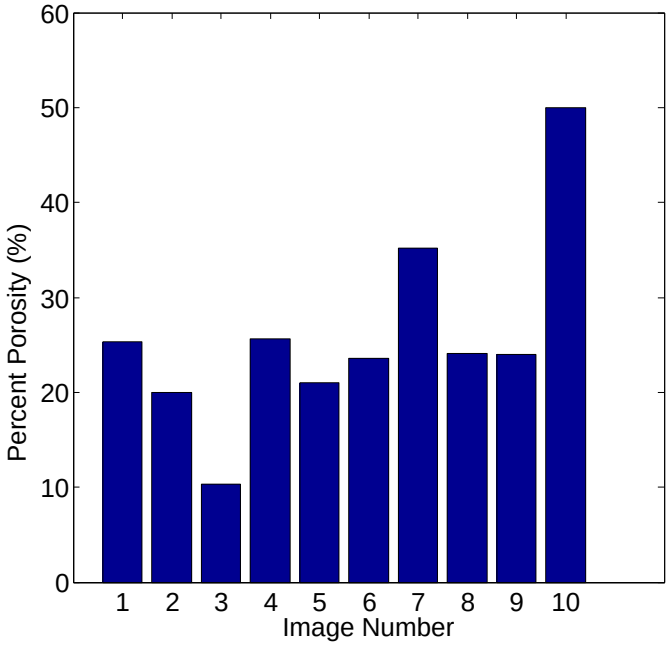

Figure 4.25: Porosity at Various Locations along Cross Section of Pressed and Sintered Powder at 0.203 GPa)

Table 4.8: Porosity using Image Manipulation of Powder Compacts Under Various Loading Conditions

Compaction Method	Average Porosity (%)	Resulting Density (g/cc)	Standard Deviation (%)
Dynamic-0.203GPa	28.1	4.487	4.7
Dynamic-0.501GPa	23.3	4.789	9.4
Pressed-Sintered	25.9	4.622	10.4

Figures 4.23-4.25 and Table 4.8 indicate that as the compaction pressure increased the porosity decreased. This correlation was expected through intuition. However, by observing the images in Appendix I, it was expected that the pressed and sintered compacts would result in lower porosity than the dynamic compaction. This expectation was observed when the high porosity data point (50%) in Figure 4.25 and the low porosity data point (8.4%) in Figure 4.24 were removed. This resulting in porosity for the dynamic compaction at 0.501GPa and Pressed and Sintered Method of 26.2% and 23.2% respectively. These results are more in line with what was expected upon initial inspection. Therefore, increasing the pressure by 250% will only reduce the porosity by 1.9%. This is a large amount of pressure increase for very little gain in further compaction. Once again, this could be a result of a release wave in tension traveling through the powder increasing the porosity and breaking apart constituents bonded together.

The comparison of the final densities achieved by consulting the experimental data from the flyer-plate experiments and the image analysis yielded comparable results. The experimental data as seen in Figure 4.13 resulted in a final density of 4.479 g/cc at 0.201GPa and a final density of 4.753 g/cc at 0.501GPa. These densities are close to those listed in Table 4.8. The resulting percent differences in the density determination for compaction at 0.203GPa and 0.501GPa was 0.18% and 0.76% respectively. The experimental density was determined based on the incident pressure wave traveling through the powder, while the density determined through imaging was determined by examining the sample after all pressure waves had subsided. This result indicates that there may not have been a release wave in tension traveling through the powder disrupting the compacted

sample, since the density upon initial compaction and post-experiment were nearly identical. However, it is important to note that substantial error may exist in the imaging method which can not be quantified in addition to the error in the experimental method which was roughly 12% utilizing the error analysis methods discussed in Appendix A.

CHAPTER 5

Conclusions

The work presented in this thesis aimed to accomplish three important tasks of shock physics research: developing a working data acquisition system, deriving equation of state in U_S-U_p Space, and comparing morphologies of static and dynamic compaction methods. Each task was completed and the results were consistent with published literature. The work presented, especially that pertaining to the construction of Manganin Gage Targets, will progress the shock physics research at Marquette University. It will also combine new research endeavors between the shock physics group and manufacturing groups in the area of granular materials.

The data acquisition system was able to consistently and accurately obtain both projectile velocity and stress waveforms. The modifications of the projectile allowed for projectile velocities that were greater and more repeatable than those presented in the research of Downs while using more massive projectiles. The inclusion of the Mylar shim in the stress gage targets, though needed to encapsulate the Manganin gages, proved to reduce the peak amplitude between aluminum interfaces in addition to increasing the incident rise times. These can be seen in the comparison of the experimental data to the impedance matching technique where the experimental peak pressure adhered to the 10% or more reduction in peak pressure mentioned by Linde [11]. In addition, the inclusion of the Mylar shim yielded a Power-Law Analysis that was consistent with materials in laminate composites with an exponent of roughly 2.5. The Power-Law of the back gage was also less than the front gage as expected to the distortion of the stress wave traveling through the granular mixture.

The experimental data in U_s-U_p space was fit with a linear equation of state as is common practice in the shock physics community. The equation of state was developed for several scenarios based on various impedance matching techniques, Manganin gage hysteresis, and the presence of the Mylar shim. It was determined

that the calculation method based on the experimental pressure (Methods 1 and 3) provided the most statistically accurate values for the Hugoniot slope and bulk sound speed. The resulting equation of state compared favorably with experimental data available in literature based on the initial density and particle velocity. The initial density was less than those available in literature and therefore the experimental data in the present research resided below the data tabulated in literature. The one-dimensional KO computer simulations also clearly resembled the stress waveform for the data acquisition system and qualitatively support the equation of state developed here. The KO simulations over predicted the peak pressure and underestimated the rise-time which is consistent with literature and expected based on the observed response of the Mylar shim. The experimental data also straddled the porous Hugoniot and $P - \alpha$ model adjusted for porosity and was above the $P - \alpha$ model for granular copper as was expected.

The dynamic compaction of the granular powder produced samples that were of higher porosity than the statically pressed and sintered samples. However, the arrangement of the individual constituents in the dynamic compaction closely resembled those of the statically compacted. Based on the inability of most copper particles to bond together, the use of this method for manufacturing processes requires more development. The images also suggested that release waves in tension may have been present in the powder sample causing the sample to break apart as indicated by the "puzzle" type orientation of the particles. A higher level computer simulation would be required to determine if this is the case.

Lastly, further experiments were deemed necessary to completely characterize the results in the present research. These experiments will need to be conducted on a gas gun capable of producing projectile velocities up to 1 km/s.

5.1 Future Work

The Marquette University SSGG could utilize several improvements to improve safety and functionality. There can also be changes made to the velocity and stress measurement system to improve the results and repeatability of the devices. Also, further simulations and experiments can be implemented to better characterize the pressure traces, analyze the phenomena observed, and study the

response of the heterogeneous powder to loading. Lastly, many unexpected problems existed in conducting the research which will provide pivotal insight to future research. The following sections will touch on considerations for each of the areas of improvement mentioned above.

5.1.1 Marquette University SSGG

There exist several area to improve safety for the operators of the SSGG. The operators of the SSGG must currently remain several feet from the pressurized vessels and the speeding projectile. To improve safety it is recommended to purchase a variable control valve to replace the needle valve for the gas booster inlet. This will allow for operation of the gas gun outside of the room during the launching of the projectile. In addition an automated pressure gauge would be useful if the control valve is implemented to know the continuous pressure in the breech. Two camera's feeding live data of the velocity and stress measurement systems could be considered to observe any premature triggering of the system due to noise. Consideration should also be given to construction of a breech and barrel capable of launching 2 inch projectiles. The use of 2 inch projectiles will expand the working area of the target and lengthen the time required for shock waves in the radial direction to reach the Manganin gage. This will result in more accurate measurements of the pressure at the gage. In addition, the larger breech will result in higher projectile velocities which would aid immensely in developing the $U_s - U_p$ linear equation state with velocities in the range of data available in literature. The present research was capable of projectile velocities in a range of 70 m/s where a range of 500 - 1000 m/s would be ideal. At higher projectile velocity's it is predicted that the equation of state in U_s-U_p will exhibit more linearity. Also, it is anticipated that greater compaction of the powder sample will occur and quite possibly reduce to the porosity to states less than the statically pressed and sintered compacts. A vacuum chamber at the barrel end would eliminate the need of having to hold vacuum on the barrel end. This would improve the ability to pull vacuum immensely in addition to reducing the time and labor required to machine a target. If the vacuum chamber is not feasible, several o-rings should be added to the SSGG to aid in pulling vacuum. O-rings should be located at the barrel end and the

vacuum holder. Also a bolting system should be implemented to create an improved seal on the vacuum pin system and the target at the barrel end. A sturdier jack in the Target chamber with a wider platform would be helpful for relieving stress on the barrel and the weight of the anvil, along with areas to rest the cables entering the chamber.

5.1.2 Velocity and Stress Measurement Systems

The velocity and stress measurement systems could be greatly improved with the changes stated in the SSGG section above. Removing the requirement of holding vacuum on the target would greatly improve the overall functionality of the target and the labor necessary to manufacture one. With no vacuum a target cylinder could be developed to allow the front plate to slip in the cylinder. This would result in easier compacting of the powder using the MTS with improved planarity of the front plate. In addition, a wider cylinder capable of resting the entire Manganin Gage without forcing the gage to span several crevices would be preferable. Also, thought should be given to developing a target that could be compressed from the back. This could also result in improved planarity and location of the gage on the front plate. Also, the purchase of encapsulated manganin gages would eliminate the need for a mylar insulator (Vishay Micro Measurements Part Number: LM-SS-210FD-050/SP60). As seen in the data analysis the mylar insulated greatly effects the shape of the pressure waveform. The velocity pin system will need new graphite guides machined due to the damage they incur during an experiment. Also, a current two-channel oscilloscope with storage capabilities would greatly improve the accuracy in the projectile velocity measurements in addition to the immense functions available on current oscilloscopes. A digital voltage supply with multiple channels would be useful for running the velocity measurement system in addition to running several of the suggestions in the SSGG section. Also, experiments should be considered while altering the oscilloscope settings. The oscilloscope contains several measurement methods such as averaging and RMS which could produce cleaner waveforms. However, the potential tradeoff would be a reduction in the number of data points captured by the oscilloscope. It would also be interesting to analyze different projectile configurations. Boring a larger hole in

the back of the projectile would lighten the projectile and intuition would suggest faster projectile velocity. An analysis of projectile configurations could increase the range of the SSGG with the current experimental apparatus.

5.1.3 Further Research Considerations

Further insight into the behavior of the heterogeneous powder could be gained by changing parameters in the experiments. It would be interesting to develop equations of state for the heterogeneous powder at varying powder densities. Experiments at powder densities of 3.75 g/cc and 4.5 g/cc could introduce new phenomena to the powder response to dynamic loading. In addition, the fully compacted and sintered compact at 6.21 g/cc should be subjected to dynamic loading. Also, the duration of the sintering process could be considered when analyzing the dynamic compaction of the powder and if the sintering time has a measurable effect on the resulting sample. The microstructure analysis of each post-experiment compact could indicate new constituent orientation and bonding.

Also, further high-level 2D simulations should be performed on the pressure waveforms. A two-dimensional simulations will conclude if a second Hugoniot state was reached on the front gage trace. In addition, the effect of the small sample area could be analyzed to determine which aspect of the target is contributing to the shape of the waveforms. Also, additional equations of state such as the $P - \alpha$ model could be developed to compare with the experimental data to further characterize the powder behavior to loading at varying density and pressure. It would be interesting to also analyze the temperature produced in the powder during shock loading and what effect alterations in the projectile velocity and target configuration have on the temperature observed.

Lastly, further research should be conducted in the 1.5GPa pressure range. From conducting the research it appears there is some anomalous behavior that exists in this pressure range, which is most likely a result of the boundary between elastic and plastic regimes. An improved method would be useful to analyze shock experiments at 1.5 GPa due to the breakdown of the fourth-power law and hysteresis in the manganin gages.

5.1.4 Lessons Learned during Present Research

There were many lessons learned while performing the present research that contributed greatly to the outcome of this research. The lessons learned are connected to the behavior of the equipment used in addition to the fragility and sensitivity of the components.

The behavior of the piezoelectric pin proved to result in troublesome results when trying to set the oscilloscope delay and trigger location. The first consideration is to insure the pin is completely isolated from its environment other than at the connection to the pigtail and above the surface of the target. If precaution is not taken the pin can easily be shorted. Also, the requirement of the target to hold vacuum on the barrel resulted in initially unexpected behavior of the pin. The coupling of a low vacuum level in the barrel with an un-vented barrel created pressures capable of causing the pin to trigger the scope before the projectile reached the pin. Also, not evacuating the barrel could cause the air to ionize and become conductive causing the pin to short prematurely [6]. One of the seven target assemblies considered was aimed at using the triggering of the oscilloscope from the pin and a single gage on the target back plate to determine the transit time through the powder. The earlier triggering of the pin however prevent reliable determination of the triggering point by as much as 40 microseconds.

In addition, the wiring for an individual line in the research building is not rated for the loads drawn by the experimental equipment. It is therefore essential to make sure the equipment is isolated on serval different circuits to prevent fuses from being blown. The introduction of UPS greatly improved this behavior but did not eliminate it completely.

Also, there are numerous connections between varying components of each system. For example, there are seven connections between the oscilloscope and manganin gage. As, a result noise in the cables is almost certain to occur. Therefore, as with the piezoelectric pin it is essential to isolate the components from each other with large noise sinks and aluminum foil insulation. It is also of importance to make sure all connections are sound especially the soldering of the leads onto the manganin gage. Epoxy should be liberally applied to make sure this

connection is well isolated and secure. Also, the gages are extremely fragile and should not be placed on any surface capable of being deformed.

Lastly, countless triggering methods were tried to trigger the velocity and stress measurement systems. It was found that the two measurement systems can not be located on the same oscilloscope due to the resolution of the oscilloscope and the inability to control the time elapsed between the completion of the velocity pin circuit to impact with the target. In addition, with the size of the flyer plates used any rigid component placed in the path of the projectile will deform the surface of the projectile. A copper break wire was implemented as an effort to trigger the oscilloscope however extensive damage occurred to the flyer plate in addition to not properly triggering the oscilloscope. The piezoelectric pin also caused significant damage to the flyer plate however the oscilloscope for stress measurement could be properly triggered with the pin. A larger flyer plate could reduce the effect the pin has on distorting the surface of the flyer plate.

REFERENCES

[1] Z. Rosenberg. The use of manganin gauges in shock reverberation experiments. *Journal of Applied Physics*, 52(6):4000–4002, June 1981.

[2] D. K. Dijken and J. Th De Hosson M. Shock wave equation of state of powder material. *Journal of Applied Physics*, 75(2):809–813, January 15 1994.

[3] R. R. Boade. Principle hugoniot, second-shock hugoniot, and release behavior of pressed copper powder. *Journal of Applied Physics*, 41(11):4542–4551, October 1970.

[4] *LASL Shock Hugoniot Data*, 1980.

[5] John P. Borg, David J. Chapman, Kostas Tsembelis, William G. Proud, and John R. Cogar. Dynamic compaction of porous silica powder. *Journal of Applied Physics*, 98:073509–1–7, October 5 2005.

[6] Marc Andre Meyers. *Dynamic Behavior of Materials.* John Wiley and Sons Inc, New York City, 1994.

[7] W. H. Gourdin. Dynamic consolidation of metal powders. *Progress in Material Science*, 30:39–80, 1986.

[8] Kevin S. Vandersall and Naresh N. Thadhani. Shock compression of mo-si powder mixtures using recovery and instrumented experiments. In M. D. Furnish, L. C. Chhabildas, and R. S. Hixson, editors, *Shock Compression of Condensed Matter*, pages 763–766. Georgia Institute of Technology, American Institute of Physics, 1999.

[9] R. R. Boade. Compression of porous copper by shock waves. *Journal of Applied Physics*, 39(12):5693–5702, November 1968.

[10] Vonne D. Linse. The particulate nature of dynamic compaction. *Metallurgical Applications of Shock-Wave and High-Strain-Rate Phenomena*, pages 29–55, 1986.

[11] Ronald K. Linde and David N. Schmidt. Shock propagation in nonreactive porous solids. *Journal of Applied Physics*, 37(8):3259–3271, July 1966.

[12] Ronald K. Linde, Lynn Seaman, and David N. Schmidt. Shock response of porous copper, iron, tungsten, and polyurethane. *Journal of Applied Physics*, 43(8):3367–3375, August 1972.

[13] P. C. Lynse and W. J. Halpin. Shock compression of porous iron in the region of incomplete compaction. *Journal of Applied Physics*, 39(12):5488–5495, November 1968.

[14] D. E. Grady. Shock attenuation in distended media. *AIP Conference Proceedings*, 1195(1):1031–1054, 2009.

[15] W. Herrmann. Constitutive equation for the dynamic compaction of ductile porous materials. *Journal of Applied Physics*, 40(6):2490–99, May 1969.

[16] Michael Carroll and Albert C. Holt. Suggested modification of p-alpha model for porous materials. *Journal of Applied Physics*, 43(2):759–761, 1972.

[17] A. Ferreira and M. A. Meyers. Method for determining pressure for shock compaction of powders. *Shock-Wave and High-Strain Rate Phenomena in Materials*, pages 361–370, 1992.

[18] L. Boshoff and H. J. Vijoen. Comparative study of analytical methods for hugoniot curves of porous materials. *Journal of Applied Physics*, 86(3):1245–1254, August 1 1999.

[19] W. H. Gourdin. Energy deposition and microstructural modification in dynamically consolidated metal powders. *Journal of Applied Physics*, 55(1):172–181, September 19 1983.

[20] D. E. Grady, N. A. Winfree, G. I. Kerley, and L. T. :Kuhns Wilson L.D. Computational modeling and wave propagation in media with inelastic deforming microstructure. *Journal of Physics, IV France*, 10:9–15–20, 2000.

[21] Lee Davison, Y. Horie, and Mohsen Shahinpoor. *High-Pressure Shock Compression of Solids IV : Response of Highly Porous Solids to Shock Loading*. Springer, New York, 1997.

[22] David J. Benson and W. J. Nellis. Dynamic compaction of copper powder:computation and experiment. *Applied Physics Letters*, 65(4):418–420, July 25 1994.

[23] Shao Binghuang, Wang Xiaolin, and Liu Zhiyue. Equation of state of porous material in explosive compaction. *Shock-Wave and High-Strain Rate Phenomena in Materials*, pages 473–481, 1992.

[24] Dennis E. Grady. Structured shock waves and the fourth power law. *Journal of Applied Physics*, 1195(3):1–13, January 6 2010.

[25] John P. Borg, John R. Cogar, A. Lloyd, A. Ward, David J. Chapman, Kostas Tsembelis, and W. G. Proud. Computational simulations of the dynamic compaction of porous media. *International Journal of Impact Engineering*, 33:109–118, 2006.

[26] Thomas J. Downs. The development of a single stage light gas gun and velocity measurement system. Master's thesis, Marquette University, 2006.

[27] unknown. Manganin pressure gages- a review. *Unknown*, pages 1–6, January 20 1987.

[28] Dynasen Inc. Piezoelectric pins. `http://www.dynasen.com/html/piezopinpage.html`, 1996.

[29] Agilient Technologies. *Agilent InfiniiVision 5000/6000/7000 Series Oscilloscopes*.

[30] Dynasen Inc. *Piezoresistive Pulse Power Supply Model: CK2-50/0.050-300 Instruction Manual*.

[31] Z. Rosenberg, D. Yaziv, and Y. Partom. Calibration of foil-like manganin gauges in planar shock wave experiments. *Journal of Applied Physics*, 51(7):3702–3705, January 25 1980.

[32] L.M. Lee. Calibration of thin-foil manganin gauge in alox materials. In *Shock Compression of Condensed Matter*. Ktech Corp, American Physical Society, August 1995.

[33] The Boeing Company. Hugoniot equation of state of mylar, March 1969.

[34] G. Ravichandran S. Zhuang and D.E. Grady. An experimental investigation of shock wave propagation in periodically layered composites. *Journal of the Mechanics and Physics of Solids*, 51:245–265, 2003.

[35] Mark L. Wilkins. *Computer Simulation of Dynamic Phenomena*. Springer, New York, 1999.

[36] R. Byron Bird, Warren E. Stewart, and Edwin N. Lightfoot. *Transport Phenomena*. John Wiley and Sons, New York, 2002.

[37] A. C. Whiffinr. The use of flat-ended projectiles for determining dynamic yield stress. ii. tests on various metallic materials. *Proceedings of the Royal Society of London. Series A, Mathematical and Physical Sciences*, 194:300–322, Sep. 2 1948.

[38] Tao Tan. Personal interview.

[39] David J. Benson. The calculation of the shock velocity-particle velocity relationship for a copper powder by direct numerical simulation. *Wave Motion*, 21:85–99, 1995.

[40] David J. Benson. An analysis by direct numerical simulation of the effects of particle morphology on the shock compaction of copper powder. *Modeling Simulation Material Science Engineering*, 2:535–550, 1994.

[41] John P. Borg and K. B. Jordan. Equation of state development as applied to extremely porous heterogeneous materials. pages 1353–1356. Marquette University, American Institute of Physics, June 28-July 3 2009.

[42] John P. Borg and Tracy J. Vogler. Mesoscale calculations of the dynamic behavior of a granular ceramic. *International Journal of Solids and Structures*, 45:1676–1696, November 5 2008.

[43] L. C. Chhabildas. Survey of diagnostic tools used in hypervelocity impact studies. *International Journal of Impact Engineering*, 5:205–220, 1987.

[44] Emanuale Coglioti, Vittorio Loreto, Hans J. Herrmann, and Mario Nicodemi. A "tetris-like" model for the compaction of dry granular media. *Physical Review Letters*, 79(8):1575–1578, Aug 25 1997 1997.

[45] G. E. Duvall. The physics connection. *Metallurgical Applications of Shock-Wave and High-Strain-Rate Phenomena*, pages 3–25, 1986.

[46] D. E. Grady. Analytic solutions and constitutive relations for shock propagation in porous materials. pages 205–208, Furnish, M.D.; Gupta, Y.M.; Forbes, J.W., 2003. Applied Research Associates, American Institute of Physics.

[47] Paul Harris. The gruneisen constant of porous materials in energy deposition materials. *Picatinny Arsenal Technical Report 4255*, pages 1–27, August 1971.

[48] Vitali F. Nesterenko. *Dynamics of Heterogeneous Materials*. Springer, New York, 2001.

[49] A. P. Polyakov. The effect of parameters of dynamic loading on the propagation character of shock waves in a powder. *Russian Journal of Non-Ferrous Metals*, 50(1):33–38, 2009.

[50] D. Raybould. The cold welding of powders by dynamic compaction. *The International Journal of Powder Metallurgy and Powder Technology*, 16(1):9–18, 1980.

[51] A. D. Resnyansky. Constitutive modeling of hugoniot for a highly porous material. *Journal of Applied Physics*, 104:093511–1–14, 2008.

[52] A. D. Resnyansky and N. K. Bourne. Shock-wave compression of a porous material. *Journal of Applied Physics*, 95(4):1760–1769, November 18 2003 2004.

[53] O. V. Sadovskaya and V. M. Sadovskii. Elastoplastic waves in granular materials. *Journal of Mechanics and Technical Physics*, 44(5):741–747, March 3 2003.

[54] H. W. Sandusky and T. P. Liddiard. Dynamic compaction of porous beds. *Naval Surface Warfare Center*, pages 1–53, 1985.

[55] Kevin S. Vandersall and Naresh N. Thadhani. Time-resolved measurements of the shock-compression response of mo+2si elemental powder mixtures. *Journal of Applied Physics*, 94(3):1575–1583, August 1 2003.

[56] Chris Wensrich. Dissipation, dispersion, and shocks in granular media. *Powder Technology*, 126:1–12, 2002.

[57] J.R. Taylor. *Introduction to Error Analysis: The Study of Uncertainties in Physical Measurements*. University Science Books, California, 1997.

[58] Hewlett Packard. *54600-Series Oscilloscope User and Service Guide*.

[59] IET Labs. *Certificate of Calibration*.

[60] Andrew Fraser. Mesoscale behavior of an aluminum-manganese dioxide-epoxy mixture under shock loading: from milli to nano-sized aluminum particles. Master's thesis, Marquette University, 2009.

APPENDIX A

Error Analysis

A brief discussion of the error analysis calculations employed to the experimental results will be described in this section. The error analysis will be applied to the experimental results in experiments 22-26. The basis of the error analysis was developed in part by the text of J.R. Taylor describing uncertainties in physical measurements and most importantly the propagation of error through numerical calculations [57]. It is important to note that many of the uncertainties based on the Hugoniot data represents a lower bound to the error obtained in the experimental research, since it was assumed there was not error in the calculation data. This is especially true in the calculation of the particle velocity which was taken by reading the $P - U_p$ Hugoniot at an experimental pressure. Since, a majority of the calculations involved equations with numerous variables, a methodology was developed based on statistics and the Taylor series of error. The resulting error in an equation can be determined by:

$$\delta f = \pm \left[\left(\delta x_1 \frac{\delta f}{\delta x_1} \right)^2 + \left(\delta x_2 \frac{\delta f}{\delta x_2} \right)^2 + ... + \left(\delta x_n \frac{\delta f}{\delta x_n} \right)^2 \right]^{\frac{1}{2}} \tag{A.1}$$

where δx_n is the uncertainty in a particular variable.

A.1 Density Uncertainty

The density was determined from an untraditional method due to the construction process of the target. The lack of planarity required an average to be taken for the height measurements of the cylinder used to contain the powder. The volume of the powder in the cylinder was calculated using

$$V = \pi \frac{D^2}{4} (h_{cylinder} - h_{step} - h_{piston}) \tag{A.2}$$

where D is the diameter of the cylinder, $h_{cylinder}$ is the height of the cylinder,

h_{step} is the distance from the top of the cylinder to the piston, and h_{piston} is the height of the piston.

The height of the cylinder was determined by acquiring 4 measurements of the cylinder height over the surface of the cylinder using a Browne & Sharpe Reflex 343 DMM . The height of the step on the other hand was found by taking 15 measurements over the surface of the piston with the Browne & Sharpe Reflex 343 DMM . The piston thickness and diameter was determined by using a dial caliper.

Therefore, a measurement error of 1/2 the resolution of the device was used to describe the piston thickness and diameter and a standard error (σ) was used to describe the uncertainty of $h_{cylinder}$ and h_{step} using the standard deviation (s)

$$s = \sqrt{\frac{\sum_{i=1}^{N}(x_i - \bar{x})}{N-1}} \tag{A.3}$$

$$\sigma = \frac{s}{\sqrt{N}} \tag{A.4}$$

Therefore, the uncertainty in the volume can be calculated using the formula based on Equation A.1 below:

$$\delta V = \pm\left[\left(\delta D\frac{\delta V}{\delta D}\right)^2 + \left(\delta h_{cylinder}\frac{\delta V}{\delta h_{cylinder}}\right)^2 + \left(\delta h_{step}\frac{\delta V}{\delta h_{step}}\right)^2 + \left(\delta h_{piston}\frac{\delta V}{\delta h_{piston}}\right)^2\right]^{\frac{1}{2}} \tag{A.5}$$

The density which is defined as mass over volume can then be calculated using Equation A.1 with the volume uncertainty defined above and mass uncertainty defined as 1/2 the resolution of the measurement device.

$$\delta\rho = \pm\left[\left(\delta V\frac{\delta\rho}{\delta V}\right)^2 + \left(\delta m\frac{\delta\rho}{\delta m}\right)^2\right]^{\frac{1}{2}} \tag{A.6}$$

The density uncertainty's were on average 2.3% of the density measurement. This was considered excellent considering the number steps required to determine the powder density, but was greatly assisted by the high precision equipment used.

A.2 Projectile Velocity Uncertainty

The uncertainty in the projectile velocity (v) was determined using a similar method outline by Downs [26]. However, the measurement methods differed in the two projectile velocity calculations. The projectile velocity was defined as distance (d) over time (t).

The distance between the velocity pin sets was determined using a microscope from which the distance uncertainty was said to be 1/2 the resolution of the device. The time uncertainty on the other hand was determined using the manufactures calculations presented in the manual [58]. The time uncertainty is governed by the equation:

$$\delta t = 0.01\% PulseWidth + 0.2\% of FullScale + 200ps \tag{A.7}$$

The resulting uncertainty in the projectile velocity can be determined by adapting Equation 4.12 below:

$$\delta v = \pm \left[\left(\delta d \frac{\delta v}{\delta d} \right)^2 + \left(\delta t \frac{\delta v}{\delta t} \right)^2 \right]^{\frac{1}{2}} \tag{A.8}$$

The uncertainty for the velocity through the each of the three time locations was averaged to determine the uncertainty in the total projectile velocity. As was discussed previously, the projectile velocity uncertainty's were very similar to those calculated by Downs differing by no more than 1 m/s [26]. On average the projectile velocity uncertainty composed only 1.2% of the projectile velocity measurement

A.3 Pressure Uncertainty

The uncertainty in pressure measurements as seen in Equation 4.5 is only a function of the percent change in resistance however the resistance change was determined from the calibration plot in Figure 2.18 which is also function of Voltage. The fit used to represent the calibration data was not representative of all the calibration data (not all data points were on the curve), however the calibration data'a variation from the fit was less than 0.03%. Figure 2.18. Therefore, the contribution in error of the calibration curve needs to be determined based on the

error attributed to vertical deviation from the curve (Voltage) and horizontal deviation from the curve (Percent Change in Resistance). The error in the measurement of Voltage and Percent Change of Resistance must first be determined.

The error in the Voltage measurement was determined from the manufactures manual to be: [29]

$$\delta V = \pm 2.0\% Full Scale \tag{A.9}$$

The error in the percent change in resistance was determined from the propagation of error and Equation A.1. The error in a particular resistance measurement was defined by the owners manual which is dependent on the resistance decade used [59]. The error in the percent change in resistance is define below:

$$\delta \frac{\Delta R}{R_0} = \pm \left[\left(\delta \Delta R \frac{\delta \frac{\Delta R}{R_0}}{\delta \Delta} \right)^2 + \left(\delta R_0 \frac{\delta \frac{\Delta R}{R_0}}{\delta R_0} \right)^2 \right]^{\frac{1}{2}} \tag{A.10}$$

where ΔR is defined as $R - R_0$ for some measured R.

Now that the measurement uncertainties have been obtained the data must be compared to the calibration fit to determine the potential deviation between the data and the fit. To obtain this deviation for the percent change in resistance the quadratic formula was used to determine the percent change in resistance for a given voltage based on the calibration second order fit. The percent change in resistance from the data was then compared to the simulation for the quadratic formula using:

$$error = \sqrt{(data - fit)^2} \tag{A.11}$$

The standard deviation was then applied to the error in all the data points from Equation A.11 and it was determined that the deviation between the data and the fit for the percent change in resistance was large enough that it had to be included in the measurement uncertainty. Therefore, the deviation error and measurement error were summed to get the total uncertainty in the percent change in resistance.

A similar method was used to find the deviation in the vertical direction

from the calibration fit based on the uncertainty in the Voltage measurement. The second order calibration fit was then adjusted to incorporate the uncertainty in the Voltage measurement. The quadratic formula was then applied to get the resulting percent change in resistance. The deviation between the data and fit was then determined using Equation A.11. This deviation will represent the uncertainty in percent change in resistance due to the uncertainty in the Voltage. Therefore the total uncertainty in percent change in resistance will be the sum of the uncertainty contributed to the Voltage in the vertical axis and the percent change in resistance in the horizonal axis.

The uncertainty in the pressure can then be determined by applying Equation A.1 to Equation 4.5 using the uncertainty in percent change in resistance calculated above.

$$\delta P = \pm \left[\left(\delta \frac{\Delta R}{R_0} \frac{\delta P}{\frac{\Delta R}{R_0}} \right)^2 \right]^{\frac{1}{2}} \tag{A.12}$$

The percent uncertainty in the pressure measurements were on average 12.2% which is very similar to the 10.7% uncertainty depicted in the pressure measurements in the research of Fraser [60]. However, it is noted that Manganin gages were used in the research of Fraser but the data analysis procedure was not described.

A.4 Particle Velocity Uncertainty

The particle velocity was determined from the Impedance Matching Technique. Therefore, Equation 1.6 was used to determine the particle velocity which will result in particle velocity being a function of density, Hugoniot slope, bulk sound speed, pressure, and projectile velocity. Since the density, Hugoniot slope and bulk sound speed were not experimentally determined and obtained from the LASL data they will be considered constants. Therefore, the particle velocity will be assumed to be a function of pressure and projectile velocity only. The quadratic formula will then be applied to Equation 1.6 to solve for the particle velocity U_p. The resulting equation for particle velocity will be:

$$U_p = \frac{2S\rho v + \sqrt{(2S\rho v)^2 - 4s\rho(S\rho v^2 - \rho C_0 v - P)}}{2S\rho} \tag{A.13}$$

The uncertainty in the particle velocity can then be calculated using Equation 4.12.

$$\delta U_p = \pm\left[\left(\delta v\frac{\delta U_p}{v}\right)^2 + \left(\delta P\frac{\delta U_p}{P}\right)^2\right]^{\frac{1}{2}} \tag{A.14}$$

The average percent particle velocity uncertainty was 10.6 % compared to the 12.3 % tabulated by Fraser [60]. This was expected to be lower since the current research did not experimentally determine the particle velocity while the research discussed by Fraser implemented a VISAR system for continuous particle displacement versus time.

A.5 Shock Velocity Uncertainty

Equation 4.5 was used to determine the shock velocity of a flyer plate experiment. The shock velocity is a function of the thickness of the powder, the transit time, and the particle velocity's through the various media of the target. The particle velocity's uncertainty was determined from the method outline in the previous uncertainty section on particle velocity. The uncertainty in the powder thickness is determined in a similar manner to that of the powder volume. The powder thickness is defined as

$$PowderThickness(d) = h_{cylinder} - h_{step} - h_{piston} \tag{A.15}$$

Therefore, the uncertainty in the powder thickness is simply the sum of the uncertainty of each of the components: $h_{cylinder}, h_{step}, h_{piston}$.

The uncertainty in the time measurement was obtained from the oscilloscope manual [29]. This uncertainty is described by the formula below:

$$\delta t = \pm 2(15ppm) \tag{A.16}$$

The oscilloscope was set to 5 mircoseconds/division therefore the uncertainty in the time measurement will be 1.5 nanoseconds.

The uncertainty in the shock velocity can then be calculated using Equation A.1.

$$\delta U_s = \pm \left[\left(\delta d \frac{\delta U_s}{d} \right)^2 + \left(\delta t \frac{\delta U_s}{t} \right)^2 + \left(\delta U_{p1} \frac{\delta U_s}{U_{p1}} \right)^2 + \left(\delta U_{p2} \frac{\delta U_s}{U_{p2}} \right)^2 \right]^{\frac{1}{2}} \tag{A.17}$$

The average percent shock velocity uncertainty was determined to be 2.9 % compared to the 6.4% determined stated in the research of Fraser [60]. This discrepancy could be due to the target configuration and the inability in the current research to experimentally determine the particle velocity through the copper shim and mylar encapsulating sheet.

A.6 Conclusion

From the uncertainty calculations detailed above, the uncertainty's in the remaining results can be determined. These uncertainties include those obtained for the fourth-power law analysis, the wavelength, and other shock velocity calculation methods. There are areas for improvement in the uncertainty's of the experimental quantities which can be obtained by implementing suggestions in the Future Work section of this thesis. However, the results of the uncertainty calculations were encouraging for those that were directly comparable to data available in open literature.

APPENDIX B

Experimental Procedures

The following experimental procedures offer set-up and maintenance guidelines for operation of the Marquette University Single Stage Gas Gun. The experimental procedures will be broken into pre-experiment procedures and post experiment procedures. The pre-experiment procedures will outline the steps required to prepare the SSGG for a flyer plate experiment, while the post-experiment will offer guidelines for the proper maintenance of the SSGG. For brevity not all the procedures were included, however a more detailed instruction in stress gage target instruction can be found in Appendix F. Detailed descriptions of the velocity measurement system set-up, projectile construction, powder creation, polishing method, and microscopy procedures can be found in the present research file. The procedures below are only meant to be guidelines for operation of the SSGG and the owners manual of individual equipment must be consulted for greater equipment understanding and operation.

The assumptions have been made that the experimental apparatus has been completely unassembled prior to beginning an experiment.

1. Preparation of the Breech

    (a) Apply vacuum grease to the o-rings on the upstream and downstream side of the breech

    (b) Apply vacuum grease to the inlet of the barrel

    (c) Apply vacuum grease to both o-rings of the sabot

2. Load the Projectile

    (a) Insert the projectile from the upstream side of the removable breech housing

(b) Make sure the projectile is flush with the end of the breech housing. Note: If the projectile does not fit properly, a rubber mallet may have to be used. Be mindful that the o-rings do not get damaged during loading.

3. Attach Copper Shear Disk

   (a) Cut a Shear disk of copper shim stock in a hexagonal shape to fit between the breech bolt hole pattern

   (b) Attach the shim to the breech using electrical tape (electrical tape performs better than masking/duct tape when contacted with vacuum grease)

4. Assemble the Breech and Gun barrel using the 3/8-24 UNF bolts and clamps

   (a) Assemble such that vacuum inlet ports are pointing upwards (toward ceiling)

   (b) Apply pressure with the gun barrel and rotate slightly against the breech while tightening the bolts to insure that the breech o-rings seat properly.

   (c) Place the Velocity Measurement System Bolt Block in it's channel under the barrel

   (d) Place a level on the barrel and raise the manual jack until the barrel is level

      i. Make sure the bolt holes in the block are spaced evenly on each side of the barrel (This is required for fitting the Velocity Measurement System to the barrel)

   (e) Tighten the bolts until they are snug

5. Test the Breech and Barrel Vacuum system

   (a) Attach the vacuum tubing to their appropriate location on the breech and barrel.

(b) The tubing exiting the downstream ball valve should be attached to the barrel

(c) The tubing exiting the upstream ball valve should be attached to the breech

(d) Close the upstream ball valve and turn on the vacuum pump for 3-5 minutes. The vacuum gauge should reach 30 inHg.

i. If the vacuum level does not remain near 30 inHg. Cycle the pump 2-3 times followed by 3-5 minutes of continuous operation.

ii. If the vacuum holds, open the upstream ball valve on move to step 7.

iii. Otherwise, disassemble and reassemble the breech system and repeat vacuum trial.

6. Assemble Velocity Measurement System

(a) Apply vacuum grease to the velocity pin holder on the barrel

(b) Apply vacuum grease to both sides of the red-rubber gasket

(c) Place the red-rubber gasket onto the barrel while applying pressure and rotating slightly to get a snug connection

(d) Apply vacuum grease to the bottom of the velocity pin system

(e) Fit the Velocity Pin System to the barrel using the bolt holes as a guide (Be mindful not to break the graphite)

(f) Shine a flash light down the barrel end to make sure no graphite rods are broken and they are at an appropriate depth to contact the flyer plate.

(g) Apply vacuum grease in a circular pattern around the top of the velocity pin block

(h) Apply vacuum grease to both o-rings on the Vacuum Sleeve

(i) Place the Vacuum Sleeve over the velocity pin; applying pressure and rotating to create a proper seal

(j) Bolt the velocity pin block to the bolt block. Tighten by hand until the bolts are snug. Do not over tighten as any skewing in planarity will prevent vacuum from being held on the barrel

(k) Apply vacuum grease to the Acrylic Lid

(l) Fix the copper wire from the velocity pin block to the leads on the Acrylic Lid

(m) Place the Acrylic Lid on the Vacuum Sleeve. Apply pressure and rotate slightly to insure a proper seal is made

7. Test Vacuum on Velocity Measurement System

(a) Apply vacuum grease to the end of the barrel

(b) Place red rubber gasket material (with vacuum grease on the surface) to the end of the barrel.

(c) Use a piece of metal (angle iron) to apply pressure to the gasket.

(d) Turn on the Vacuum Pump

(e) While the Vacuum Pump is running apply pressure and rotate the Acrylic Lid and Vacuum Sleeve.

(f) Cycle the Vacuum Pump 2-3 times

(g) The vacuum gage should read 30 inHg. (If the vacuum level is decreasing substantially repeat appropriate steps above

(h) If the vacuum level is decreasing at 5 inHg per 10min. This is adequate to perform the experiment

8. Set-Up the Velocity Data Acquisition System

(a) Attach banana plug/ alligator clip assemblies to the Acrylic Lid, Oscilloscope, and Digital Voltage Supply

i. 1 banana plug must run from the Digital Voltage Supply (+) to Acrylic Lid Terminal

ii. 1 banana plug must fun from Digital Voltage Supply (-) to Oscilloscope Ground

iii. 1 banana plug must run from Oscilloscope (+) to remaining Acrylic Lid Terminal

(b) Plug the Oscilloscope into the UPS (Noise, Surge, and Battery Terminal)

(c) Plug the Digital Voltage Supply into the UPS (Batter and Surge Terminal)

(d) Turn on the Oscilloscope

i. Enable Channel 1

ii. Select 50 microseconds/div

iii. Select 0.500 mV/div

iv. Choose to Trigger off Channel 1

v. Select Rising Trigger

vi. Set Trigger Voltage to 0.500 mV

vii. Make sure Trigger is set to Normal

viii. Select Single (Scope will now be waiting for 0.500 mV)

ix. Scale Vertical Axis near the bottom of the viewing window

x. Set Delay to 230 microseconds

9. Test Velocity Pin System

(a) Turn on Digital Voltage Supply and Set Voltage to 0.500 mV

(b) Remove Cable from Acrylic Lid and make contact with the other Alligator Clip (Terminal). This will be completing the circuit

(c) Scope should trigger and a square wave at 1.5V should be seen over the entire viewing window

(d) Repeat Several Times to insure proper functionality

(e) If trace does not appear, check connections and Oscilloscope settings and Repeat Testing Procedure

10. Set-Up Stress Measurement System

(a) Plug Agilent DSO6054A Oscilloscope into UPS (Noise, Surge, and Battery Terminal)

(b) Plug Dynasen Pulse Power Supply into UPS (Batter and Surge Terminal)

(c) Discharge Capacitor on Pulse Power Supply and verify the voltage returns to 46-50 V

(d) Connect the Dynasen and Oscilloscope as represented in Dynasen Manual in conjunction with the Stress Gage

(e) Follow Balancing procedure for both Manganin Gages as represented in Dynasen Manual

(f) Connect the Dynasen and Oscilloscope as represented in Dynasen Manual in conjunction with the Variable Resistor Decade Box

(g) Follow Procedure to Calibrate Pulse Power Supply as represented in Dynasen Manual

(h) Record Voltage and Resistance in Lab Notebook (Most calibration data should surround the gage resistance) The gage resistance can easily be determined by adjusting the variable resistance supply and firing until the scope is once again balanced.

(i) Set-Up Oscilloscope for Stress Measurement (see Figure 2.16)

i. Power Channel 1 and Channel 3

ii. Set Horizontal increment to 5 microseconds/ div

iii. Set Vertical increment to 50 mV/ div

iv. Set Trigger to External

v. Set Trigger to Rising Slope

vi. Set Trigger to 0.750 mV

vii. Set Delay depending on piezoelectric pin distance from impact surface

viii. Make sure channel impedance is set to 50 ohms.

ix. Set Vertical Position near center of the screen, but allow enough space so pulse does not get clipped.

x. Connect Oscilloscope Trigger Output to the Trigger of the Dynasen Pulse Power Supply

xi. Arm Oscilloscope (Single) and Dynasen to wait for a Trigger

xii. Connect the BNC gage cables to the Manganin Gages

xiii. Trigger the Oscilloscope through the External Trigger with a 3V Battery. Check to make sure the scope triggered and the gage traces are balanced

(j) Disconnect BNC cables from gages

(k) Reapply Vacuum Grease to Barrel End

(l) Apply Vacuum Grease to the surface of the stress target

(m) Fit the Stress Target to the barrel end (Be careful not to break the piezoelectric pin by making contact with the barrel) Apply pressure and rotate slightly

(n) Feed the BNC piezoelectric pigtail through the anvil and connect to the Pin.

(o) Connect the other end to the Oscilloscope External Trigger

(p) Snug the Anvil up to the Target (Make sure the Piezoelectric Pin is in the center of the Anvil Circuit Isolator. Use Shims as necessary to insure pin is centered in Isolator.

(q) Turn on Vacuum Pump and let run for 3-5 minutes

(r) Cycle Vacuum Pump 2-3 times and check that vacuum level is 0-30 inHg (Adjust components as necessary)

(s) Back Anvil off Target and Use Multimeter to insure there is continuity between the BNC pigtail and the piezoelectric pin

(t) Snug Anvil against Target

(u) Close Door to Target Chamber: Be sure not to crimp the cords and induce personal injury due to weight of the chamber door

11. Pressurize and Ready Gas Gun for Experiment

(a) Make sure all occupants have ear and eye protections and no persons are located in the adjacent rooms.

(b) If any problems attributed to the air delivery system arise, depressurize the breech immediately and close the upstream needle valve on the filtration system

(c) Make sure the compressor and air dryer are connected to separate circuits

(d) Check the three-way-ball valve is oriented for use in the 1" SSGG

(e) Make sure the air supply needle valve of the gas booster is closed

(f) Close the upstream needle valve to the filtration system

(g) Turn on Air compressor

(h) Turn on Air Dryer

(i) Allow the pressure in the compressor tank to reach 100 psi

(j) Turn off Compressor

(k) Open needle-valves on filtration system (Air should now enter the adjacent tubing and gas booster driver cylinder)

(l) Slightly open the air supply needle valve on the gas booster.

(m) Allow the breech to pressurize to 75% of the pressure required to burst the copper shim as noted in thesis of Downs [26] and close air supply needle valve

(n) Repressurize the Air compressor to 100 psi and turn off.

(o) Arm the Velocity Measurement System and the Stress Measurement System

(p) Turn on the Vacuum Pump for several minutes and insure the vacuum level is near 30 inHg.

(q) Close upstream ball valve on vacuum pump system to prevent high pressure air from entering the pump.

(r) Turn off the Air Dryer

(s) Open the air supply needle valve until the copper shim ruptures and the sabot is sent down the barrel.

(t) Close the air supply needle valve

Post-Experiment Procedures

1. Close upstream needle valve on filtration system to prevent compressor from draining down barrel end
2. Turn off the Dynasen Pulse Power Supply
3. Save the Stress Gage Data on the DSO6054A Oscilloscope using the instructions below (indicated in owner's manual)
   (a) Insert USB drive to Front Panel of Oscilloscope
   (b) Select Save-Recall Softkey on the Front panel of Oscilloscope
   (c) Choose "Settings"
      i. Choose "Length"
      ii. Turn "Cursor" knob until maximum number of data points is selected (200,000 for 5 microsecond/div)
   (d) Return to Save-Recall Menu
      i. Choose Save "ASCII XY data"
      ii. Select "Push to Save"
      iii. Choose "8 bit BMP"
      iv. Select "Push to Save"
   (e) Before Turning off Oscilloscope upload data into available computer to insure the data has been saved correctly
4. Record Velocity Measurement Data
   (a) Select "Measure" from the panel Softkeys
   (b) Choose "Time"
   (c) Use front panel cursor knob to transverse the trace
   (d) Record the time location of each voltage spike relative to 0 microseconds

(e) Take Several Pictures of Oscilloscope Trace

(f) Perform calculation to insure velocity is in expected range before turning off oscilloscope

5. Discharge Air from valve on bottom of compressor tank (This will remove all moisture from the tank)

6. Remove Air Compressor and Air Dryer extension cords and place on shelf to prevent injury from tripping

7. Open Door to Target Chamber: Be sure not to crimp the cords and induce personal injury due to weight of the chamber door

8. Disconnect Stress Gage wires from BNC connector adapters

9. Disconnect Alligator Clips from Vacuum Lid

10. Disconnect Pigtail to Piezoelectric Pin: Check if any damage was caused to the pigtail assembly (brass connector)

11. Remove all wires and cables from Target Chamber

12. Remove Velocity Pin System from the Target Chamber by loosening mounting bolts

(a) Place on wooden blocks

(b) Loosen Nuts on Acrylic Lid to release wires (Remove Lid)

(c) Remove Vacuum Sleeve

(d) Loosen Bolts from Copper Busses: Remove Copper Busses

(e) Use Mechanical Pencil with 0.0197" Drill bit to remove graphite from graphite guides

(f) Clean all Velocity Pin System Components, removing all vacuum grease, powder, and graphite pieces.

13. Remove red-rubber gasket from velocity pin holder: Remove all vacuum grease and particulate
14. Remove all vacuum grease from velocity pin holder and barrel end
15. Remove the Stress Target from the chamber for post-experiment examination
16. Vacuum up all particulate in the vacuum chamber: Sabot pieces and particulate
17. Open the door to the breech chamber
18. Disconnect the Vacuum tubing from the Breach and Barrel and slide outside of the vacuum chamber
19. Remove the 3/8-24 UNF Bolts and clamps from the Breech Assembly
20. Remove the barrel from the breech and remove the breech plate, placing the breech plate on a clean surface
21. Clean the breech plate and breech inlet surfaces removing all vacuum grease, particulate, and tape adhesive. Remove, clean , and install the breech assembly o-rings
22. Clean barrel using pushrod and toweling. The barrel is clean when the toweling exiting the barrel contains no residue
23. Clean-up the lab as necessary for the next experiment
24. Double-Check all lab electronics are turned off
25. Open the upstream ball valve of the vacuum system
26. Make sure the compressor tank is empty (0 PSI) and close the valve under the tank
27. Drain the Filter-Regulator to the Gas Booster of all liquid and particulate as needed
28. Check the compressed air and vacuum system to insure all valves are in there proper orientation

APPENDIX C

Tabulated Data

Table C.1: Cumulative Experimental Data

Test #	Flyer Material	Target Configuration	Shim	Projectile Mass	Projectile Diameter	Density	Projectile Velocity	Front Gage Pressure	Back Gage Pressure
1	Al	Al/G/P/G/PMMA	0.007	NA	0.969 ± 0.0005	NA	NA	NA	NA
2	Al	Al/G/P/G/PMMA	0.007	NA	0.969 ± 0.0005	NA	247.10 ± 3.06	NA	NA
3	Al	Al/G/Al/P/G/PMMA	0.007	NA	0.969 ± 0.0005	NA	NA	NA	NA
4	Al	Al/G/Al/P/G/PMMA	0.007	NA	0.969 ± 0.0005	NA	NA	NA	NA
5	Al	Al/P/Al	0.007	NA	0.969 ±0.0005	NA	252.83 ± 3.20	Recovery	Recovery
6	Al	Al/P/Al	0.007	NA	0.994± 0.0005	NA	259.74± 3.37	Recovery	Recovery
7	Al	Al/P/G/PMMA	0.007	NA	0.994± 0.0005	NA	Blown Fuse	Blown Fuse	Blown Fuse
8	Al	Al/G/Al	0.007	NA	0.994± 0.0005	NA	No Trigger	No Trigger	No Trigger
9	Al	Al/G/Al	0.007	NA	0.994± 0.0005	NA	No Trigger	No Trigger	No Trigger
10	Al	Al/MY/G/Al	0.007	NA	0.994± 0.0005	NA	No Trigger	1.727 ± 0.262	No Gage
11	Al	Al/MY/G/Al	0.007	21.4731± 0.00005	0.994± 0.0005	NA	259.74± 3.37	No Trigger	No Gage
12	Al	Al/MY/G/Al	0.007	21.6843± 0.00005	0.994± 0.0005	NA	251.08± 2.34	1.682± 0.292	No Gage
13	Al	Al/P/MY/G/AL	0.007	22.0907± 0.00005	0.996± 0.0005	2.618± 0.079	253.11± 3.331	No Gage	No Trigger
14	Al	Al/P/Cu/MY/G/AL	0.005	21.4696 ± 0.00005	0.996± 0.0005	2.523± 0.074	219.78± 2.44	No Gage	0.982± 0.277
15	Al	Al/P/Cu/MY/G/AL	0.007	21.9784 ± 0.00005	0.996± 0.0005	3.254± 0.067	253.11± 2.44	No Gage	1.568± 0.246
16	Al	Al/P/Cu/MY/G/AL	0.004	21.5844 ± 0.00005	0.996± 0.0005	2.770± 0.036	No Trigger	No Gage	0.901± 0.269
17	Al	Al/P/Cu/MY/G/AL	0.004	22.2322 ± 0.00005	0.996± 0.0005	2.586± 0.035	215.57± 2.33	No Gage	1.149± 0.259
18	Al	Al/P/Cu/MY/G/AL	0.006	21.48797 ± 0.00005	0.996± 0.0005	2.675± 0.041	242.59± 2.95	No Gage	1.256± 0.261
19	Al	Al/P/Cu/MY/G/AL	0.007	21.9262± 0.00005	0.996± 0.0005	2.608± 0.050	262.81± 3.46	No Gage	1.646± 0.247
20	Al	Al/P/Cu/MY/G/AL	0.005	21.6388 ± 0.00005	0.996± 0.0005	2.812± 0.039	209.87± 2.21	No Gage	1.379± 0.253
21	Al	Al/MY/G/Al/P/Cu/MY/G/AL	0.005	21.3724 ± 0.00005	0.997± 0.0005	2.690± 0.055	219.51± 2.41	1.402± 0.126	Trace Not Captured
22	Al	Al/MY/G/Al/P/Cu/MY/G/AL	0.004	21.7553 ± 0.00005	0.997± 0.0005	2.886± 0.055	197.78± 1.96	0.987± 0.144e	0.925± 0.129
23	Al	Al/MY/G/Al/P/Cu/MY/G/AL	0.006	22.2764± 0.00005	0.997± 0.0005	2.712± 0.069	240.66± 2.90	1.279± 0.140	1.218± 0.142
24	Al	Al/MY/G/Al/P/Cu/MY/G/AL	0.007	22.1534 ± 0.00005	0.997± 0.0005	2.713± 0.071	256.09± 3.28	1.388± 0.138	1.332± 0.136
25	Al	Al/MY/G/Al/P/Cu/MY/G/AL	0.008	22.3349 ± 0.00005	0.997± 0.0005	2.747± 0.077	271.14± 3.68	0.893± 0.148	1.276± 0.167
26	Al	Al/MY/G/Al/P/Cu/MY/G/AL	0.007	22.3267 ± 0.00005	0.997± 0.0005	2.724± 0.050	262.91± 3.46	1.627± 0.134	1.130± 0.146

Table C.2: Experimental Data for Calculating Fourth Power-Law for Front Gage in Aluminum 2.70 g/cc

Experiment #	Projectile Velocity (m/s)	Peak Pressure (GPa)	90% Peak Pressure (GPa)	40% Peak Pressure (GPa)	Strain Time (sec)	Method 1 $\dot{\epsilon}$ $(sec)^{-1}$	Method 2 $\dot{\epsilon}$ $(sec)^{-1}$	Method 3 $\dot{\epsilon}$ $(sec)^{-1}$
22	197.78± 1.96	0.987±0.144	0.888±0.130	0.395±0.058	2.10E-07	2.951E+04± 5.63E+02	2.984E+04± 3.31E+03	4.377E+04±9.36E+02
23	240.66±2.90	1.279±0.140	1.152±0.126	0.512±0.056	2.27E-07	3.650E+04±4.82E+02	3.537E+04±3.33E+03	4.841E+04±7.66E+02
24	256.09±3.28	1.388±0.138	1.249±0.124	0.555±0.055	2.03E-07	4.234E+04±5.25E+02	4.287E+04±3.68E+03	5.764E+04±1.04E+03
25	271.14± 3.68	0.893±0.148	0.804±0.133	0.357±0.059	3.02E-07	1.878E+04±4.06E+0	1.878E+04±2.71E+03	4.078E+04±1.00E+03
26	262.91± 3.46	1.627±0.134	1.464±0.120	0.650±0.053	1.52E-07	6.571E+04±8.66E+02	6.652E+04±4.70E+03	7.890E+04±2.15E+03

Table C.3: Experimental Data for Calculating Fourth Power-Law for Back Gage in Aluminum 2.70 g/cc

Experiment #	Projectile Velocity (m/s)	Peak Pressure (GPa)	90% Peak Pressure (GPa)	40% Peak Pressure (GPa)	Strain Time (sec)	Method 1 $\dot{\epsilon}$ $(sec)^{-1}$	Method 2 $\dot{\epsilon}$ $(sec)^{-1}$
22	197.78± 1.96	0.925±0.129	0.832±0.116	0.370±0.052	4.21E-07	1.373E+04±2.69E+02	1.860E+04±1.71E+03
23	240.66± 2.90	1.218±0.142	1.096±0.128	0.487±0.057	3.49E-07	2.299E+04±3.06E+02	3.096E+04±2.24E+03
24	256.09± 3.28	1.332±0.136	1.199±0.122	0.533±0.054	2.12E-07	3.864E+04±5.02E+0	5.203E+04±3.54E+03
25	271.14± 3.68	1.276±0.167	1.149±0.150	0.511±0.067	3.02E-07	2.604E+04±3.36E+02	3.531E+04±3.13E+03
26	262.91± 3.46	1.130±0.146	1.017±0.131	0.452±0.058	2.86E-07	2.525E+04±4.15E+02	3.404E+04±2.84E+03

Table C.4: Flyer Plate Experimental Results Note: The Particle and Shock Velocities were obtained using Method 1 with no Hysteresis

Experiment #	Density ρ_0 (g/cc)	Projectile Velocity (m/s)	Calculated particle velocity U_p (m/s)	Measure shock velocity U_s (m/s)	Measured peak pressure (GPa)	Calculated peak pressure (GPa)	Measured release pressure (GPa)	Gage transit time (μsec)	Front plate t_a (mm)	Back piston t_b (mm)	Powder thickness t_p (mm)	Copper shim t_s (mm)	Back plate t_d (mm)
22	2.886±0.055	198±1.96	186±25	522±16	0.987±0.144	1.479	0.203±0.159	3.449	0.8128	0.8128	1.709±.055	0.1016	25.4
23	2.712±0.069	241±2.90	208±22	641±18	1.279±0.140	1.791	0.476±0.151	3.014	0.8128	0.8128	1.820±0.065	0.1016	25.4
24	2.713±0.071	256±3.28	226±23	738±21	1.388±0.138	1.909	0.433±0.159	2.637	0.8128	0.8128	1.818±0.077	0.1016	25.4
25	2.747±0.077	271±3.68	237±22	561±16	0.893±0.148	2.025	0.501±0.156	3.377	0.8128	0.8128	1.797±0.078	0.1016	25.4
26	2.724±0.050	263±3.46	239±23	537±15	1.627±0.134	1.960	0.341±0.1583.550		0.8128	0.8128	1.812±0.055	0.1016	25.4

Table C.5: Data for KO Computer Simulation Input File for Experiment 26 with Projectile Velocity 263 m/s

Material	Material Length (cm)	Density (g/cm^3)	Bulk Sound Speed (cm/μ s)	Hugoniot Slope	Gamma	Dynamic Yield Strength (Mbar)	Shear Strength (Mbar)	C_V (Mbar cm^3/(g K)
Projectile-Al	0.9652	2.70	0.531	1.35	2.0	5.4e-3	2.6e-1	9.6e-6
Front Plate-Al	0.0813	2.70	0.531	1.35	2.0	5.4e-3	2.6e-1	9.6e-6
Mylar Shim	0.010	1.39	0.222	1.59	0.0	2.8e-3	1.3e-3	1.3e-6
Back Piston-Al	0.0813	2.70	0.531	1.35	2.0	5.4e-3	2.6e-1	9.6e-6
Powder	0.181	2.72	0.046	0.63	0.0	1.1e-4	1.4e-2	0.1e-6
Copper Shim	0.010	8.93	0.395	1.50	1.99	1.6e-3	4.8e-1	3.9e-6
Mylar Shim	0.010	1.39	0.222	1.59	0.0	2.8e-3	1.3e-3	1.3e-6
Back Plate-Al	0.50	2.7	0.531	1.35	2.0	5.4e-3	2.6e-1	9.6e-6

APPENDIX D

Oscilloscope Traces of Two-Gage Target Experiments

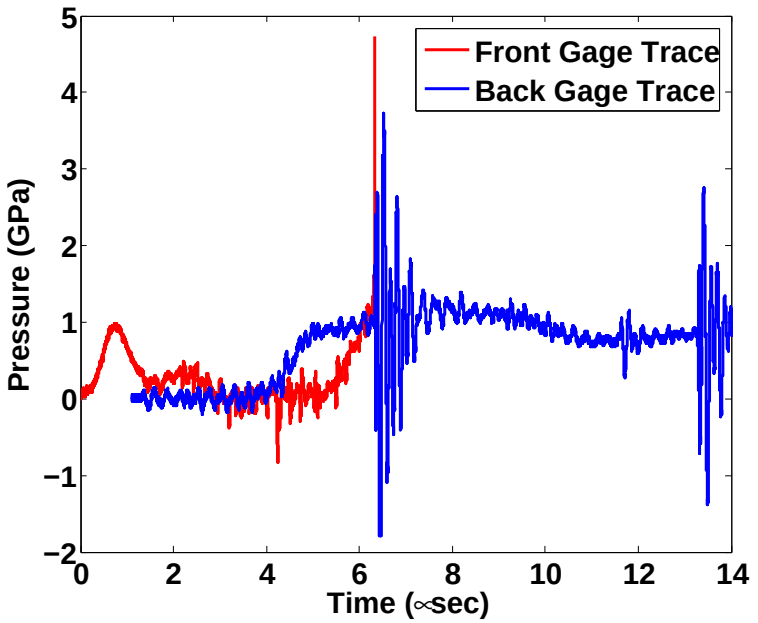

Figure D.1: Pressure Trace for Experiment 22 over 14 Microseconds Shot Velocity 198 m/s and Powder Density 2.886 g/cc.

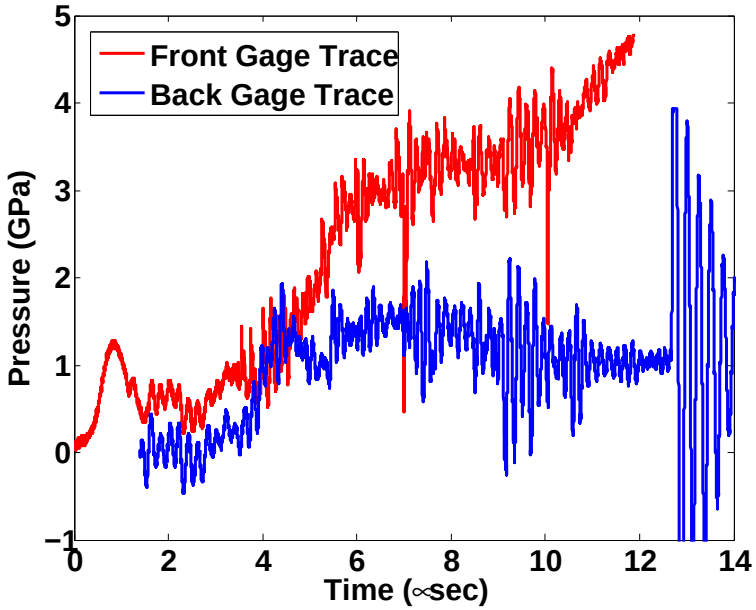

Figure D.2: Pressure Trace for Experiment 23 over 14 Microseconds Shot Velocity 241 m/s and Powder Density 2.712 g/cc.

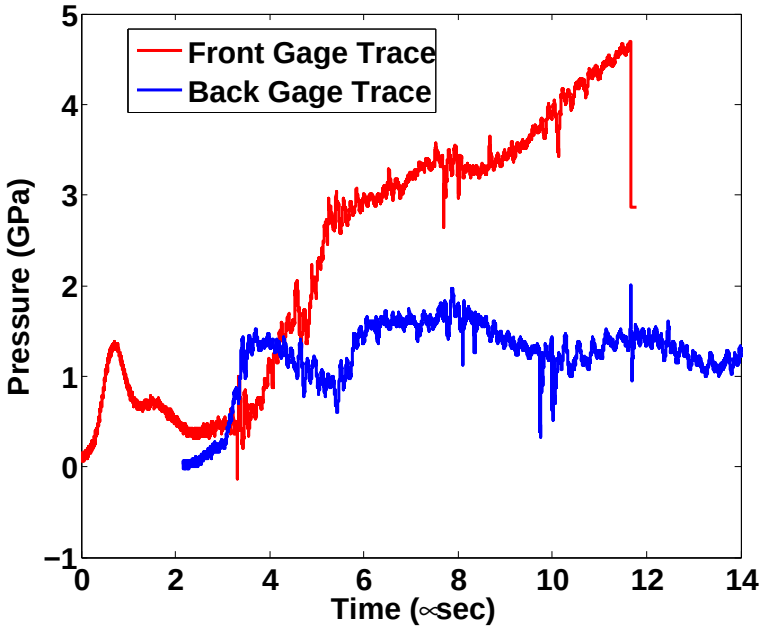

Figure D.3: Pressure Trace for Experiment 24 over 14 Microseconds Shot Velocity 256 m/s and Powder Density 2.713 g/cc.

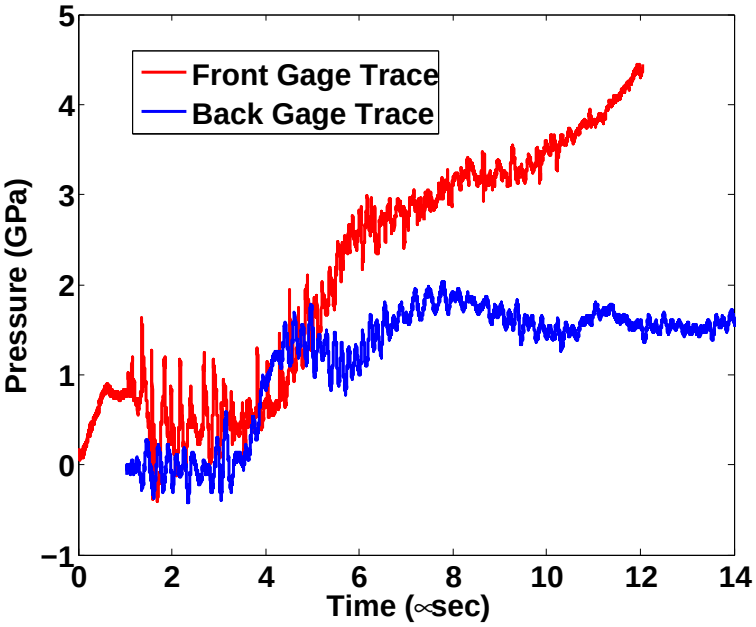

Figure D.4: Pressure Trace for Experiment 25 over 14 Microseconds Shot Velocity 271 m/s and Powder Density 2.747 g/cc.

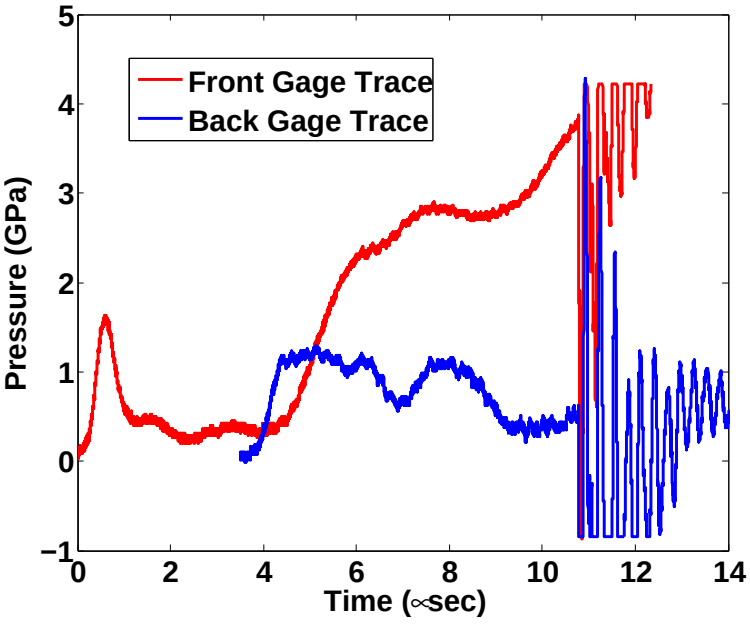

Figure D.5: Pressure Trace for Experiment 26 over 14 Microseconds Shot Velocity 263 m/s and Powder Density 2.724 g/cc.

APPENDIX E

Bulk One-Dimensional Simulations

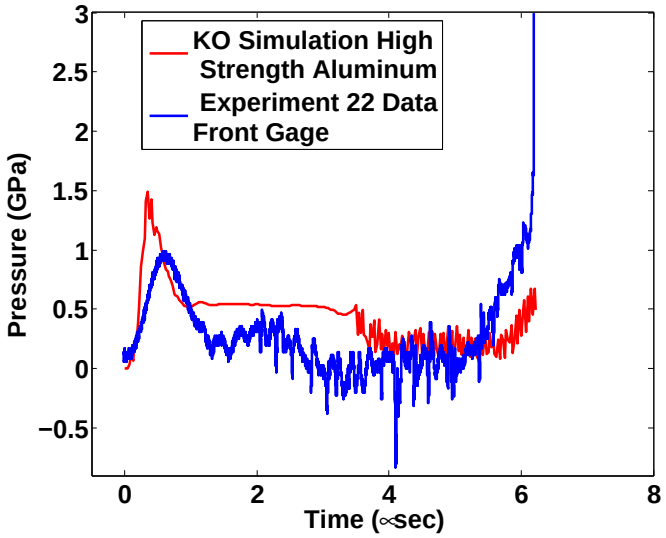

Figure E.1: Front Gage Simulation and Experiment Pressure Trace for Experiment 22 over 14 Microseconds. Shot Velocity 198 m/s and Powder Density 2.886 g/cc.

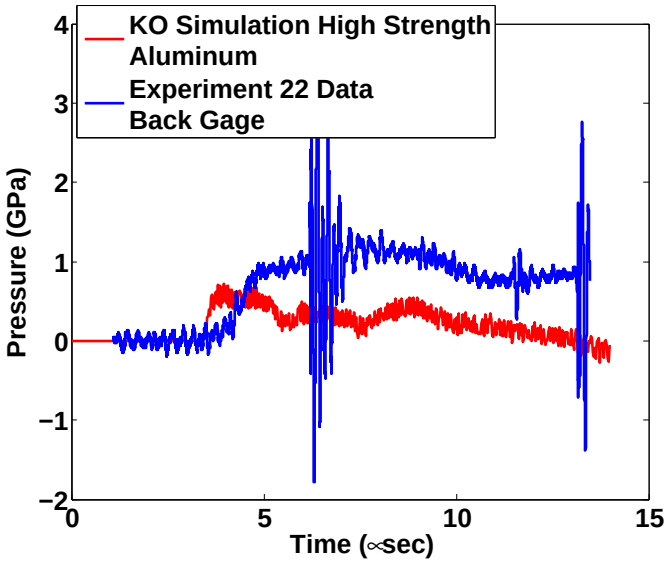

Figure E.2: Back Gage Simulation and Experiment Pressure Trace for Experiment 22 over 14 Microseconds. Shot Velocity 198 m/s and Powder Density 2.886 g/cc.

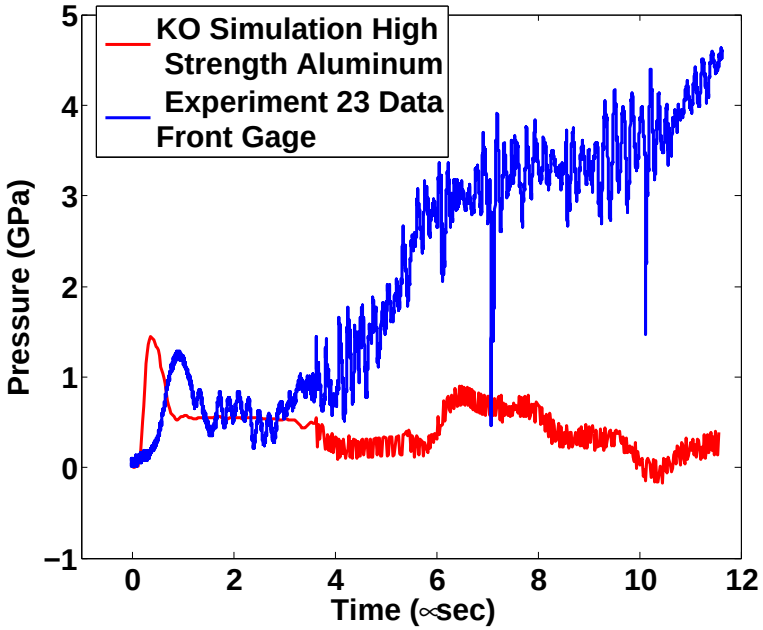

Figure E.3: Front Gage Simulation and Experiment Pressure Trace for Experiment 23 over 14 Microseconds. Shot Velocity 240 m/s and Powder Density 2.712 g/cc.

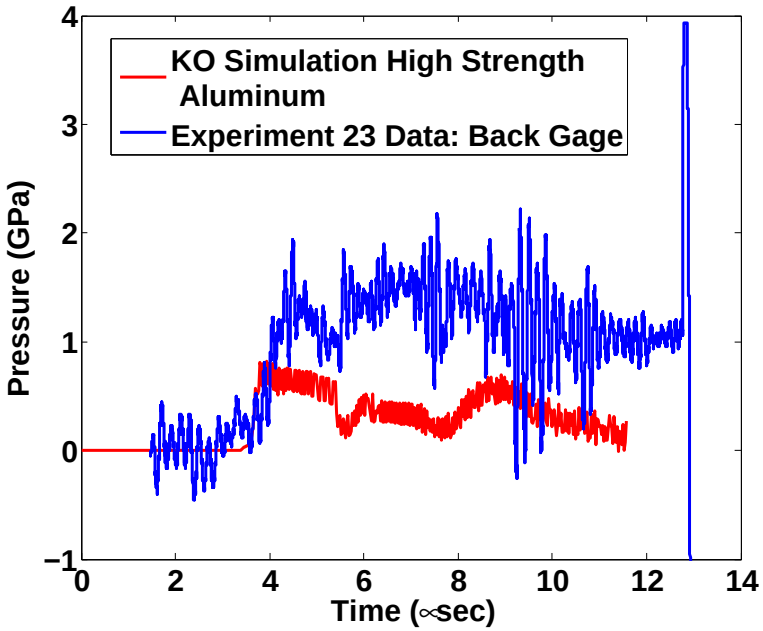

Figure E.4: Back Gage Simulation and Experiment Pressure Trace for Experiment 23 over 14 Microseconds. Shot Velocity 240 m/s and Powder Density 2.712 g/cc.

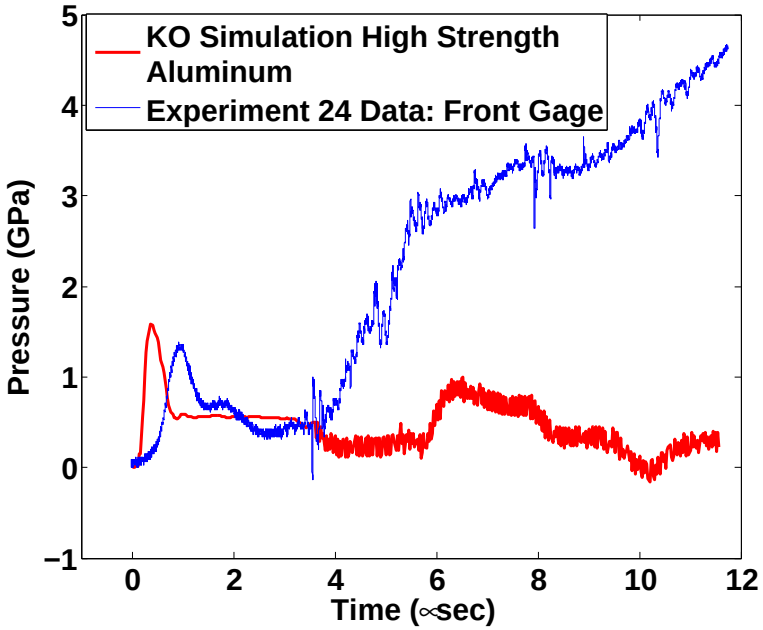

Figure E.5: Front Gage Simulation and Experiment Pressure Trace for Experiment 24 over 14 Microseconds. Shot Velocity 256 m/s and Powder Density 2.713 g/cc.

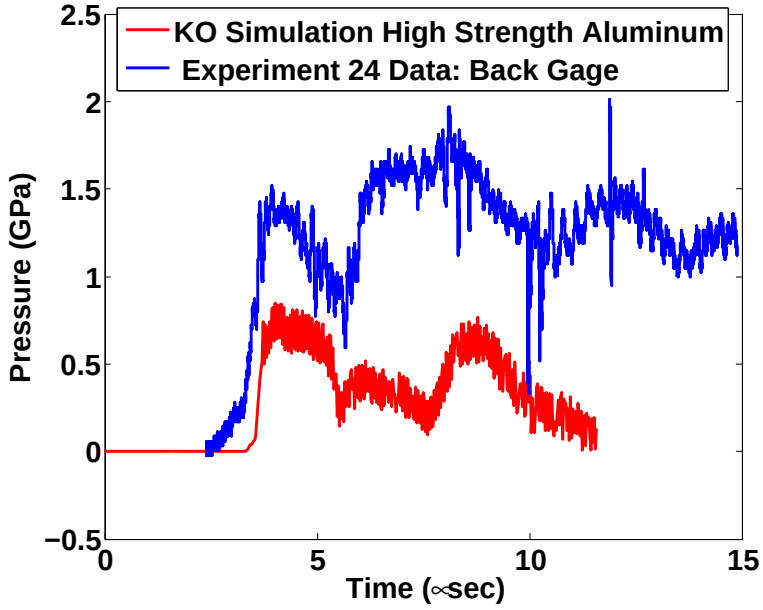

Figure E.6: Back Gage Simulation and Experiment Pressure Trace for Experiment 24 over 14 Microseconds. Shot Velocity 256 m/s and Powder Density 2.713 g/cc.

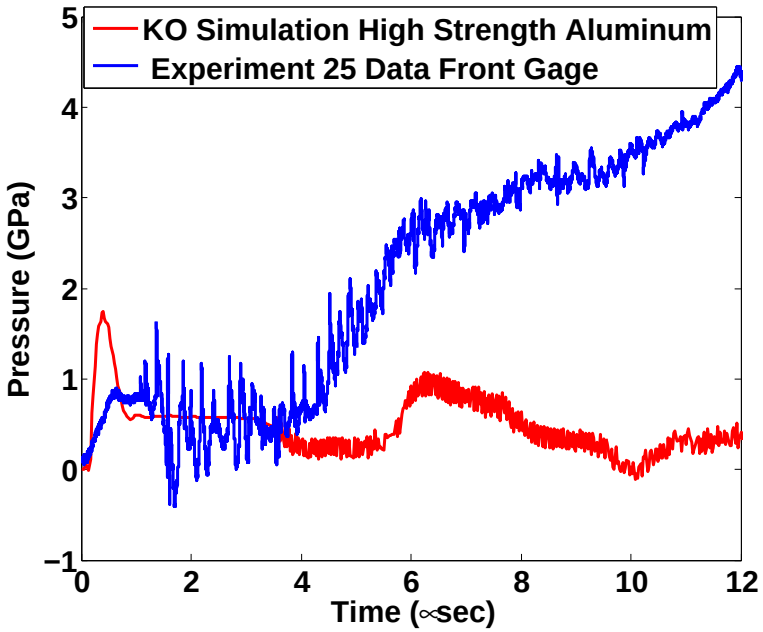

Figure E.7: Front Gage Simulation and Experiment Pressure Trace for Experiment 25 over 14 Microseconds. Shot Velocity 271 m/s and Powder Density 2.747 g/cc.

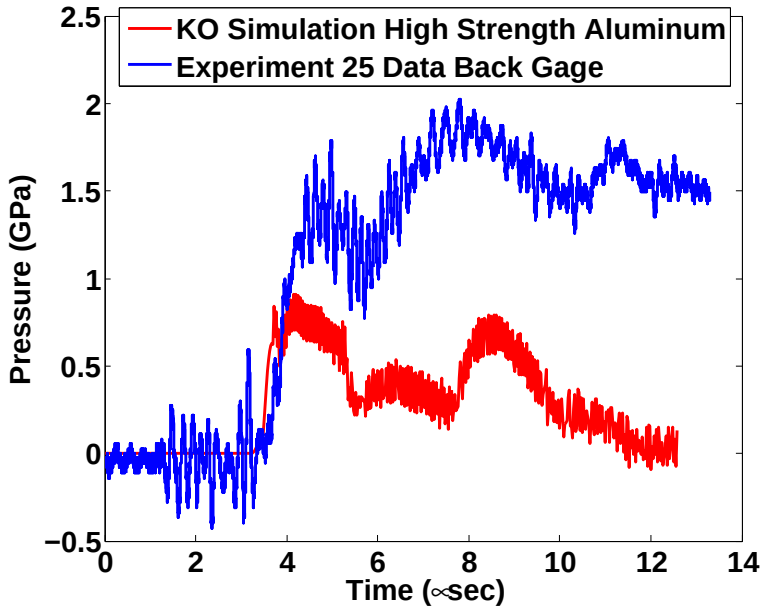

Figure E.8: Back Gage Simulation and Experiment Pressure Trace for Experiment 25 over 14 Microseconds. Shot Velocity 271 m/s and Powder Density 2.747 g/cc.

APPENDIX F

Stress Measurement Apparatus

The Construction of the Stress Gage Target can be followed through the process outlined in the Figures below:

The gage is fixed to the center of the aluminum back plate with 3MM CA8 Instant Adhesive, making sure the metallic side of the gage is facing up. The tab of the gage faces the side opposite the two exterior bolt holes. Wire leads are cut from 22 AWG insulated, braided copper wire. The two leads should measure 2-3 inches in length with 0.5 inches of stripped wire on each side. The copper braids should then be twisted together and soldered into a smooth single conductor. The wire leads are then soldered to the gage. There should be no wire exposed to the aluminum back-plate (i.e. the wire insulation should be in contact with the manganin gage). Also, make sure the lead wires are attached such that the powder cylinder can fit in its bolt hole pattern Hysol 0151 Epoxy is used to cover the wire and gage connection (Again, make sure the epoxy is located such that the powder cylinder can fit in its bolt hole pattern. A "quarter-size" section of epoxy is then placed on top of the gage, and covered with a mylar sheet. A popsicle stick is then used to evenly spread the epoxy and remove all air pockets between the mylar sheet and aluminum back plate. The results of these steps are depicted in Figure F.1

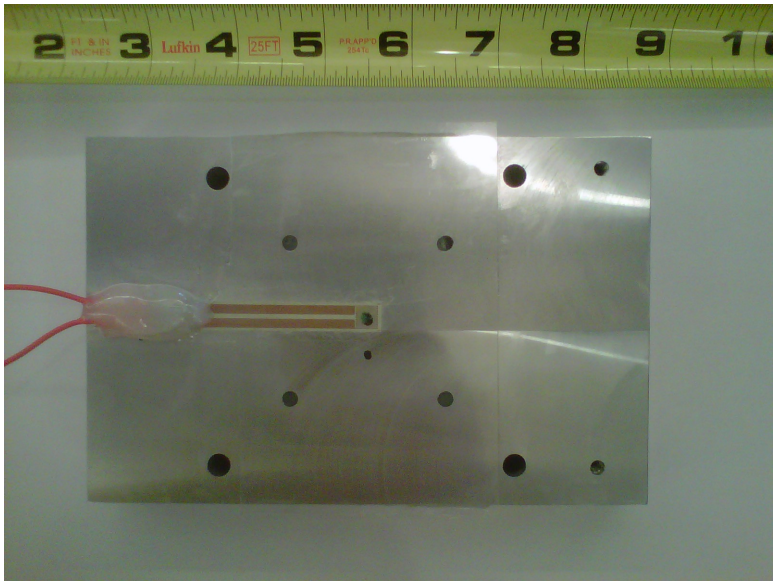

Figure F.1: Completion of Step 1 in Two Gage Target Construction

The copper buffer sheet is then fixed to the result of Figure F.1 and a chisel is used to indent the location of the bolt holes. A drill press is then used bring the holes to full diameter and to remove all epoxy.

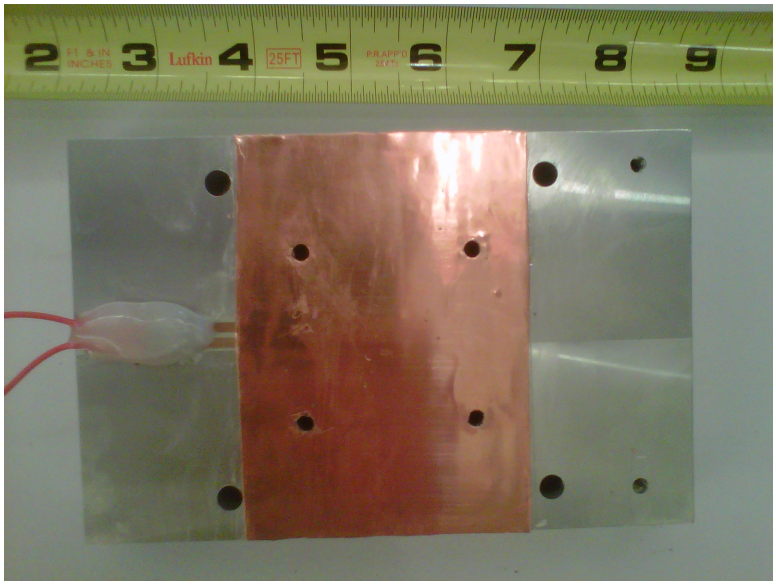

Figure F.2: Gage System with Copper Buffer and Bolt Holes

The next step is to press fit the cylinder and aluminum piston back plate flush to one end of the container. This operation was completed on a ENERPAC Hydraulic Press. The pieces are seen in Figure F.2 and fit in Figure F.3

Figure F.3: Powder Container and Aluminum Back Piston

Figure F.4: Powder Container and Aluminum Back Piston Press Fit

Powder is then poured into the powder container and all powder on the upper surface of the container is carefully removed.

The powder cylinder is then bolted to the aluminum back plate in the orientation depicted in Figure F.3 (Piston toward the floor). The piston is then pressed to the appropriate density on the MTS. A flange and piston of appropriate thickness have been developed to attach the target to the MTS. Use the MTS calibration sheet to determine the stroke length required to compress the target to

Figure F.5: Powder Container Filled with Powder

the appropriate density. The aluminum front gage leg-rest is then bolted to the aluminum back plate. The leg-rest is required to support the legs of the gage. Check the Resistance of the gage to insure the gage is intact.

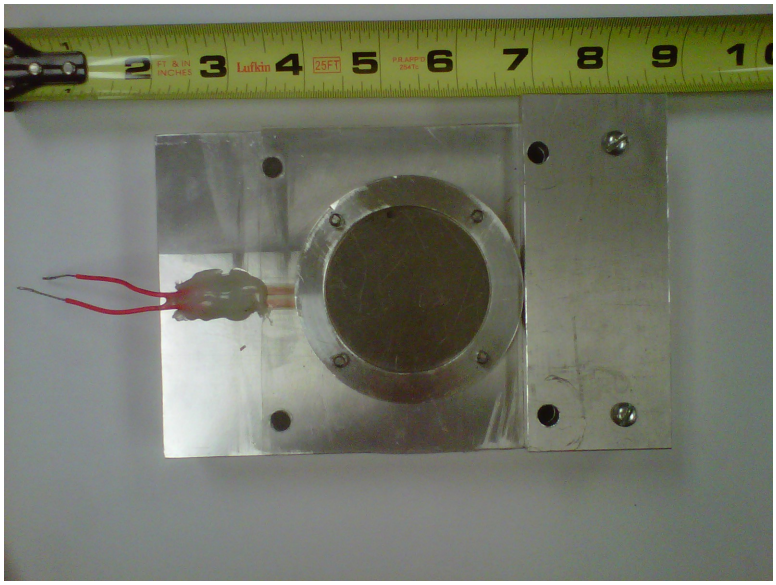

Figure F.6: Aluminum Back Piston Pressed to Appropriate Density and Aluminum Gage Leg-Rest

Note: An exacto knife can be used to remove the copper around the powder cylinder, however this is not recommended due to damage that can be incurred to the gage during removal. In Figure F.10, the copper shim remained unaltered

throughout the target assembly process to prevent any unintentional damage to the gage.

The target is then placed on a Browne & Sharpe Reflex 343 DMM to check the planarity of the pressed piston. Fifteen data points were chosen to cover the surface area of the piston with the deviation from the top of the cylinder recorded.

A milling machine was then used to channel the leg rest to the appropriate width and depth so the gage can rest properly on aluminum back plate and leg-rest. The milling machine may also be needed to expand the inner diameter of the cylinder containing the powder to allow the front aluminum plate to slip on. If the fit is not loose the front gage will break when the front aluminum plate is pushed on. The gage is then affixed to the aluminum back piston with Instant Adhesive.

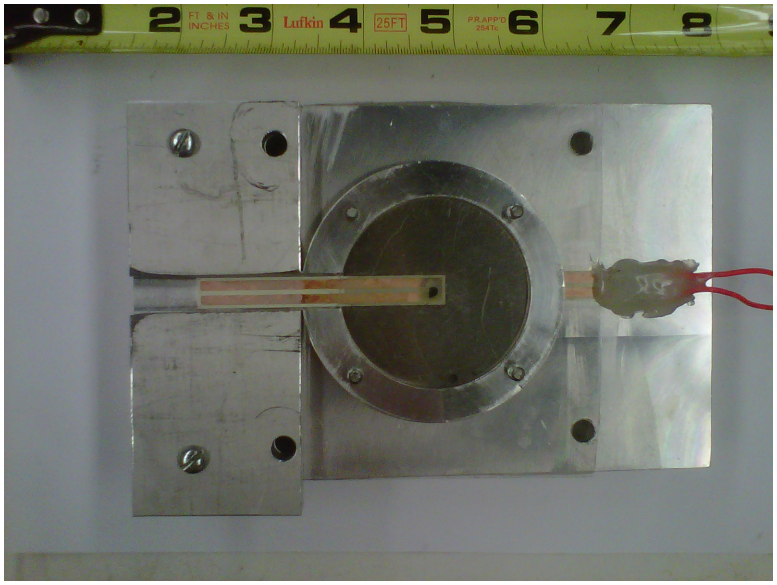

Figure F.7: Front Gage Applied to Target System

The front gage leads are soldered to the gage using the same method as discussed previously. Epoxy is once again applied used to cover the gage and wire lead connections. Make sure epoxy is covering the gage up to the surface of the front plate. This will ensure the gage will remain intact and survive the experiment. A section of epoxy (the size of a nickel (United States coin)) is then placed on top of the gage, and covered with a mylar sheet. The mylar sheet should be 2" in diameter with a 0.25"-0.5" tab to encapsulate the gage up to the lead wires connection. A popsicle stick is then used to evenly spread the epoxy and remove all air pockets between the mylar sheet and aluminum back plate. In addition, paper towel is required to clean the inner surface of the cylinder to insure no epoxy is on the cylinder edges or on the surface of the Mylar sheet that would obstruct the placement of the front plate.

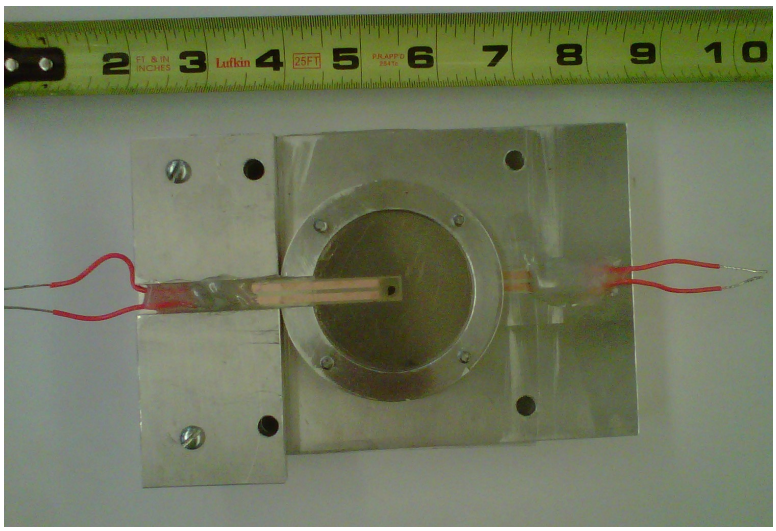

Figure F.8: Front Gage Applied with Leads Soldered and Mylar Encapsulating Sheet

The aluminum front plate with a mirror finish is then gently affixed to the gage assembly with Instant Adhesive. Check the Resistance of the gage to insure the gage is intact.

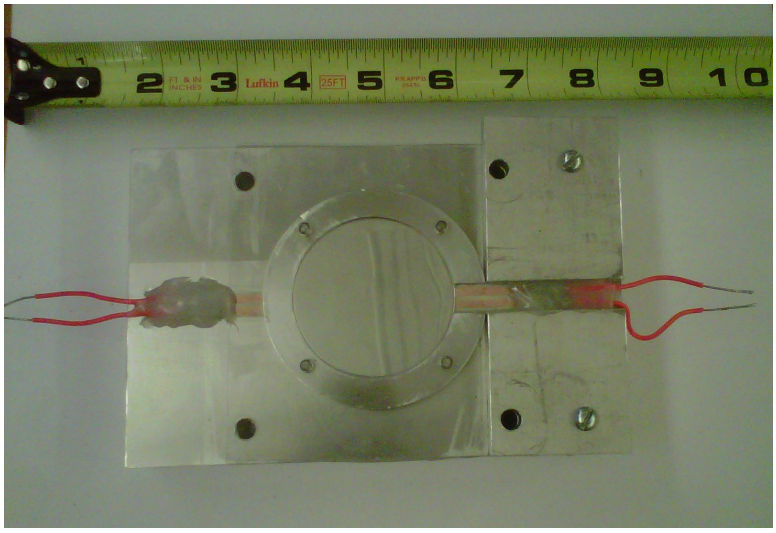

Figure F.9: Aluminum Front Plate Fixed to Gage Assembly

A #44 drill bit is then used to drill the through hole for the piezoelectric pin. The through hole will remove all epoxy and debris between the front plate and the back plate. Use a high drill speed to complete with task. Then 2" of heat shrink fit is cut to insulate the piezoelectric pin, allowing for roughly 0.025" to 0.050" exposure on the projectile interface side and 0.50" on the connection side. The pin is then fit through the hole and epoxied on the back side to keep the pin rigid and allow vacuum to hold. Instant Adhesive is also used as a void filler on the front plate for the piezoelectric pin to prevent vacuum from disturbing the powder and system.

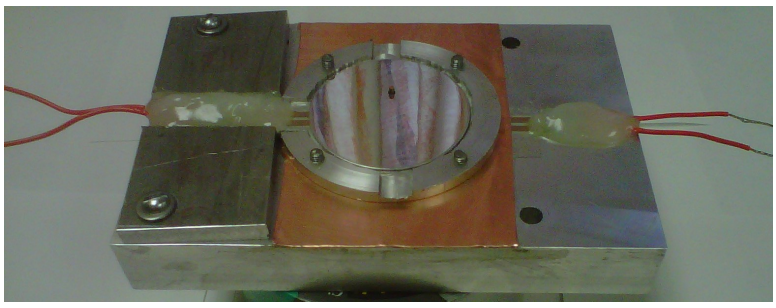

Figure F.10: Aluminum Front Plate Fixed to Gage Assembly

The target is brought back to the Browne & Sharpe Reflex 343 DMM where the distance of the piezoelectric pin above the front plate surface is more accurately

determined. For the current SSGG, the distance of the pin above the front plate surface is on average 0.090". However, with improvements in the vacuum system and gage manufacturing, this distance could be reduced to 0.010"-0.020" to increase the available resolution of the oscilloscope. The distance is recorded and will be used for oscilloscope triggering purposes.

APPENDIX G

Marquette University Single Stage Light Gas Gun

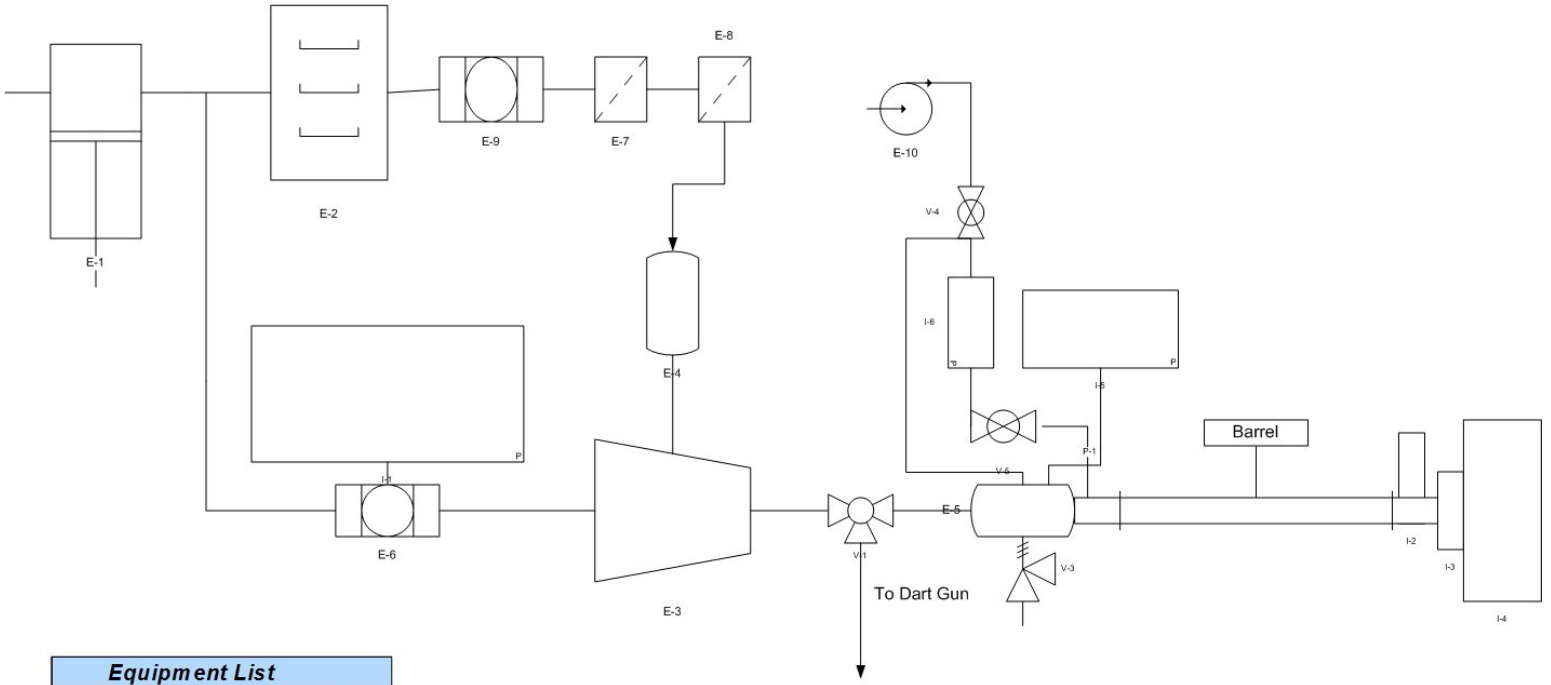

Equipment List	
Displayed Text	Description
E-1	Air Compressor
E-10	Vacuum Pump
E-2	Air Dryer
E-3	Gas Booster
E-4	Compressed Air Holding Tank
E-5	Breech
E-6	Filter-Pressure Regulator
E-7	Filter 3
E-8	Filter 2
E-9	Filter 1

Valve List	
Displayed Text	Description
V-1	3-Way Ball Valve Gas Booster - 1" Gun-Dart Gun
V-3	Breech Pressure Relief Valve
V-4	Vacuum Pump Line Ball Valve
V-5	Barrel Vacuum Line Ball Valve

Instrument List	
Displayed Text	Description
I-1	Regulator Pressure Gauge
I-2	Velocity Pin System
I-3	Stress Gage System
I-4	Alumnium Anvil
I-5	Breech Pressure Gauge
I-6	Vacuum Gauge

Figure G.1: Marquette University Single Stage Light Gas Gun System Component Diagram

APPENDIX H

Compacted Powder Images

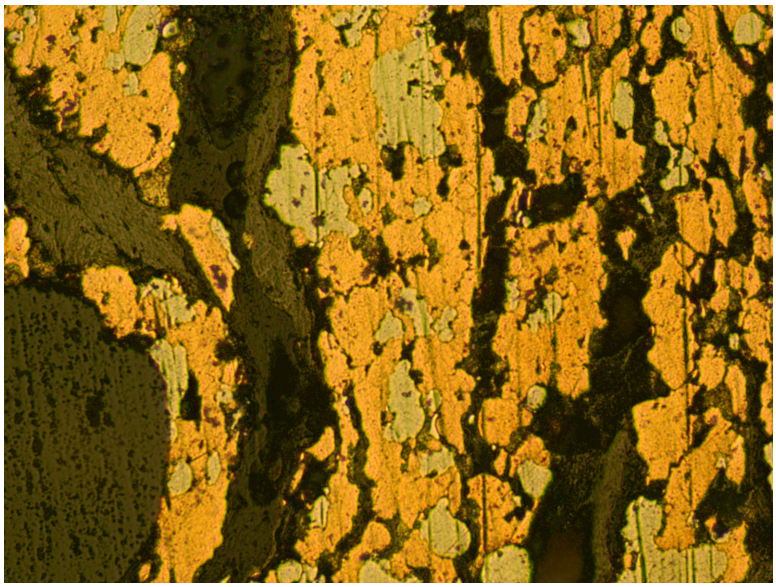

Figure H.1: Dynamically Compacted Powder at 0.203 GPa with 100X Magnification for Use in Porosity Determination)

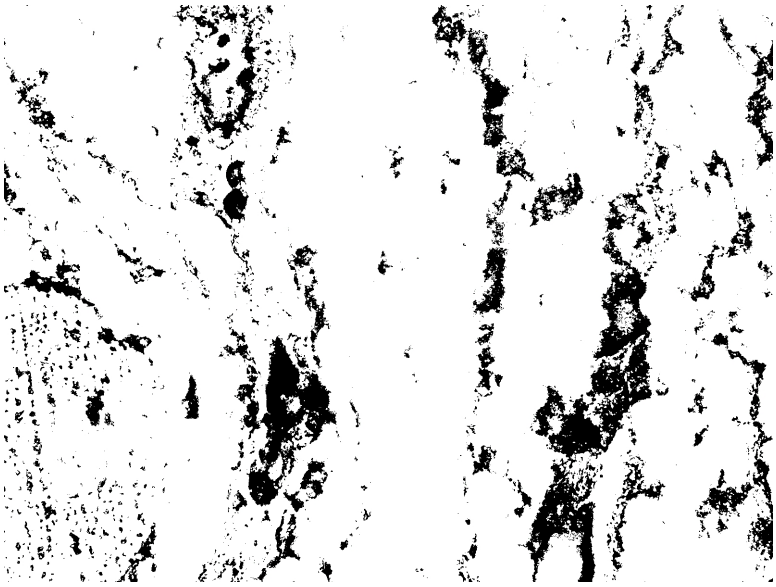

Figure H.2: Porosity of Image in Figure H.1

Figure H.3: Cross Section of Dynamically Compacted Powder at 0.34-0.433GPa.

Figure H.4: Dynamically Compacted Powder at 0.34-0.433GPa Upon Removal from Gas Gun Target (Removed Cross Section for Imaging)

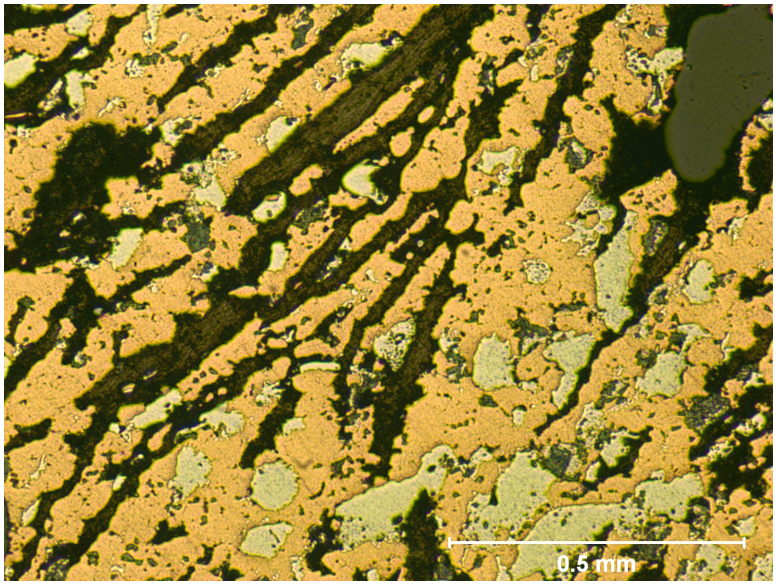

Figure H.5: Optical Image of Statically Pressed and Sintered Powder Compact Magnification 50X. (Pressed from the Left to Right)

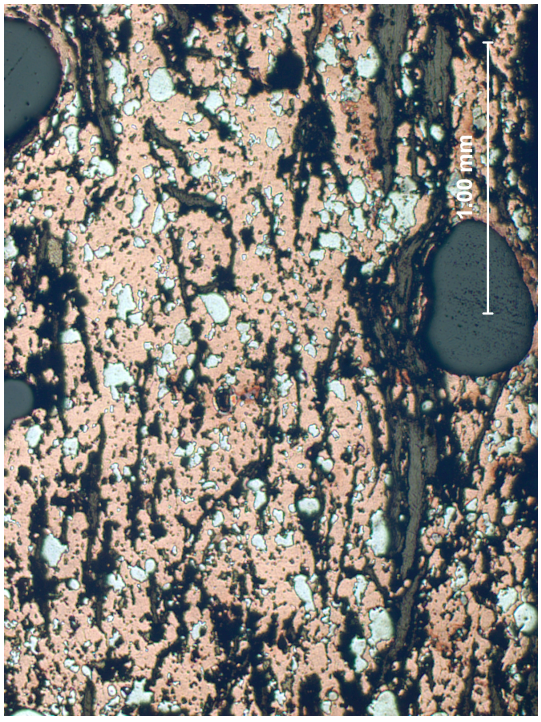

Figure H.6: Optical Image of Statically Pressed and Sintered Powder Compact at Lower Magnification. (Pressed from the Left to Right)

APPENDIX I

Experimental Apparatus Material List

The list below is an accumulation of the necessary components to build and operate each experimental apparatus. The main components for the Marquette University Single Stage Light Gas Gun including air delivery system and breech can be found in the thesis of Tom Downs [26]. A section will be devoted to additions to the Single Stage Light Gas Gun from the research of Downs.

Velocity Measurement System

Component	Manufacturer
System Block: 5"x0.75"x1" 1018 CR Bar	Online Metals
Qty: 2 Acrylic Mounting Plate: 1"x1"x4"	Midland Plastics
Nylon Channel Tee: 1"x0.5"x2.75"	Midland Plastics
Qty:(4) 3/32"x1" Allen Bolts	Menards
Graphite Guides: 3/16" Nylon Rod	Online Metals
Qty: 2 Copper Buses: 1/4" x1/2" x 2.75"	Speedy Metals
0.5mm Graphite (Pencil Lead)	Office Depot
Vacuum Sleeve: 3.25" OD 2.85" ID 4" L Steel	Metals Express
Variable Voltage Supply: 6216A	Hewlett Packard
Vacuum Sleeve O-Rings: Dash Number 150	McMaster Carr
Acrylic Lid 3/8"	Midland Plastics
24 AWG Insulated Copper Wire (Copper Buss to Lid)	Radio Shack
Lid Fasteners	Menards
Qty: 4 8-32 x 2" Bolts	
Qty: 4 8-32 Washers	
Qty: 24 8-32 Nuts	
Qty: 4 Alligator Clips	Radio Shack
1/8" Red Rubber Gasket	McMaster Carr
Qty: 4 Banana Plug Assemblies (Pomona) 4ft	Newark
Oscilloscope: 2 Channel 54600A	Hewlett Packard

Stress Gage Targets

Component	Manufacturer
Base: Aluminum 6061 4”x6”x1”	Speedy Metals
Cylinder: Aluminum 6061 2.75” D	Speedy Metals
Front Plates: 12” SQ Al 6061 0.32” Sheet Metal	McMaster Carr
Vacuum Plate: 12” SQ Al 6061 0.32” Sheet Metal Mirror Finish	McMaster Carr
Stress Gages: 50 ohm Manganin Gages LM-SS-210FD-050	Vishay- MM
Qty:4 10-32 Countersunk Bolts	Menards
0.004” Copper Shim CU-4 6” x100”	Lyon Industries
Mylar Transparency Paper	Apollo
Hysol 0151 Epoxy Resin- Hardener	Loctite
Piezoelectric Pins: CA-1135+2”	Dynasen Inc.
22 AWG Copper Stranded Wire	Radio Shack
Heat Shrink Fit Tubing 0.061” ID	McMaster Carr
3A8 Instant Adhesive Scotch Weld	3MM
Anvil: Aluminum 6061 3.25” x4” x7”	Speedy Metals
Nylon Insulator: 1” Round	Midland Plastics

Stress Data Acquisition System

Component	Manufacturer
4 Channel Oscilloscope: DSO6054A	Agilent Technologies
Piezoresistive Pulse Power Supply: CK2-50/0.050-300	Dynasen Inc.
Qty: 2 75 ohm BNC Terminator	Newark
Qty: 2 3283 F-F BNC Adapters	Pomona
Qty: 2 B-24 Banana Plug Assembly	Pomona
Qty: 2 50 ohm BNC Assembly 2249-C-96	Pomona
Qty: 2 75 ohm BNC Assembly 2249-E-24	Pomona
Qty: 2 50 ohm BNC Assembly 2249-C-36	Pomona
Qty:2 BNC to F-Banana Plug Adapters 1270	Pomona
Piezoelectric Pin BNC Assembly CA-1148-1	Dynasen Inc.
Decade Resistor Box: HARS-X04-0.01	IET Labs
Uninterruptible Power Supply- Smart 1000LCD	TripLite

Projectiles

Component	Manufacturer
Sabot: 1” Nylon Round Stock	Midland Plastics
Flyer Plate: 1” Aluminum Round Stock	Metals Express
Sabot O-Rings Qty:2 Dash Number 117	McMaster Carr

Vacuum System

Component	Manufacturer
160VP CuteVac Direct Drive Rotary Oil Vacuum Pump	Hitachi
5ft 1” ID Plastic Tubing	Grainger
1” Hose Barb to 1” Male NPT	Menards
1” Coupling Nut	Menards
1” Male NPT to 1/2” Female NPT Reducer	Menards
1/2” Nipple	Menards
1/2” Galvanized Female NPT Tee	Menards
1/2” Ball Valve NPT R850 150WSP/600WOG	Mueller Industries
Qty: 4 1” Hose Clamps	Menards
1/2” Male NPT to 1/4” Male NPT Galvanized Reducer	Menards
1/4” Female NPT Galvanized Tee	Menards
1/4” Galvanized Nipple	Menards
1/4” Ball Valve Female NPT 5044F 150WSP/600WOG	Red/White Valve
1/2” Male NPT to 1/4” Female NPT Reducer	Menards
Qty: 4 1/2” Hose Clamps	Menards
Qty: 2 1/4” Male NPT to 1/4” Hose Barb	Menards
16ft 1/4” ID Plastic Tubing	Menards
Qty 2: 1/4” Female NPT Air-Line Quick Connect	Menards
0-30 in Hg Pressure Gauge	Wika
Breech Side Vacuum Fittings	Menards
1/4” Male NPT to 1/4” Hose Barb	
Qty: 2 1/4” Male NPT to 1/4” Hose Barb	
Qty: 21/4” Female NPT to 1/8” Female NPT Reducer	
Qty: 2 1/8” Nipple	

Alterations to Gas Gun Developed by Downs

Component	Manufacturer
Barrel: 1” ID 2” OD 36” Length DOM Steel	Aladdin Steel
1/2” Three Way Valve- Booster to 1” Gun, 1/2” Gun, Part: SS-83XS8	Swagelok